DESIGN, SIMULATION OF FLUID FLOW AND OPTIMIZATION OF OPERATIONAL PARAMETERS IN TESLA MULTIPLE-DISK TURBINE

A Thesis Submitted to the School of Graduate Studies at Addis Ababa University Institute of Technology
In Partial Fulfillment of the Requirement for Degree of Masters of Science in Mechanical Engineering
(With Specialization in Thermal Engineering)

Advisor: Dr.-Ing. Abebayehu Assefa

By: SURAFEL SHIMELES
April 2014

Submitted by:

Surafel Shimeles	________________	________________
Student	Signature	Date

Approved by:

1.	________________	________________	________________
	Dr.-Ing Abebayehu Assefa (Project Advisor)	Signature	Date
2.	________________	________________	________________
	Dr.-Ing Edessa Dribsa (Internal Examiner)	Signature	Date
3.	________________	________________	________________
	Dr. Tesfaye Dama (External Examiner)	Signature	Date

Acknowledgement

God, however long it may have been, you have come along finally when I still believed less of myself.

I would like to thank Dr.-Ing. Abebayehu Assefa, for going through all the material and providing constructive inputs, directions and corrections, whenever so needed. I am greatly indebted to my mother, W/o Meaza Endale, for providing me the morale and material support to make this thesis a true success. Of course, this paper would not have been a complete one without any peer support from my good friends, Binyam Kebede, Yidnekachew Messele and Messay Mekonen.

Abstract

Tesla turbine, an unconventional co-axial multiple-disk turbine utilizing a blend of friction and boundary layer effect for power production, has been a topic of many academic and experimental works for a century. Decades after its first patent in 1913 by Serbian genius -Nikola Tesla, the turbine has seen subject of many fluid investigators that sought to explain mainly the fluid dynamics behind the flow between its narrow inter-disk spaces for purpose of maximizing utility for practical applications. Among the available literature, there is a plethora of research in analytical and experimental spheres while on the other hand, there are limited published works regarding numerical investigation of the turbine. Between the different numerical genera, negligibly no numerical work has been performed in studying the turbulent regime of flow.

In the current work, a background discussion introducing the Tesla turbine theory, merits, demerits and previously done works is presented. A modified two-dimensional Cuoto etal. turbine design procedure is used to construct 2D and 3D geometrical models for CFD analysis. Two principal models have been prepared, each of which having their inherent strengths and weaknesses. The effect of certain operational parameters such as rotor angular speed and flow on selected performance figure of merits has been quantitatively analyzed. By keeping flow input variables, the number of nozzles has been varied as an added geometrical design parameter to see performance disparity between different combinations.

The results revealed peculiar flow characteristics belonging to the disk gaps and the strong variances of the selected figures of merits with controlling parameters. In some cases, operational limitation thresholds were established due to the strong correlations of these performance variables with turbine output quantities.

1 Table of Contents

Table of Figures

List of Tables

Symbol	Unit	Description
Q	m^3/s	Fluid discharge
ω	rad/s	Angular velocity
r	m	Radial position
b	m	Inter-disk spacing distance
u	m/s	Tangential velocity
Δ	-	Change
P	m	Perimeter
p	$kg/m\text{-}s^2$	Pressure
ρ	kg/m^3	Density
L	m	Length, duct length
d	m	Diameter
D	m	Duct diameter
f	-	Fanning friction
k	-	Pressure loss coefficient
α	-	Visco-geometric number
v	m/s	Radial velocity
υ	m^2/s	Kinematic viscosity
RR	-	Radius ratio
AR	-	Aspect ratio
μ	kg/m-s	Dynamic viscosity
A	m^2	Area
x	m	Length on which full boundary thickness develops
T	K	Temperature
T	N-m	Torque
C	-	Coefficient
n	-	Number of disk spacing
s	m	Disk row end spacing distance

Superscript/ Suffix	Description
o	Outer, ambient
i	Inner
-	Non-dimensional
f	Friction
a	Associated to the gap
u	Enlargement(up)
d	Contraction(down)
b	Bend, gap
inlet	Inlet
static	Static
air	Air
av	Average
lam	Laminar
eff	Effective
h	Hydraulic
flow	Flow
wet	Wetted
turbulent	Turbulent
gap	Gap
disk	Disks
M	Moment
total	Total
out	Outlet
k	At local point k
nb	Neighboring

"There is something within me that might be illusion as it is often case with young delighted people, but if I would be fortunate to achieve some of my ideals it would be on the behalf of the whole of humanity."

Nikola Tesla

Chapter 1

1. Introduction

1.1 Background

The Tesla turbine is a bladeless centripetal flow turbine patented by Nikola Tesla in 1913. It is referred to as a bladeless turbine because it uses the boundary layer effect, not fluid impinging upon its blades, as in conventional turbines. The Tesla turbine is also known as the ‘boundary layer’ turbine, ‘cohesion-type’ turbine, and ‘Prandtl layer’ turbine (after Ludwig Prandtl). All the above designations mainly refer to the construction feature or principle with which the turbine operates.

The Tesla turbine has captured the attention of many during the last century in that the simple stack disk construction can be practically made in small workshops where the manufacturing capabilities are minimal. The amount of power generation can be modularly enhanced by increasing the number of disks on the drive shaft which is in turn coupled to a generator. As a consequence, this characteristic results in compact power generation. To add, the turbine can be operated with steam exhaust from steam turbine or from any steam source (solar thermal system, geothermal power plant or from a flash chamber), making it suitable for low temperature waste energy recovery, which otherwise would have been wasted because of its poor energy quality. It also can be used for pumping viscous and abrasive fluids by making only slight modification to its circular casing.

Besides the geometrical simplicity, the study of its viscous flow between any two of the rotating parallel disks in a fixed enclosure has received considerable interest over the past six decades since the phenomenon is of significant scientific interest and much of practical importance. Researches on this topic have been made and the results are diverse. Many analytical and experimental efforts have been made on this field but at the present not many comprehensive works using CFD tools have been published.

This work does not pretend to answer all the questions that have been formulated for the Tesla turbine, but an approximation of the “analytically unsolved Navier-Stokes equations” using FLUENT software. It is thus the subject of this work, in which CFD tool is used in order to solve the mathematical equations that govern the fluid motion.

1.2 Objective and Scope

Major objective of this study is to find-out and describe general field parameters which are of practical concern for characterization of this unconventional turbine.

The specific objectives of the project are:

- Design a Tesla turbine for specific input condition;
- Numerical modeling and solution of a fluid flow between any two rotating disks of the turbine with available fluid mechanics equations;
- Pointing out possible design parameters which can optimize efficiency of the turbine.

1.3 Methodology

The methods to be employed to achieve the objectives of the research are:

1. Literature review;
2. Numerical modeling;
3. Simulation of flow using FLUENT software; and
4. Analysis and interpretation of the results.

1.4 Outline

The study will review the different works performed by various authors on issues related to fluid flow in the inter-disk space and attempts to approximate this flow with certain assumptions with already known conservation equations. Up on the evaluation of the previous works undertaken by different investigators, a design activity will be carried out for already set design conditions applying boundary layer and fluid mechanics equations. Right after determination of the major physical dimensions, two geometrical models will be constructed in Gambit® later to be solved in FLUENT software by imposing prevalent flow boundary conditions. The results of the simulations will be discussed in detail and the paper winds by giving necessary recommendations and works for future study.

Chapter 2

2 Literature Review

2.1 Nikola Tesla and the Birth of Tesla Turbine

Among the scholars and scientist of the twentieth century, one man stands out as one of the most prolific and pragmatic of all figures, Nikola Tesla. Nikola Tesla is, by far the most practical of all inventors of his time in that his inventions shaped the way we live and communicate with each other. Tesla is the unsung creator of the electric age, without whom the radio, television, auto ignition system, telephone, alternating current power generation& transmission would all have been impossible. He discovered the rotating magnetic field, the basis of most alternating-current machinery and held more than 700 patents. His inventions make him one of the foremost pioneers in the distribution of electric energy [1].

He was born in 1856 from Serb family in Croatia where he began his study and research in electricity. He trained to be an engineer, attending the Technical University at Graz, Austria and the University of Prague. Beginning his studies in physics and mathematics at Graz Polytechnic, he then took philosophy at the University of Prague. It was during this time that he had one of his most famous ideas, the rotating magnetic field and alternating current induction motor. Tesla began work as an electrical engineer with the Central Telegraph Office in Budapest, Hungary in 1881 and the following year, he went to work in Paris for the Continental Edison Company. In 1883, he constructed, after work hours, his first induction motor. Then after sailing to America in 1884, Tesla found employment in the Edison Electric Company where he served close to two years before living to pursue his own inventions in the alternating current area which in principle were new and completely different from Edison's direct current concept. The alternating current offered superior advantage for power transmission in that electric current could be transmitted over long distances with minimum current in the conducting lines leading to reduced electrical loss. By 1885, he already sold his patents of his induction motor, his poly phase system of alternating-current dynamos, transformers and motor to the West Wing House Power Company which still functions with the same basic principles of Tesla to modern day. In April 1887, he established his own laboratory, where he experimented with shadowgraphs similar to those involved in the discovery of x-rays. In 1888, his discovery that a magnetic field could be made to rotate if two coils at right angles are supplied with AC current 90^{O} out of phase made possible the invention of the AC induction motor. The major advantage of this motor is its brushless operation which many, at the time, believed impossible. In 1891, the Tesla coil was invented. This device was used primarily in televisions and radios. This was also the same year that Tesla was given citizenship in America. During the following years, Tesla received royalty payments for his alternating current motor and power transmission method patents. By May of 1905, the patents had expired and the royalties came to end.

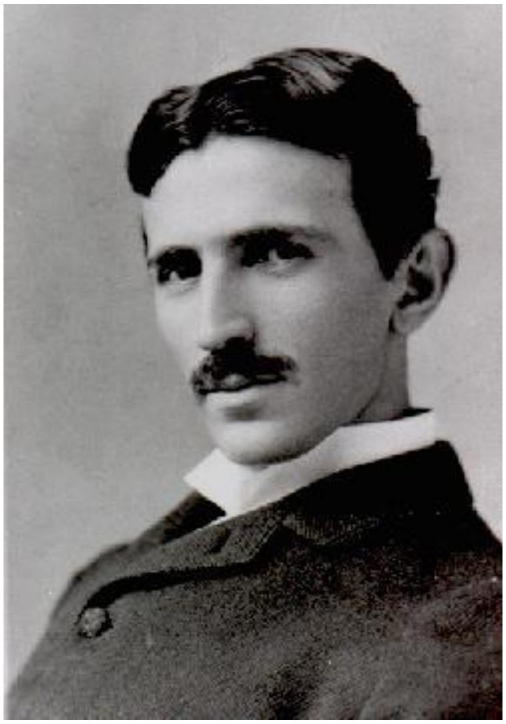

Figure 2-1: Nikola Tesla

In 1906, Tesla returned to his work and began focusing efforts on an improved turbine design. It took several years of research and experimentation, but the Tesla turbine was finally realized. Turning away from the common propeller design that turbines of the time used, Tesla implemented discs attached to a shaft that could be spun using steam or gas. The concept was considered radically different.

Even though Tesla's turbine patent was registered in 1913, the actual concept originates over four decades earlier. A patent for a European bladeless turbine was registered in 1832. The idea was not as effective as Tesla's future turbine would be. It served as a foundation for Tesla to work off. After making several improvements, Tesla worked on increasing the potential of the bladeless turbine [2]. A patent was issued to Tesla for both the concept and the device [3], hence the name Tesla Turbine. The turbine configuration is also referred to as the shear-torque turbine and the bladeless turbine [4].He demonstrated the concept with a steam powered, eight inch diameter turbine that developed over 200 horsepower [1].

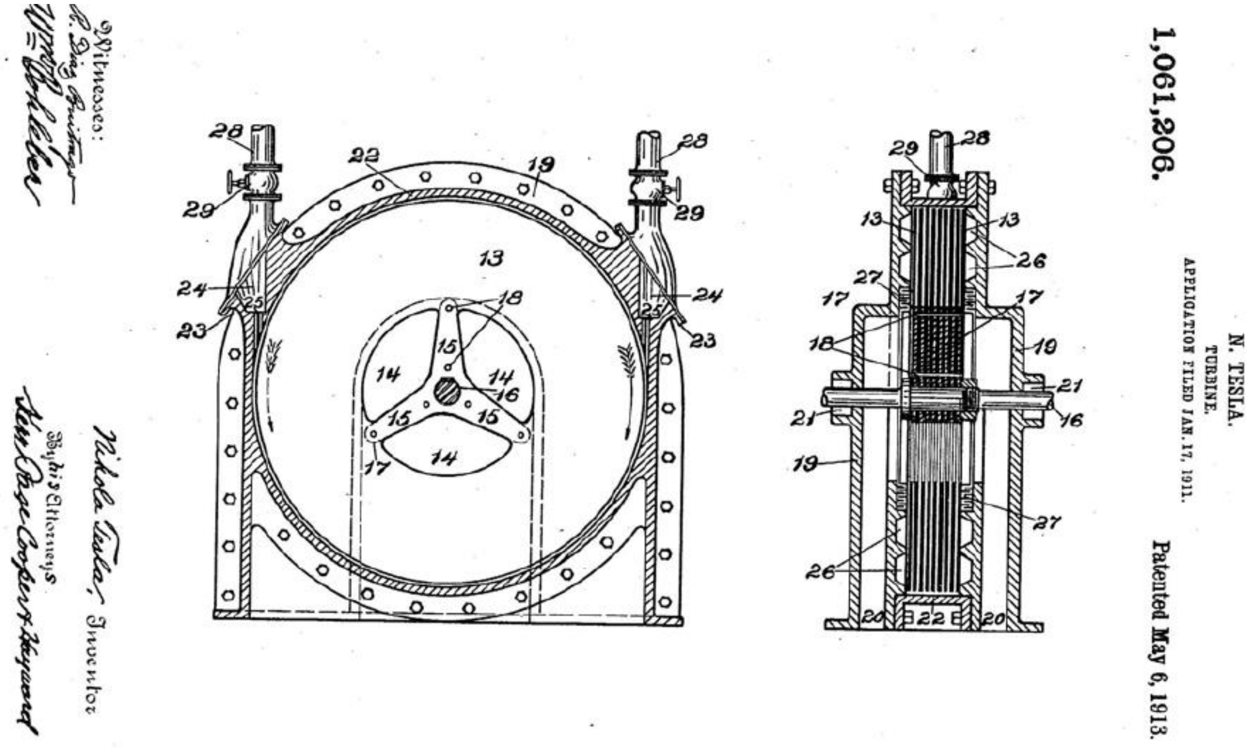

Figure 2-2: Original Patent of the Tesla Turbine as Patented in 1913 by the U.S. Patent Office [31]

The design makes use of the effects which occur in the boundary layer flow between the rotating disks placed very close to one another. The fluid flowing spirally from the outer to inner part transfers energy to the rotating disks. The supply usually takes place from several nozzles discretely located along the circumference. The medium flows out through the holes in the disks situated near the turbine shaft.

From what Tesla wrote in the patent, it seems his experiments were mainly done with liquid fluids but had confirmed it works with air as well. Normally compressed air, fluids or steam is applied to the inlet and the turbine spins giving a mechanical rotational output.

What Tesla claims in his patents was a high efficiency close to 95% due to the form of energy transfer, based on the assumption that a highest economy will be attained when the changes in velocity and direction of the movement of the fluid is as gradual as possible. Ideally, this can only be accomplished by causing the propelling fluid to move in natural paths or streamlines of least resistance, free from constraints and disturbances caused by vanes or intricate devices in common turbo machinery, and changing the fluid velocity and direction of movement by imperceptible degrees.[6] If so gradual deflection of the fluid element by small degrees is needed, the physics of the problem might indirectly translate to larger size disks which are not economically sound. It was later found that, with experimental replication of Tesla's test conditions run by W. Rice, the actual efficiency hovers between 36 % and 41 %. [60]

When he designed the Tesla multiple disk turbine, contemporary turbines of its day were inefficient because of the poor aerodynamic understanding and lack of suitable blade construction materials. However, early steels could not withstand high temperatures, thus limiting turbine power. Tesla sidestepped this problem by using shear drag forces and devising a system that was very efficient at relatively low speeds. However, steels of the day were not sufficiently resilient to withstand large shear forces when designed at the thickness required by the Tesla turbine design. This led to unavoidable warping when the turbines were operated, and is the same reason why the turbines never gained widespread industrial application [5]. Because of this reason, Tesla himself did not procure a large contract for production. With modern day metallurgy, it has been possible to overcome this problem to fabricate a warp free rotor disks.
Starting from the patent of Nikola Tesla, extensive analytical works were made in the 60's and 70's [6].

2.2 Conventional Turbo machinery versus Tesla Turbine

Frictional shear force in conventional turbo machinery has detrimental effect into the operation of the machine and this situation becomes more severe as the diameter of the blades and the spacing between them decreases. As a result, the specific power and the efficiency of turbine plunge to lower values. The primary advantage of conventional turbines is a high power output-to-weight ratio and high efficiencies for larger units. Friction force on the contrary, helps the transfer of momentum from the swirling fluid to the co-rotating disks by retarding the flow in Tesla turbines. Investigation by Rice [8] asserts that attainment of higher efficiency could only be made possible within the low flow regions of operation. Consequently, due to the smaller flow rate range of operation, the Tesla turbo machinery is only economically suitable for low torque and power requirements where conventional turbines are inadequate. In contrast to conventional turbo machines, the reduction in disk spacing helps in the boundary layer formation which is a plus to the transfer of energy between the fluid and the rotating wall.

2.3 Geometry

The rotor of Tesla turbine consists of rigid circular flat disks rigidly mounted in parallel fashion on a rotating shaft. In theory, the thickness of the disks should be as thin as possible. The passage for provision of fluid movement is provided by means of thin spacers that are placed in between each disk. The spacers could be of annular shape, in which case they will be fixed on the shaft, or in some other case, they could be made of thin cylindrical shaped magnets that may be placed in circular pattern around the entry radius where they cause little intrusion to the ingoing flow. It is important to note that there could be negligible relative movement between the disk and the spacers once motion of the whole pack commences.

According to Rice [9], the highest value of efficiency appears when they are approximately equal to twice the boundary layer thickness. The gaps between the disks should depend on the prevailing flow conditions and physical properties of the working fluid. On the other hand, the thickness of the disks and the distances between them are also limited by the material strength, the technology of manufacture and assembly.

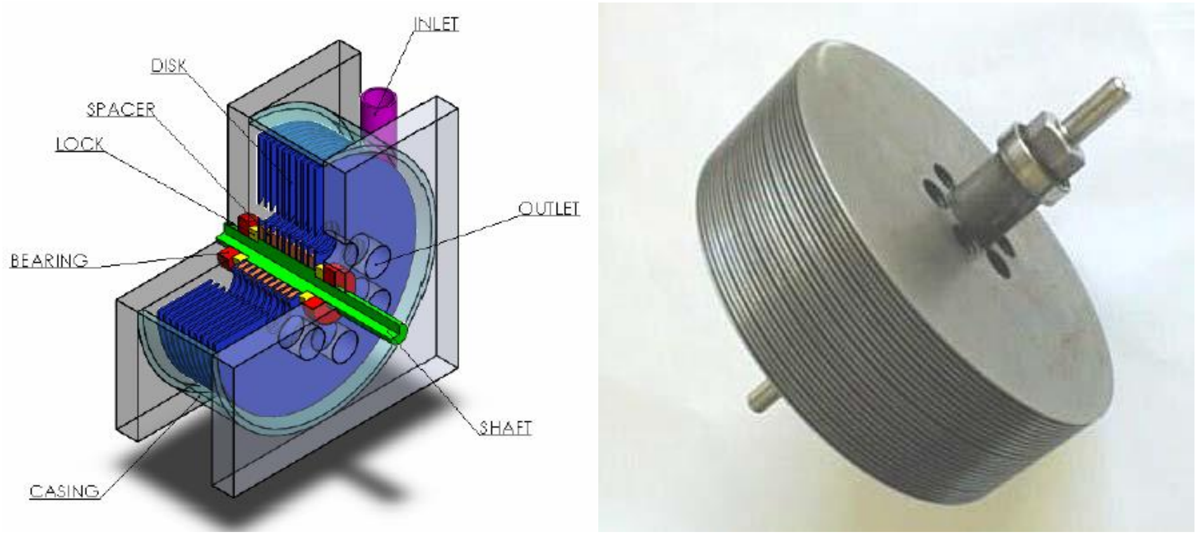

Figure 2-3: a) A cut-away view of a Tesla turbine Assembly Consisting Basic Parts b) An Actual Disk Turbine Assembly without Shroud Covering [6]

Figure 2-3: (b) shows a disk bank and spacer assembly which is held in place by a locking nut which is fastened to a thread at one end of the shaft and by a sleeve which is integrated to the shaft on the other end. At both ends, the shaft is inserted to radial bearing in bearing seat for smoother operation. The bearing seat is part of the external casing through which the exit of the nozzle is used to introduce fluid into the blade row.

The supply takes place from the nozzles discretely located along the circumference. The nozzles are tilted under a certain angle to the tangent of the disk. If two nozzles are placed one opposed to the other, the rotational direction is imposed by the selection of the specific nozzle on which the direction of rotation is desired. Performance of the turbine is strongly dependent on efficiency of nozzles and the nozzle-rotor interaction [8].

2.4 Motive Principle

The working fluid enters the chamber through the inlet in the tangential direction and flows along the surface of the disk through the disk spacings. Due to viscosity, momentum exchange takes place between fluid and discs, as the fluid slows down and adds energy to the discs, it spirals to the center due to pressure and velocity, where exhaust is. Since the rotor has no projections, it is very sturdy. Flat discs with exhaust ports near their centers stacked up on a shaft with thin spacers between. These discs are spun by directing some fluid (air, water and exhaust gas) between them so that adhesion of the boundary layer of the fluid on the surface of the discs drags them around as the fluid travels in from the outer edge of the discs and out through the central vent holes. As disks start to rotate and their speed increases, the working fluid now travels in longer spiral paths because of larger centrifugal force. Through this phenomenon, some of the fluid energy is converted to mechanical work, causing the disks and shaft to rotate.

By considering the flow domain as a control volume and taking a steady state flow assumption with no force on the control surfaces, the momentum equation of fluid motion can be reduced to determine the power being produced by the turbine shaft.

$$\boldsymbol{P_{out} = \dot{m}.\omega.(r_o U_o - r_i U_i)} \tag{2-1}$$

As can be seen from the above relation, the main driving force behind power production is the difference in momentum of the tangential velocity vectors between the disk bunk entry (outer periphery) and exit (inner disk bunk departure point). Detailed derivation of this relation can be found in work performed by Ladino. [6]

2.5 Application

The applicability of this device is usually in the smaller power ranges of turbine and compressor applications. Most of the practical applications are in compression of fluids and slurries that contain significantly abrasive, viscous, solids, shear sensitive or otherwise difficult to handle with vane or centrifugal pumps.

Miller et al. [11] showed that Tesla pump could be effectively used as an artificial ventricle in the human heart. As Tesla pump has no valve, it can be operated in a pulsating mode just by controlling the voltage to a DC drive motor. Valente [12] claimed that Tesla turbine can be used successfully in gas liquefaction plants for pressure reduction of hydrocarbon gases. By incorporating Tesla turbine into liquefaction sequence, nearly isothermal liquefaction of hydrocarbon gases can be achieved.

In recent years, possibility for harnessing power from wind using Tesla turbine has been realized. The design includes an airfoil shaped spacer near the perimeter of the disk to induce lift and add further torque to the rotating shaft [13].

The general application areas in which Tesla turbo machinery is greatly suited have been summarized below.

- Biomass fuelled power plants
- Heat recovery installations
- Co-generation systems
- Systems using solar energy
- Installations where exhaust heat can be utilized
- Plants with low temperature geothermal medium

Some other applications that use the Tesla turbine principles are dentist drills, air compressors, air motor engines, vacuum exhauster and small propulsive devices for expandable weapons, such as torpedoes [4].

2.6 Advantages

Tesla turbine offers variety of operational and technical advantages. To mention some;

- Extreme simplicity, cheapness and reliability
- Greater stability due to the even distribution of rotor mass on the axis of rotation.

- Low mechanical stress in the turbine due to its small size and low peripheral speeds
- No axial load only tangential and radial fluid forces acting on the moving part of the turbine
- The internal static pressure inside the housing is very low, for this reason heavy cast housings are not necessary in order to assure its structural rigidity [6]
- Since there is no direct flow impingement on disk surfaces and negligible static pressure difference between sides of the disks is present within the disk-casing assembly, the rotors are less (disks) likely to suffer from cavitation.
- Ability to handle exotic fluids, e.g., highly viscous fluids, gas–liquid mixtures, highly concentrated commercial slurries and suspensions, combustion byproducts, and non-Newtonian fluids.
- Fluent transfer of the medium through the turbine without any slack actions [14]
- Relatively high turbine efficiency (in theory)
- Long lifetime
- The rotor is better adapted for dynamic balancing and through rubbing friction resists disturbing influences thereby ensuring quieter running [15]
- It does suffer from problems such as shear losses and flow restrictions [15]
- Valve failures that are common to conventional turbo machinery are not inherent to Tesla devices.
- No flow separation because the fluid is accelerated in the flow between co-rotating disks then unstable flow is not present with undesirable vibrations[6]
- Clockwise and counterclockwise direction of operation can be achieved by installing separate nozzle mechanisms on opposite sides of the casing.
- As opposed to explosion mode of failure which compromises human and equipment reliability during equipment over speeding in conventional turbo machineries, Tesla turbine components rather implode within the casing assembly and blown out through the central exhaust recess. The makes Tesla turbines safe to operate in extreme situations.
- Good load switching capability

This turbine can also be successfully applied to condensing plants operating with high vacuum. In such a case, owing to the very great expansion ratio, the exhaust mixture will be at a relatively low temperature and suitable for admission to the condenser.

2.7 Disadvantages

In 2003, in his review of past researches, Prof. Rice concluded the turbine will be best suited for applications that require high angular speed, low torque and low fluid mass flow rate. If the need for higher power arises, the rotor disks must be enlarged to accommodate the increased working fluid flow. This would, in turn, translates to higher tangential inlet velocities as a result of radial increment of the disks. Consequently, losses creep in as a result of energy being dissipated on the outer edge and profile faces of the rotor. The cumulative effect of this would be the introduction of low component of absolute velocity generating moment of momentum to the detriment of the operation.

The best design and operating point for the turbine is strongly dependent upon the inlet pressure and viscosity of the motive fluid. In addition, there is no unitary method of design as compared to classical bladed turbines which will be able to govern the sizing process. Most Tesla type turbines and pumps have been designed using intuition and simple calculations or empirical experience and ‘rules of thumb’. This has almost always led to the use of large spaces between the disks corresponding to turbulent flow between the disks [9]. The already existing design methodologies and tips presented in several patents, books, and journals, at times, are conflicting [16], consequently, creating a reduced interest and understanding of the friction turbine.

2.8 Previous Flow studies

2.8.1 Numerical and Analytical studies

Many investigators during fifties and sixties attempted to analytically and numerically calculate to determine the flow behaviors for laminar and turbulent flow regimes for inter-disk flow of Tesla turbine. Most these studies rely on simplistic flow assumptions due to the limited computation tool capability of their times.

One such prolific investigator of this time is Prof. Warren Rice who has made extensive effort to describe and mathematically model the operational characteristics and summative gross parameters of multiple-disk turbo machinery by employing different sets of formulations. In 1963, he produced a research [17] on how to select the number of disks of air-operated friction pump & compressors based on a steady state, incompressible flow in single inter-disk space by method of surface force determination by solving the differential equations of motion on the radial and tangential coordinates. The study establishes the upper limit of performance parameters such as efficiency and non-dimensional total pressure rise across the pump by assigning frictional losses to occur only between the disk spaces (i.e. entrance & exit losses, windage losses, bearing and housing are neglected). A continuation of this study [18] was performed following similar derivations for reversely operated pump (Multiple-disk Tesla turbine) in 1965 with similar flow considerations. Results of the study indicated that the maximum efficiency and pressure drop of the turbine is attained at the inner fluid exit recess and the tendency of efficiency to decreases as the non-dimensional flow parameter ($Q/\omega r_o^3$) increases is justified. Other W. Rice collaborated works can be found in [19-26].

The various types of pressure losses that exist at the various positions of the turbo machinery are presented with the study of Hasinger et al. [27]. Their determination of the different frictional losses filled the knowledge gap that existed in calculating the realistic performance characteristics of the device based on earlier studies by W. Rice and his associates in which maximum attainable efficiency and power were established. In addition to the aforementioned investigations, various authors attempted to analytically trace out the spiral fluid particle path swept by a fluid particle as it travels from the rotor inlet to fluid exhaust [4, 21, 28]. While others, with the help of Commercial CFD software packages, achieved the same objective [16, 29, 30].

Most of the literatures reviewed by the author follow a two dimensional laminar incompressible flow approach towards solving governing equations to determine the different flow quantities such as Reynolds number, local shear force, radial & tangential velocity components, pressure drop compared to inlet conditions, particle flow paths, etc. [6,31,18,19,28, 32,33,34]. Among them, Soo [34] calculated the radial and axial velocity profiles for a incompressible fluid flowing between one stationary and other rotating disk plates for radially inward and outward flows through first and second order approximation to the Reynolds number.

Still other analytical approaches were made with numerical methods: a finite difference scheme for calculating the radial outward flow between co-rotating disks was presented by Breiter and Pohlhausen [35], a similar method of calculation was applied for radially inward flow by Boyd and Rice [22] using finite difference solution, which modeled the inlet region of the turbine, and take into account the inner region which develop an asymptotic flow for high Reynolds number.

2.8.2 Practical Designs and Experimental Studies

One of the earliest records of experiment undertakings is by N. Tesla himself. He conducted series of experiments from year 1906 to 1914 to investigate the feasibility of the turbine under different operating conditions. According to Tesla, the turbine could achieve a staggering 95 % efficiency which exceeded the conventional turbo machineries of his day. His ultimate goal was to replace the piston combustion engine with a much more efficient, more reliable engine based on his technology. The most efficient piston combustion engines did not get above 27 to 28 percent efficiency in their conversion of fuel to work.

In 1966, Beans [68] tested a 6 inch air turbine by varying the operating conditions such as angular velocity (4,000-18,000 rpm), supply pressure (6895-27,579 Pa) and design variable like disk spacing. In his experiment, he achieved a maximum efficiency of 24% for single stage turbine of specific speed of 0.1 rpm which was considerably lower as compared to steam turbine of similar specific speed which is around 40 to 45%. He also demonstrated the strong relation that flow rate would have on torque acting on rotor disk surface design of Tesla turbine as a result of sharp decline of tangential velocity.

In 1965, Prof. Warren Rice undertook experiments to verify the performance merits claimed by Tesla himself. He replicated the visco-geometric properties under which prior runs were done. The results of his tests confirm the possibility of operating the turbine at almost pure impulse to wholly reactive mode of operation and the diversion of the tested results from N. Tesla's claim of turbine merits at different geometry, flow rate and speed combinations.

Adam et. al. [23] performed tests to experimentally verify radial pressure drop patterns from fluid inlet to exit for a closely separated disk pair with partial flow admission that was earlier presented by Boyd and Rice [22]. Good agreement with the analytical model was reached for the laminar flow. A continuation of this study with little adjustment to the already existing experimental facility of Adam et al. with the mission of determining various fluid regimes, fluid particle streamlines and pressure distribution was presented by Pater et al. [25]. According to them, with the r_i, r_o, and b remaining constant, the combination of flow rate, operating angular speed and kinematic viscosity constant (ν) can be used to design multiple disk turbo-machineries if the flow is ought to remain within laminar flow regime.

2.8.3 CFD Studies

Dependence of operating parameters on the total number of nozzles injecting the working fluid into the inter-disk spacing was analyzed by Lampart et al. [31]with the help of CFD tool using nitrogen as a working fluid for Organic Rankine Cycle. They modeled three different number of nozzles (i.e. 2, 4, 6 nozzles) located at equidistant locations along the circumference of the flow entrance that are tilted at 10 ^{o} from the tangent of the circumference. What they have found in their study was the strong correlation of the reduced number of injecting nozzles to the higher flow efficiencies at different flow conditions. Six-nozzled turbine configuration yielded the shortest flow path which is indicative of the lower efficiency of power transfer and the losses occurring within the flow space which then lead to lower power output compared to smaller number of nozzles with turbine operating under the same flow entrance conditions.

The simulated models exhibited increased flow efficiencies for off-design operating mass flow conditions. This is in good agreement with Rice et al. depiction of higher efficiencies being attained at smaller flow conditions. The study fails to achieve the operational characteristics of the friction-type micro turbine at smaller flow rates close to 0 kg/s.

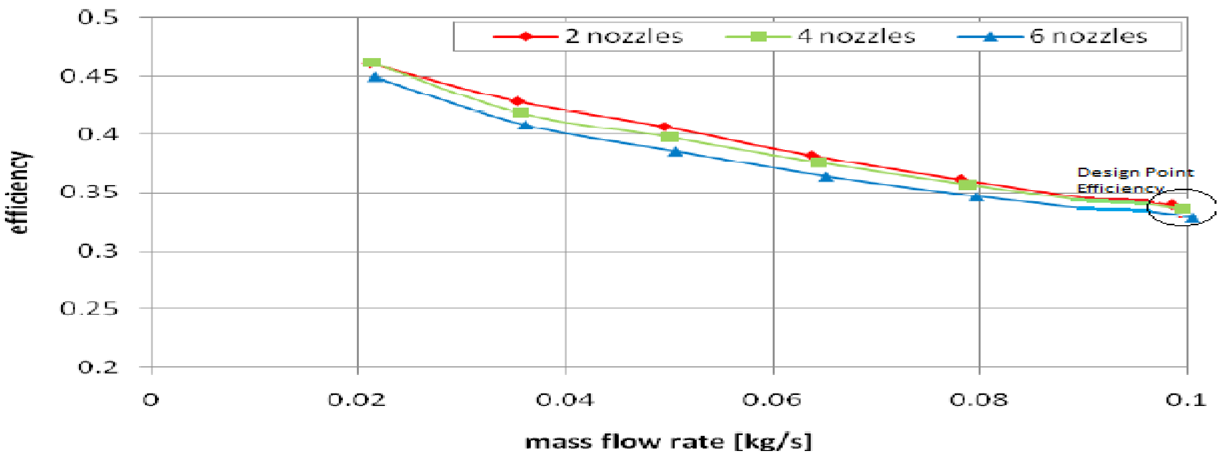

Figure 2-4: Flow Efficiency [-] for 120 mm Disk Diameter CFD Models as a Function of Mass Flow Rate [kg/s] at a constant disk rotation rate of 24,000 rpm; The System Supplied From Two, Four And Six Nozzles [16]

Different investigators such as Harwood [37] and J.H. Morris [38] explored the operational characteristics of the turbine as flow closed to 0 kg/s and determined the efficiency to approach 0 at these conditions. This is contradicts earlier investigation by Rice and Crawford [39] which stated the efficiency of the turbine to keep incrementing as the flow reaching to null flow rate state.

2.9 Losses

A significant reduction of multiple disk turbine efficiency is mostly attributed to the losses that occur on the different sections of turbine's circuits. The rotor alone has been proven to be highly efficient going high above 90% efficiency exceeding that of the normal performance characteristics of conventional bladed turbines. Actual overall efficiency of Tesla turbine could fall below 10%. Rice remarked that this excessive drop in efficiency comes from mainly losses occurring at the junction between the nozzle exit and rotor entrance. These losses are manifested in the form of pressure and enthalpy drops.

Guha & Smiley, by designing a nozzle that utilizes a plenum chamber inlet, have been able to reduce the total pressure losses to about less than 1%. In normal case, the total pressure losses that exist within the fluid inlet and rotor entrance region are between 13-34 % which is a major source of efficiency drop. They have also attested their design by running experiments that have demonstrated enhanced uniform jet generating capability of the improved design.

In general, the losses that occur in multiple disk turbines can be categorized into four according the location on which the specific type of losses would exist.

a. Connecting hose losses before entrance to the nozzle

These specific types of losses occur as a result of bends, leaks and discontinuities within the fluid transport duct from the fluid source at higher pressure level. The losses may occur as a result of:

i. Friction against the inner wall of the connecting duct causing mechanical energy loss. The magnitude of this loss can be estimated by using Darcy Weissbasch relation for frictional pressure drops by assuming pressure loss coefficient for the inner wall.

$$\Delta p_f = \frac{1}{2} k_f . \rho . u^2 \tag{2.2}$$

where:-

$$k_f = f.\frac{L}{d}$$

ρ= average density of the fluid entering the nozzle

u= average axial velocity of fluid stream

L= Duct length

d= duct inner diameter of the duct cross section resulting in viscous eddies

For abrupt enlargement of flow cross section, the pressure losses can be estimated from the relation given below. [40]

$$\Delta \boldsymbol{p_a} = \boldsymbol{k_u}.\boldsymbol{\rho}.\boldsymbol{u_i}^2 \tag{2.3}$$

$$k_u = (1-\alpha^2)^2$$

Similarly, for abrupt contraction of cross section in the flow direction, the pressure losses can be estimated from the following equations. [40]

$$\Delta \boldsymbol{p_a} = {}^{\boldsymbol{1}}/_{\boldsymbol{2}}\,.\boldsymbol{k_d}.\boldsymbol{\rho}.\boldsymbol{u_n}^2 \tag{2.4}$$

$$k_d = -0.33\alpha^{-2} - 0.18\alpha^{-1} + 0.5$$

Table 2-1: Calculated Loss Coefficients for Inlet and Nozzle

Loss Mechanism	*symbol*	*Loss Coefficient*
Friction against wall	k_f	0.27
Changes in inlet duct diameter in three places(all referred to the velocity in the 6 mm diameter section)	k_u	0.86
90 ° bend in the elbow	k_b	1.65
90 ° bend in the nozzle	k_b	0.94

Table 2-2 presents general loss coefficients used for pressure loss calculation by Guha and Smiley [40] for improving the nozzle performance characteristics.

ii. Change of fluid direction as a result of bends in the flow duct resulting uneven radial pressure distribution from inner to the outer curvature of the duct wall. The disparity in pressure distribution arises from difference in centrifugal force acting on the fluid particle as a result of peripheral velocity deviation with respect to a bending center point.

iii. Losses related to leakages in seals fitted to the connecting hose at both ends with working fluid bypassing the rotor not performing useful work.

b. Losses occurring between nozzle inlet to rotor exit sections

i. Loss of available energy due to entropy generation in the nozzles

ii. Losses due to partial admission as a consequence of finite thickness of the rotor disks at the nozzle-rotor junction and limited flow introduction due to the finite number of nozzles spanning the disks' peripheries.

iii. Losses related to energy dissipated to unions and spacers

iv. Windage losses: Negative zone of wall stress causing fluid to be entrained by the disks producing local blower effect. Figure 2-7 shows the stress distribution on a disk plane on which negative stress distributions can be discerned near the periphery of the flow space colored in blue and light blue which is clear indicative of momentum transfer from the disk onto the fluid rather than from the fluid to the disk.

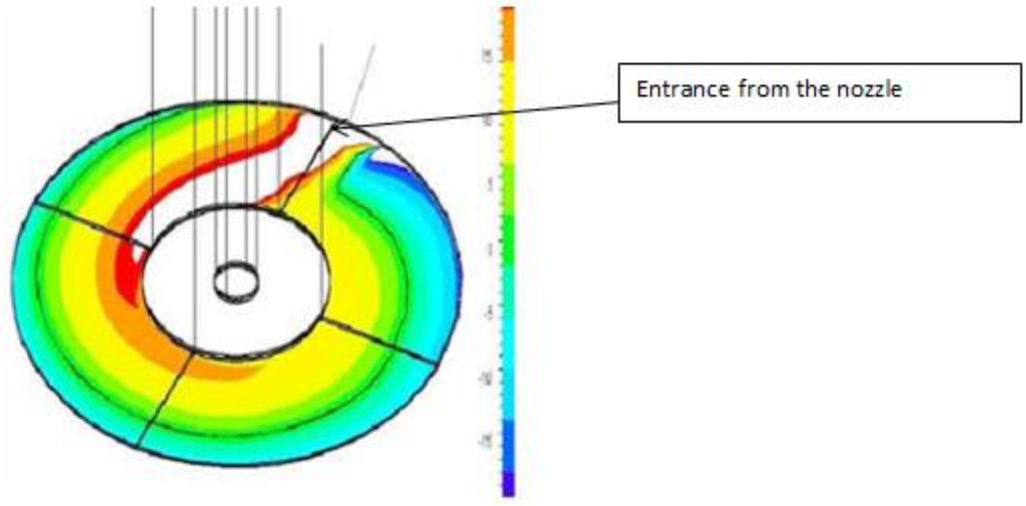

Figure 2-5: Wall Stress Distribution Across The Disk Surface [26]

v. Energy loss as a consequence of momentum exchange between previously injected fluid particles travelling in the inter-disk space and the freshly injected fluid particles.

vi. Entropy generation in the laminar sub layer of turbulent boundary layer near the disk surface extending to energy dissipated due to shear forces on the outer surface of the rotor, on the sides of the outer disks and edges of all disks and friction interaction of the fluid between the housing and the fluid. [6]

c. Exit and miscellaneous losses

i. Losses due to uncontrolled diffusion in the rotor exit. The change of flow direction from radial to axial direction produces secondary flows apart from the high swirling flow at the disk outlet. [6] & [18] such losses can be minimized by allowing the fluid to stay longer in the inter-disk space by allowing the turbine to run at higher operating speeds.

ii. Mechanical losses at the bearings

2.10 Flow Regime transition

It is established that a wide range of types (or regimes) of flow can occur between co-rotating disks including wholly laminar flow, laminar flow with regions of recirculation, wholly turbulent flow, laminar flow proceeding through transition to turbulent flow, and turbulent flow proceeding through ‘‘reverse transition’’ or ‘‘relaminarization’’ to laminar flow [9]. The flow through the disks has been studied experimentally and theoretically.

The flow is turbulent in the nozzle area and gradually becomes laminar in the disk flow space. The velocity profile can be parabolic, inflected or nearly flat, and many combinations of these features have been found to exist [41].

At the exit to the nozzles and entrance to the disk assembly, turbulent flow conditions apply as the flow meets restriction from leading edge of the disks. The no-slip condition is applied to the disk walls which means maximum shear force assumptions hold for the disk surface. As the flow progresses from the leading edge, boundary layer will form on the adjacent disk surfaces growing to contain the full inter-disk span becoming a fully developed laminar flow. At this point, the inertial fluid forces are dominated by the viscous forces that dissipate turbulence effects.

Further down the flow path, the radial velocity component of the fluid stream increases, after which the boundary layer thickness reduces as the inertial forces start to dominate the viscous forces creating inviscid regions near the fluid exit. The level of turbulence reached at this point, compared to the entrance conditions, is relatively lower. With high acceleration, the flow vortex in the turbulent boundary layer became stretched and the vorticity is dissipated through the viscous effects, this process is called reverse transition or relaminarization [6]. Figure 2-6 illustrates the described phenomenon.

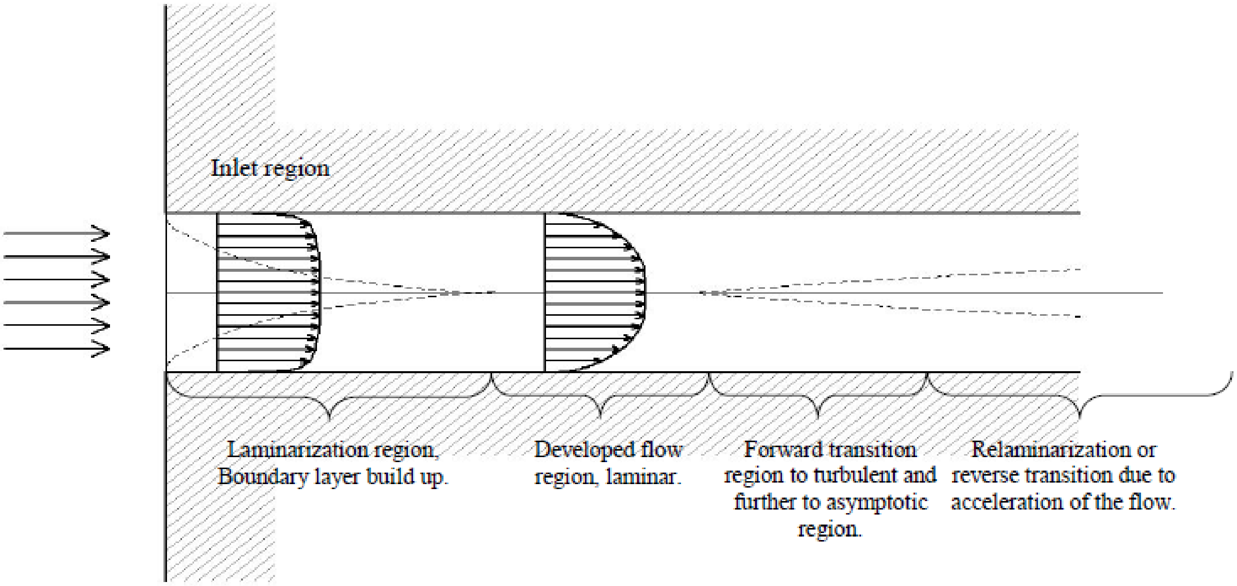

Figure 2-6: Laminarization and Transition Modes Present in a Disk Gap [6]

The benchmark for categorizing the various flow regimes that exist at various radial locations is not absolute as different authors provided their visco-geometric conditions based on their design methodologies and sizing criteria used. Adams and Rice proposed a limit for the laminar flow assuming that the inflection of the profile is the initial of instabilities, and this occurs approximately at a $Re_b=10$, since all calculated radial velocity profiles are after that inflected [6].

$$Re_b = \frac{\omega . b^2}{\nu}$$

Where: ω is operational rotation speed of the turbine at design condition

b is the inter disk spacing

ν is the kinematic viscosity of the working fluid disk row entry point at the design pressure and temperature

Re_b is a non-dimensional Reynold's number associated with the gap

Other authors such as Tabattatai and Pollard, defined another Reynolds number parameter, $Re_{r,l}=800$ as the upper limit for laminar flow regimes.

$$\boldsymbol{Re_{r,l} = \frac{\omega r_{in} . b}{\nu} < 800} \qquad (2.5)$$

The above assumption takes into account that at the inner radius of the disk (r_{in}), the fluid tends to attain maximum relative tangential velocity coupled to losses occurring at the same radial position, flow will be more likely to be disturbed transitioning to turbulent regime.

Wu, after considering all available experimental and analytical evidences, the visco-geometric number, **α,** proposed by Nendl [42], most adequately characterizes the flow regimes.

$$\boldsymbol{\alpha = \frac{\bar{U}}{r}\frac{b^2}{\nu}} \qquad (2.6)$$

Where: $\bar{U}$ is the average tangential velocity between the peripheral and inner radial tips flow locations

b is the interdisk spacing

r is the mid radius between disk row inlet and exit area

According to Nendl's flow regime prediction criteria, **α** less than 10 represents laminar flow while the other flow category criteria are listed below.

α<10…………………Laminar flow

10<α<20………….....Transient flow

α>20………………...Turbulent flow

As opposed to the above mentioned criteria, Couto et al. [43] designed a Tesla turbine by considering the same flow transition assumptions adopted from conventional pipe flow theory.

Chapter 3

3 Design of Tesla Turbine

3.1 Introduction

Since its inception in 1909, the design of Tesla type turbo machinery is mostly reliant on intuitive predictions coupled with experimental test runs with presumed controlled operating variables. Much of the publicized researches are more enchanted towards identifying potential control parameters and through determination of such parameters, the description of flow between any two disk rotors had been attempted. Researches in the 60s and 70s, concentrated their attention into solving the governing Navier Stokes equations, under certain flow assumptions, with various sets of numerical methods. In any case, there hasn't been any standardized design procedure; as it was developed for conventional types of turbo-machineries which were predominantly based on momentum exchange between a fluid and energy generation equipment.

Lately, there is a renewed interest among the academics and Nikola Tesla work fans to retrospect and improve some of his prior inventions to apply them to solve some of the current energy challenges. One such interest group is the Tesla engine builders association (TEBA) which is working towards hybridizing the gasoline-fired Tesla engine operated cars with electricity. Nevertheless, there is a perceived need to keep some of the innovative design techniques secret within some academic and Tesla-builder circles.

As opposed to this, some investigators such as Couto et al. reviewed the physical principles behind the Tesla Bladeless Turbine using only basic fluid mechanics. By considering the relative motion of rotating surfaces, their research sets up the transport equations describing the flow between parallel rotating disks making it easy to estimate the boundary layer thickness under laminar and turbulent regimes, leading to expressions yielding the width between consecutive disks. H.S.Couto explained how to calculate the total number of disks that is required to maintain a given desired performance. In addition, the research also asserts the device's behavior to act as an air compressor or water pump and its versatility as a unit source of rotating motion running under a very wide spectrum of fluids and fuels in the wider sense.

In general, designing a Tesla turbine includes determination of the available power from flow tangential velocity components, and selection, sizing and deciding on the following parameters:

- Estimation of the maximum expected power from the fluid stream
- Sizing the inter-disk spacing based on the prevalent flow velocity components relative to the rotating disk surface
- Deciding the fluid inlet and exit diameters
- Determination of a generalized fluid flow regime to represent the flow condition
- Selecting the number of nozzles
- Selecting effective nozzle entrance angle for introducing the fluid jet into the flow space

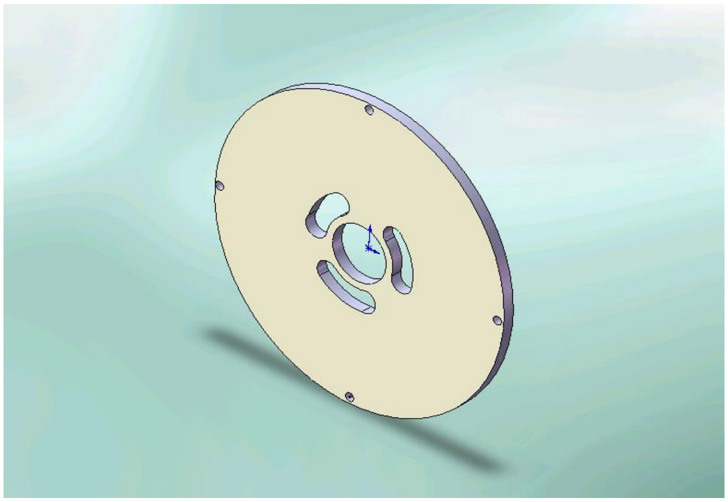

Figure 3-1: Isometric View of a Single Disk of Tesla Turbine

- Determining the thickness of each disk that effectively resists the radial inward force on turbine rotor edge surfaces without causing any wrapping thus avoiding flow disturbance downstream
- Calculating the disk to casing clearance
- Selecting the type of prime over fluid with which to operate
- Choosing the right surface roughness for the disk surface
- Limiting the rotor inlet pressure and absolute velocity
- Calculating the total number of disks to meet an expected power requirement
- Selecting the design operating speed

3.2 Design Assumptions

Similarly, the idealizations that would apply to the flow in between the disks include,

- There would be full peripheral admission. The nozzles would eject fluid to the inter-disk space uniformly and ventilation effect that would otherwise trigger fluid steam slowdown is avoided.
- The type of flow assumed is incompressible and viscous flow.
- The entire space between the disks is occupied with the working fluid; No flow separation between the rotating fluid stream and the disk faces.
- No flow leakages would occur either before or after the rotor. All the flow would be used to produce useful work on the rotor disks.
- There wouldn’t be temperature increase or decrease due to entropy creation or destruction in the flow.
- Axial variations in pressure, velocity and mass flow rate conditions that would occur as result of surface tension and relative disk rotation are neglected.
- Disk spacers, essentially placed between any two rotor disks, that introduce disruption to the spiral fluid stream are absent in the conceptual design.

3.3 Estimation of the Rotor’s Outer & Inner Disk radiuses and Selection of Operating Angular Velocity

The fluid will be ejected to a disk row with the help of injection nozzles. The geometry of the nozzles is designed such that the selected taper angle avoids choking at the discharging throats. The throat exit velocities, in their respective tangential and radial directions, have been used to calculate the available power in the fluid.

$$U_O = 209.33\, m/s$$

$$V_O = 33.15\, m/s$$

The operating angular speed of the turbine is selected to be 10,000 rpm which is in the mid operating speed range for a normal Tesla turbine.

$$\omega_d = 1046.67 \frac{rad}{s}$$

As it has been demonstrated in section 2.4, the total transferred power to turbine shaft has been represented as the difference in momentum of the tangential fluid components between disk row entrance and exit velocities.

$$P_{out} = \dot{m}.\omega.(r_o U_o - r_i U_i)$$

The maximum extracted mechanical work can be achieved when the fluid has already imparted its momentum to the neighboring disks in which case the relative tangential velocity at the most inner radius vanishes to zero. Note that energy transfer can only take place only when there is a positive tangential velocity gradient between the inter-disk fluid stream and torque conducting energy surface.

$$\boldsymbol{P_{out-max}} = \dot{m}.\omega.(r_o \boldsymbol{U_o}) \qquad (3.1)$$

Based on the above relation,

$$P_{out-max} = 9150.54\,\boldsymbol{watt}$$

Estimation of the peripheral diameter of the rotor disk and fluid exit radius are prior parameters to be decided in the designing procedure. Selection of both dimensions is at the designer's disposal which considers material cost and space factors. Once either of the extreme dimensions is decided, the other can be calculated based on recommendations put forward by prior studies.

Initial estimate of rotor disk outer diameter is decided to be 12 cm.

$$D_0 = 0.12\,m$$

This initial diameter guess is subjected to change later upon the earlier mentioned consideration points.

According to Hasinger et al. [27] practical rotor efficiency could reach 60 % if the flow coefficient (radial inlet velocity to rotor tip speed) remains between 0.02 to 0.03 and the disk radius ratio is kept between 0.33 -0.5 for best performance.

$$\boldsymbol{radius\ ratio(\ RR)} = \boldsymbol{\frac{R_i}{R_o}\ where\ 0.33 < RR < 0.5} \qquad (3.2)$$

On similar note, from the numerical solutions of Boyd and Rice, it can be found that above a certain value of the RR, i.e. RR> 0.5, the axial component of velocity is almost zero. This limit sets the condition for avoiding large exit flow vertices [28].

The radius ratio is selected close to 0.5 as it allows more fluid residence time in between the disk spaces at the same time minimizes exit swirl losses. More rotations, hence, higher energy transfer could be achieved when the fluid is allowed to rotate in the inter disk spacing.

$$RR = 0.528$$

$$D_i = D_o . RR$$

The same radius ratio has been used to estimate the inner radial dimension in one of the practical design configurations by Lemma et al. [44] to avoid large outflow vortices.

The operating fluid with which the rotor disks are propelled to produce power is compressed air. It has been demonstrated in the foregoing discussions that every Tesla turbine is unique according to the fluid with which it will be operated. Inter-disk space varies depending on its thermo-physical properties.

Turbine entrance pressure condition is achieved through laboratory compressor which raises the total pressure of air to its entrance condition. Harwood [37] gives the relation between these two variables in the following way by considering the flow in inter-disk space to be incompressible.

$$\boldsymbol{P_{inlet} = P_{max} + {}^{1}/_{2} \cdot \rho_{air} V_{av}^2 = \frac{\rho_{air}\, \omega^2 (R_o^2 - R_i^2)}{2} + {}^{1}/_{2} \cdot \rho_{air} .(\omega R_o)^2} \qquad (3.3)$$

Plugging in the known physical parameters the design entrance pressure of the turbine is found from,

$$P_{inlet} = \frac{\omega^2 . \rho_{air} . (2R_o^2 - R_i^2)}{2} = 14.08\ kPa$$

Since the fluid discharges to atmospheric conditions, the calculated amount of static pressure must be available for expansion at the inlet to the rotor. In other words, the total pressure at the inlet to the turbine stage is the local atmospheric condition plus this static pressure.

3.2 Estimating Boundary Layer Thickness and Total Number of Disk

The fluid adherence to the wall (i.e. the “no-slip” condition) is the basic assumption behind the Tesla turbine. As the fluid rotates over the energy transferring surfaces, the disk will acquire the velocity of the fluid imparted to it. For a more effective momentum transfer to take place, the flow should be mainly laminar in the majority of flow domain [9].

For a given mean flow velocity at the turbine inlet, in theory, the turbine rotor will start rotating speeding up until reaching that tangential velocity when the relative velocity between the disks and the flow is so that that there will be no energy addition back to the fluid stream in every radial span along the disk surface. From this moment and on, velocity relative to the disks will be that of the fluid penetration velocity between consecutive disks and this velocity is to be taken into account to calculate the design Reynolds number.

The pipe flow theory is instrumental in characterizing the prevalent flow and assists in the determination of boundary layer thickness which is in turn indicative of disk spacing. The Darcy Weissbasch frictional coefficient is derived in terms of representative geometrical dimensions for Tesla turbine. Note that a bulk type method of analysis which utilizes friction factor works best for laminar flows. By applying similar method unknown degree of uncertainty is introduced in case of turbulent flows.

$$\boldsymbol{f_{lam} = \frac{64}{Re} = \frac{64.\mu_{air}}{\rho_{air}V_{air-outlet}D_{eff}} = \frac{64.\mu_{air}}{(\rho_{air}((U-\omega.r_o)^2_{outlet}+(V)^2_{outlet})^{1/2})D_{eff})}} \tag{3.4}$$

where,

$\rho_{air} = Density\ of\ air$ [kg/m^3]

$V_{air-outlet} =$

$relative\ velocity\ magnitude\ of\ air\ at\ the\ outlet$[m/s]

$D_{eff} = Linear\ characteristic\ dimension$ [m]

$\mu_{air} = Dynamic\ viscosity\ of\ air$ [kg/s^2]

The hydraulic diameter is used to determine an effective diameter which then serves as a representative diameter of an imaginary duct that will have same flow conditions as the one in the turbine. The hydraulic diameter considers the flow cross-section area and wetted area by the rotating fluid.

$$\boldsymbol{D_h = \frac{4.A_{flow}}{P_{wet}}} \tag{3.5}$$

where,

$D_h = Hydraulic\ diameter\ of\ a\ representative\ duct$

$A_{flow} = Effective\ flow\ area\ of\ the\ air\ stream$

$P_{wet} = Wetted\ perimeter\ of\ the\ flow\ space$

Substituting the variables for flow cross section and flow wetted perimeter the equation takes the following form.

$$\boldsymbol{D_h = \frac{4.(\pi D_o.b)}{2.(\pi.D_o+b)}} \tag{3.6}$$

Usually, D_o is much greater than the rotor gap. Hence, the equation reduces to,

$$\boldsymbol{D_h \cong 2b} \tag{3.7}$$

The hydraulic diameter assumption taken is appropriate for flow through a wide rectangular duct. This realistic assumption is based on prior theoretical and experimental studies conducted by Ladino [6], Rice[18], Harwood [33] and Bryan [37].

Table 3-1: Summary of Design Input Parameters

Property	**Unit**	**Value**
Inlet pressure	[kpa]	14.108
Inlet Fluid temperature	[°C]	27
Working Fluid	-	Air
Nozzle angle	[°]	9
Rotor Outer diameter	[m]	0.12
Rotor Inner diameter	[m]	0.0634
Fluid mass flow rate	[kg/s]	0.4125
Rotor angular speed	[rad/s]	1046.67
Number of nozzles	-	2, 4, 6

The effective diameter can then be computed as a fraction of the hydraulic diameter.

$$\boldsymbol{D_{eff} = (\tfrac{2}{3})D_h} \tag{3.8}$$

Substituting equation (3.6) in equation (3.7),

$$\boldsymbol{D_{eff} = \left(\tfrac{4}{3}\right).b} \tag{3.9}$$

The Reynolds number is calculated based on the above effective diameter as a linear characteristic length.

$$\boldsymbol{Re = \frac{(\rho_{air}V_{air}D_{eff})}{\mu} = \frac{(4.\rho_{air}((U-\omega.r_o)^2_{outlet}+(V)^2_{outlet})^{1/2}b}{(3\mu)}} \tag{3.10}$$

The absolute tangential velocity component for the disk row exit, U, is calculated from the design power requirement related by equation 3.1. The design power requirement in this case is 8 KW. Note that in calculating the Reynolds number, the relative velocity component is only effective in tangential axis while the radial component will undergo acceleration.

3.2.1 Turbulent velocity boundary layer thickness

The turbulent boundary layer thickness can be estimated using the following correlation [45] as referenced in [43].

$$\boldsymbol{\delta_{turbulent} = 0.526.r_k\left(\frac{\mu}{\rho {r_k}^2\omega}\right)^{1/5}} \tag{3.11}$$

where:

$\delta_{turbulent}$ = Turbulent boundary layer thickness measured from entrance of rotor surface

r_k = Local disk radius

μ =Working fluid dynamic viscosity coefficient

ω= Angular velocity

ρ= Density of air at the prescribed pressure and temperature

A plot depicting the variation of turbulent boundary layer thickness at different radial spans is given in figure 3-2, for various operating angular speeds. As can be evidenced from this graph, the turbulent boundary layer thickness grows at a decreasing rate as the operating angular speed range is pushed further.

Since Tesla turbine is inward-flow turbo machinery, the local disk radius span r_k is measured from the periphery into central exit as opposed to Tesla pump.

The range within which this equation is applicable is clearly unknown and sometimes, renders considerably larger disk gap space estimates as a result of thicker boundary layer predictions. The applicability of this equation is more justified when a more viscous working fluid such as water or oil is used as a motive agent where by the turbulent boundary layer could be estimated with acceptable precision.

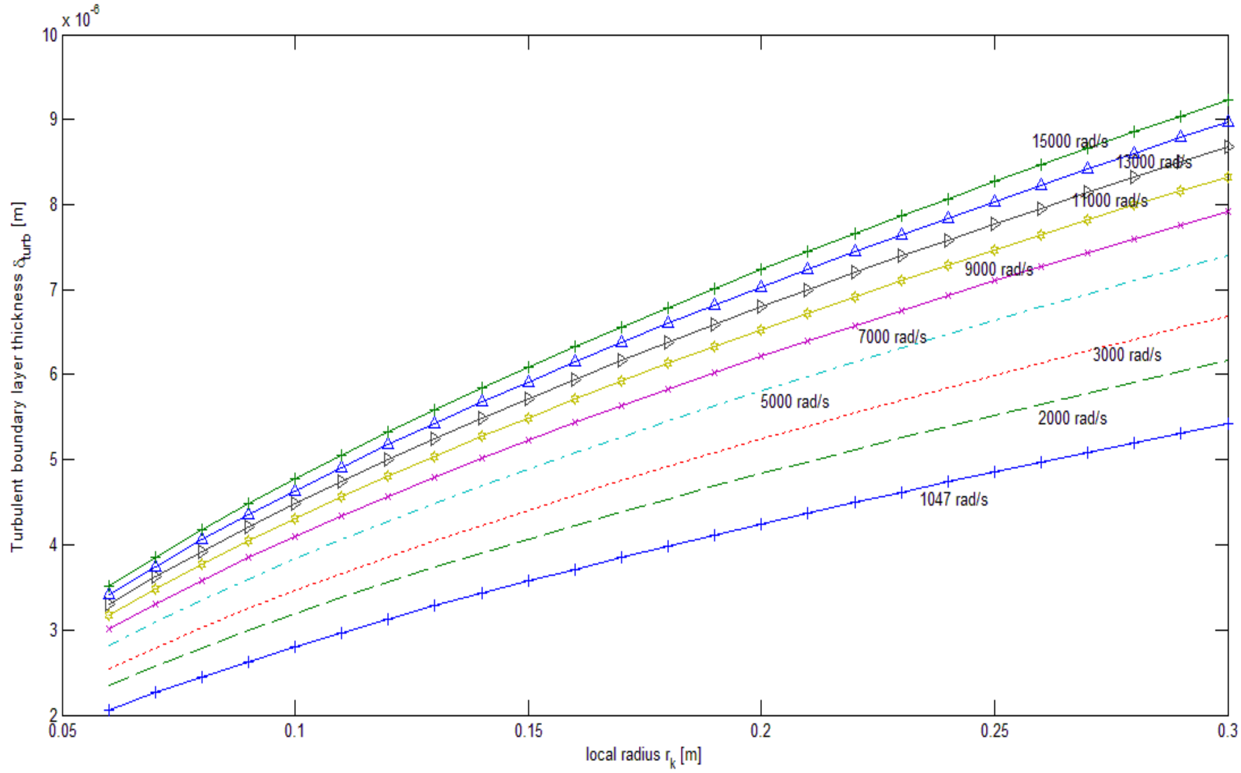

Figure 3-2: Turbulent Boundary Layer Growth [m] over Different Radii[m] and Operating Angular Speeds [rad/s]

With this in mind, the turbulent boundary layer thickness to be adopted, if the flow falls in the turbulent flow regime, is not to be double the boundary layer thickness (as is the case for laminar boundary layer) but rather a thickness equaling to its layer thickness. This argument takes to account the considerable variations between the two estimates spanning up to ten times that taken for laminar cases.

3.2.2 Estimating the laminar velocity boundary layer thickness

Observing the velocity components of the flow stream at the forefront edge of the rotor, the radial component is considerably smaller than the tangential component of the velocity magnitude. This is due to the fact that the nozzle entry angle must stay between 6 to 15 ^{o} from the tangent of the rotor assembly casing in order to ensure larger reaction coefficient for the rotor.

The tangential component is mainly used to produce torque to transform the fluid kinetic energy into useful form. While on the other hand, the radial component aids the fluid to be entrained to the central exit. By considering the disk separation space to be fully occupied by the working fluid and the flow is not exceeding sonic limit, the conservation of mass principle can be applied radially by taking the inlet and exit flow areas.

$$\boldsymbol{U_{o,r}.\pi D_o b = U_{i,r}.\pi D_i b} \tag{3.12}$$

Where, U_o and U_i are the radial velocity components at the rotor entrance and exit, respectively. But,

$$U_{o,r} = Usin(\alpha)$$

$$U_{i,r} = \frac{U_{o,r}}{RR} = \frac{U_o sin(\alpha)}{RR}$$

$$U_{i,t-rel} = U_{i,t} - \omega.R_i$$

$$U_i = \sqrt{{U_{i,r}}^2 + {U_{i,t-rel}}^2}$$

$$\boldsymbol{U_i = \sqrt{(U_{i,t} - \omega.R_i)^2 + (\frac{U_o sin(\alpha)}{RR})^2}} \tag{3.13}$$

From the moment the disks reaches a uniform angular velocity and on, the only non-zero relative velocity is the one between each disc and the flow inside the passages between consecutive disks flowing toward their center until reaching their exit port.

The boundary layer thickness can be calculated from Blasius solution which is used to estimate the boundary-layer thickness over a flat plate,

$$\boldsymbol{\delta_{laminar} = 5.(\frac{\upsilon.X}{U_i})^{1/2} = 5.(\frac{\upsilon.X}{((U-\omega.r_o)^2_{outlet}+(V)^2_{outlet})^{1/2}})^{1/2}} \tag{3.14}$$

where:

ν is working fluid kinematic viscosity coefficient
U_i is the inlet flow velocity
X is the length on which full boundary thickness develops

Notice that selected a disk separation distance guarantees a laminar regime up to the disk row exit.

$$\boldsymbol{\delta_{laminar} = 5.(\frac{\upsilon.(R_o - R_i)}{U_i})^{1/2}} \tag{3.15}$$

The viscosity (ν) in equation 3-14 is directly dependent upon temperature of the working medium and to smaller extent to the pressure. Gas viscosity varies only with temperature. The actual viscosity of the air can be approximated by referring to viscosity of air at reference temperature. For our purpose, the Sutherland law is used to calculate dynamic viscosity of the air stream at 27^{o}C.

$$\mu \approx \frac{\mu_{o}.\left(\frac{T}{T_O}\right)^{3/2}(T_O+S)}{T+S} = \frac{1.729x10^{-5}.\left(\frac{298}{273}\right)^{\frac{3}{2}}.(273+110)}{(298+110)} = 1.85103x10^{-5}\frac{kg}{m}.s \quad (3.16)$$

where:

To reference absolute temperature in ^{o}k (273 ^{o} K)

S= 110 ^{o} K

μ_o = Viscosity at the reference temperature condition

On a similar note, the density of air at the existing pressure condition is determined from ideal gas law.

$$\rho_{air} = \frac{P_o}{R.T_{air}} \quad (3.17)$$

Boundary layer will from starting from both leading edges of adjacent disk surfaces to occupy the total gap space. Hence, the inter disk spacing must be sized twice this laminar boundary layer thickness.

$$b = 2.\delta_{laminar} \quad (3.18)$$

Now, the flow must be checked for Reynolds number whether we have made the right assumption for laminar regime.

$$Re = \frac{(4.\rho_{air}V_{air}b)}{(3\mu)} = \frac{(4.\rho_{air}((U-\omega.r_o)^2_{inlet}+(V)^2_{inlet})^{1/2}b)}{(3\mu)} \quad (3.19)$$

$$Re = 3{,}141$$

Clearly, the flow between the inter-disk slit falls in the turbulent regime since the Reynolds number is greater than 2300 laminar limit set by Couto et al.

As an alternative to this conventional model, the visco-geometeric number, α, is calculated and compared against Nendl's flow transition criterion. (see section 2.12)

$$\alpha = 44.6$$

Since this number exceeds the 20 threshold limit for turbulent flows, the flow can be treated as fully turbulent problem.

3.3. Estimation of the total number of disk

The required number of disks for turbine rotor is estimated by deriving a relation between the total air mass flow rate and the Reynolds number at the design flow rate condition.

Then the mass flow rate through a gap is

$$\dot{\boldsymbol{m}}_{\boldsymbol{air}} = \rho_{\boldsymbol{air}} \boldsymbol{U}_{\boldsymbol{o}} \boldsymbol{A}_{\boldsymbol{flow}} = \rho_{\boldsymbol{air}} \boldsymbol{U}_{\boldsymbol{o}} \boldsymbol{\pi} \boldsymbol{D}_{\boldsymbol{o}} \boldsymbol{b}.\boldsymbol{N}_{\boldsymbol{gap}} \tag{3.20}$$

$$U_o b = \frac{\dot{m}_{air}}{\rho_{air} \pi D_o . N_{gap}}$$

where:

N_{gap}= Number of gap between the consecutive disks

D_o= External disk diameter

Similar equation for U_ob can be derived from the Reynolds relation in equation 3-19

$$\boldsymbol{U}_{\boldsymbol{o}} \boldsymbol{b} = \frac{3}{4} \frac{\boldsymbol{\mu}.\boldsymbol{Re}}{\rho_{\boldsymbol{air}}} \tag{3.21}$$

Equating equation 3-20 to equation 3-21, the number of disk gaps can be calculated.

$$\boldsymbol{N}_{\boldsymbol{gap}} = \frac{4}{3} \frac{\dot{\boldsymbol{m}}_{\boldsymbol{air}}}{\boldsymbol{Re}.\boldsymbol{\mu}.\boldsymbol{\pi} \boldsymbol{D}_{\boldsymbol{o}}} \tag{3.22}$$

The required total number of disks is one more than the number of gaps.

$$N_{disk} = N_{gap} + 1$$

Once the total number of disks is determined, the torque that would be achieved from the disk-shaft assembly is calculated by summing up torque contribution from individual disks.

Moment coefficient C_M for turbulent flow across a disk gap is described as in equation 3-23 [43]

$$\boldsymbol{C}_{\boldsymbol{M}} = \frac{\boldsymbol{2}.\boldsymbol{T}}{\left(\frac{1}{2}\right) \rho_{\boldsymbol{air}} \omega^2 \boldsymbol{R}_{\boldsymbol{o}}^5} = \frac{\boldsymbol{4}.\boldsymbol{T}}{\rho_{\boldsymbol{air}} \omega^2 \boldsymbol{R}_{\boldsymbol{o}}^5} \tag{3.23}$$

Where,

$$\boldsymbol{C}_{\boldsymbol{M}} = \boldsymbol{3.87} (\boldsymbol{Re}_{\boldsymbol{o}})^{-\boldsymbol{1}/\boldsymbol{2}} \tag{3.24}$$

T= Torque determined from a single disk wetted on both sides

Re_o = Reynolds number associated to outer disk radius

Equating the two equations,

$$\boldsymbol{T} = \boldsymbol{0.9675}.\left(\frac{\rho_{\boldsymbol{air}} \omega^2 \boldsymbol{R}_{\boldsymbol{o}}^5}{\boldsymbol{Re}_{\boldsymbol{o}}^{1/2}}\right) \tag{3.25}$$

But,

$$Re_o = \frac{R_o^2 \omega}{\nu}$$

The total torque produced thus depends on mainly certain design variables such as operating angular speed & disk outer radius and certain physical properties such as density and kinematic viscosity.

$$\boldsymbol{T = 0.9675.\left(\omega^{3/2} R_o^4 \left(\rho_{air}.\mu\right)^{1/2}\right)} \tag{3.26}$$

The total torque delivered by the disk row assembly is given by,

$$\boldsymbol{T_{total} = 2(n-1).T} \tag{3.27}$$

The power generated by the total torque, Po, is

$$\boldsymbol{P_{out} = \omega T_{total}} \tag{3.28}$$

In due process of designing the turbine, it was determined that the rim diameter of the disk , which is cut out of a piece of sheet metal, is directly related to the total cost of rotor. Designing a Tesla turbine with smaller rim diameter rotor renders larger number of disks while at the same time having larger sheet metal area. The figure 3-3 depicts this scenario.

Alternatively, going for higher peripheral disk diameter would introduce certain unaccounted axial forces from the fluid flow onto the disks. This in turn would lead to warping consequently triggering irregularities with the inter-disk flow area on the different axial locations. The cumulative effect from is higher loading on some of the disks while negligible useful force on the others.

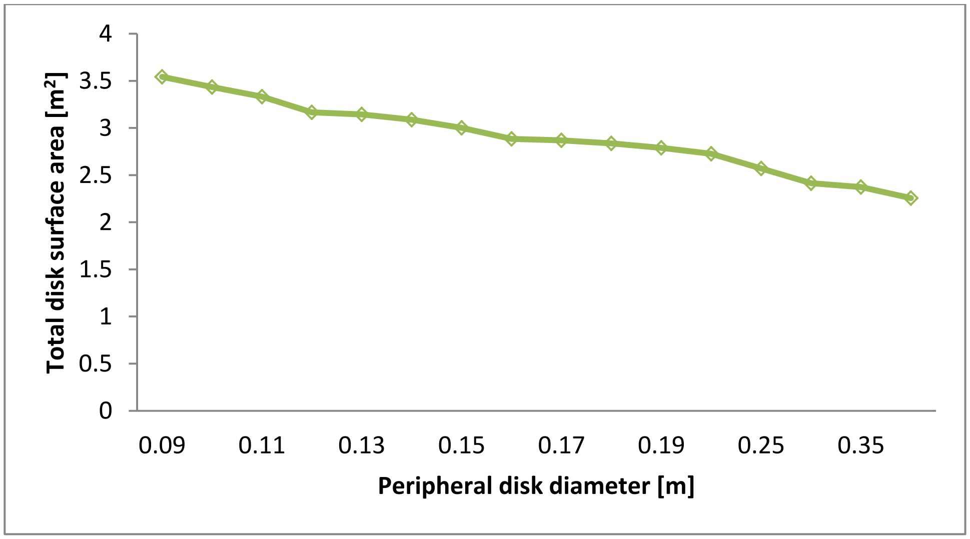

Figure 3-3: Total Disk Flow Area Variation with Peripheral Disk Diameter

Based on the stated limiting parameters, the peripheral disk diameter is selected as 0.2 m. The calculated design variables with this parameter are tabulated below.

Table 3-2: Summary of Calculated Tesla Turbine Design Parameters

Design Variable	Unit	Value
Peripheral disk diameter	m	0.2
Inner disk diameter	m	0.1056
Rotor entry angle (α)	°	9
Rotor angular speed	rad/s	1046.67
Air flow rate	kg/s	0.4125
Inter disk spacing	mm	2.2
Reynolds number	-	4925
Number of disks	-	14
Torque produced from single disk	N-m	0.17
Total torque produced from disk assembly	N-m	2.379
Turbine power	Watt	2490

3.4. Disk Assembly sideway clearance (s) and Radial clearance (σ)

For calculating the disk row to housing clearance, the entire disk assembly is assumed as a single disk set on rotational motion encapsulated in a cylindrical casing. The viscous momentum exerted on the walls of the disk induces shear stress on these surfaces.

Figure 3-4 demonstrates the disk row's side (s) and radial tip (σ) clearances as referenced from the static casing housing.

No empirical relation has been determined for estimating the disk assembly radial clearance (σ) for the turbine. A value of 1 mm has been taken for geometric construction.

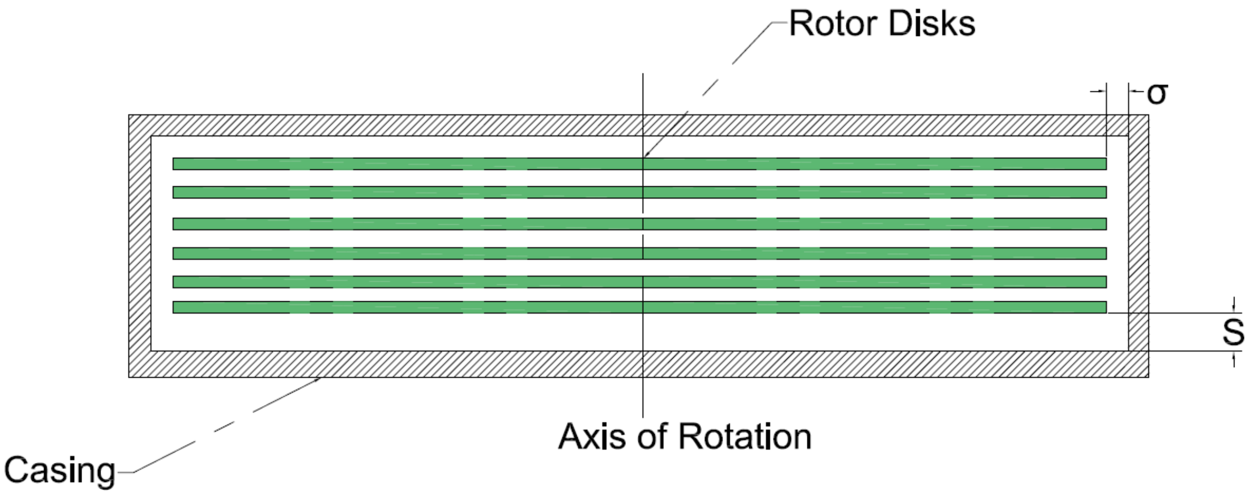

Figure 3-4: Sketch of an Encapsulated Disk for Symbols Description

By equating the momentum coefficient derived from viscous force torque acting at s distance from the disk row to the momentum of coefficient indicated by equation 3-29, the lateral clearance can be computed [43].

$$C_M = 3.87(Re_o)^{-1/2} = \frac{2.\pi.R_o}{s.Re} \qquad (3.29)$$

$$s = \frac{1.6227.R_o}{Re^{1/2}}$$

If this gap is smaller than the boundary layer thickness the change of the tangential speed across the gap is linear, like in the well-known Couette flow.

Chapter 4

4 Numerical Solution of Flow

As pointed out in the previous sections, flow between inter-disk passages of Tesla disk turbine is not straight forward as compared to classical bladed turbines that operate on momentum exchange and pressure variation on work transferring surfaces. Different authors have approached this flow in a rather heterogeneous intellectual manner. In some case, investigators without any background to fluid mechanics have managed to provide their own solution to the fluid flow by tackling the problem in a mathematical line of attack. [32, 54, 57] In other cases, their straight forward engineering approach was hindered due to the lack of powerful computer resources for solving the essential governing equations. In this sense, implementing CFD techniques to describe the most sought design characteristics with current available computer capacity provides a relatively faster and more accurate result.

In the coming sections, numerical approach for solving the flow variables in a CFD environment for Tesla multiple-disk turbine will be dealt. The flow conditions in Tesla turbine are first specified in order to assign the appropriate physical flow model options available in FLUENT commercial CFD software. Geometrical model preparation alongside with the necessary model simplification will be stated. The underlining theory behind discretization methods of flow domain will be elaborated. Solution procedure from model construction to setting up of physical model to posting results will be progressively described. The presented discussions are adapted from FLUENT user guide with Tesla turbo machinery in context to elucidate the underlying program assumptions for the numerical analysis.

4.1 Flow conditions and governing equations

For all flows, FLUENT solves numerically the Conservation Equations for Mass, Momentum and additional Transport equations (if the flow is turbulent) for a fluid in a given flow geometry. The transport equations have different forms depending on the turbulence modeling used. Bases for the CFD analysis of the flow inside the Tesla turbine has been set as realizable k–ε turbulence model, moving reference frame and steady state incompressible flow; and hence, all the governing equations are based upon those physical flow models.

4.1.1 Continuity Equation (Mass conservation equation)

The general form of mass conservation, or continuity equation, can be written as follows:

$$\boldsymbol{\nabla}.\left(\vec{V}\right) = \mathbf{0} \tag{4.1}$$

Given that the absolute velocity of flow between each disk space falls below nozzle exit velocity, the flow domain remains in subsonic state considering the design row entry velocity. It is realistic to assume incompressible conditions for such flow that are kept under 0.3 Mach number.

For steady state incompressible flow with 2D geometries, the continuity equation is given by:

$$\frac{\partial}{\partial z}(v_z) + \frac{\partial(v_r)}{\partial r} + \frac{v_r}{r} + \frac{1}{r}\frac{\partial}{\partial \theta}(v_\theta) = \mathbf{0} \tag{4.2}$$

Where, z is the axial coordinate, θ is the tangential coordinate, r is the radial coordinate,v_z is the axial velocity, and$v_r$is the radial velocity. If the turbine would be modeled as an axisymmetric problem, the θ terms vanish leaving the radial and axial terms for solving.

4.1.2 Navier-Stokes equations (Momentum conservation equations)

In inertial frame of reference, momentum conservation equation for a controlled volume is given as:

$$\boldsymbol{\nabla}.(\rho\vec{v}\vec{v}) = -\boldsymbol{\nabla} p + \boldsymbol{\nabla}.(\bar{\bar{\tau}}) + \rho\vec{g} + \vec{F} \tag{4.3}$$

Where:

p = Hydrostatic pressure,

$\bar{\bar{\tau}}$= Stress tensor, and

$\rho\vec{g}$ and $\vec{F}$ = Gravitational body force and external body forces (e.g. magnetic field, electric field, or externally induced stirring force), respectively.

For inviscid flow, the stress tensor element of the equation can be neglected. Ironically for our case, since friction in the disk channel space seems to aid the overall energy transfer process, it is necessary to keep this term in the numerical model. Note that the steady convective terms in $\nabla.(\rho\vec{v}\vec{v})$are nonlinearcomplicating the mathematical analysis.

The stress tensor, $\bar{\bar{\tau}}$, in equation 4.3 is given as:

$$\bar{\bar{\tau}} = \mu\left[(\nabla\vec{v} + \nabla\vec{v}^{T}) - \frac{2}{3}\nabla.\vec{v}I\right]$$

Where, $\boldsymbol{\mu}$ is the Molecular Viscosity, I is the Unit Tensor, and the second term on the right hand side is the effect of Volume Dilation.

For 2D axisymmetric geometries, the axial and radial momentum conservation equations are given as:

$$\frac{1}{r}\frac{\partial}{\partial x}(r\rho v_x v_x) + \frac{1}{r}\frac{\partial}{\partial r}(r\rho v_x v_x) = -\frac{\partial p}{\partial x} + \frac{1}{r}\frac{\partial}{\partial x}\left[r\mu\left(2\frac{\partial v_x}{\partial x} - \frac{2}{3}(\nabla.\vec{v})\right)\right] + \frac{1}{r}\frac{\partial}{\partial r}\left[r\mu\left(\frac{\partial v_x}{\partial r} + \frac{\partial v_r}{\partial x}\right)\right] + F_x \qquad (4.4)$$

And,

$$\frac{1}{r}\frac{\partial}{\partial x}(r\rho v_x v_x) + \frac{1}{r}\frac{\partial}{\partial r}(r\rho v_r v_r) = -\frac{\partial p}{\partial r} + \frac{1}{r}\frac{\partial}{\partial x}\left[r\mu\left(\frac{\partial v_r}{\partial x} + \frac{\partial v_x}{\partial r}\right)\right] + \frac{1}{r}\frac{\partial}{\partial r}\left[r\mu\left(2\frac{\partial v_r}{\partial r} - \frac{2}{3}(\nabla.\vec{v})\right)\right] - 2\mu\frac{v_r}{r^2} + \frac{2}{3}\frac{\mu}{r}(\nabla.\vec{v}) + \rho\frac{{v_z}^2}{r} + F_r \qquad (4.5)$$

where:

$$\nabla.\vec{v} = \frac{\partial v_x}{\partial x} + \frac{\partial v_r}{\partial r} + \frac{v_r}{r}$$

Similarly, the tangential momentum equation for 2D swirling flows is written as

$$\frac{1}{r}\frac{\partial}{\partial x}(r\rho v_x v_z) + \frac{1}{r}\frac{\partial}{\partial r}(r\rho v_r v_z) = \frac{1}{r}\frac{\partial}{\partial x}\left[r\mu\frac{\partial v_z}{\partial x}\right] + \frac{1}{r^2}\frac{\partial}{\partial r}\left[r^3\mu\frac{\partial}{\partial r}\left(\frac{v_z}{r}\right) - \rho\frac{v_r v_z}{r}\right] \qquad (4.6)$$

where, x is the Axial Coordinate, r is the Radial Coordinate, v_x is the Axial Velocity, v_r is the Radial velocity, and $v_z$is the Swirl Velocity.

4.1.3 Energy Equation

As it was previously stated at the beginning of the designing process, the flow was considered incompressible with isothermal temperature distribution over the totality of the domain. Examining the energy equations, the species diffusion flux, the conductivity and chemical reaction terms cancel out leaving the viscous dissipation terms only. Since we have three continuity equations for every direction and three momentum conservation momentum equations, adding another three energy equations with no particular interest in solving the flow temperature field will lead to over definition of the problem. The transferred shear forces can be calculated by solving viscous stress terms acting on the different control surfaces in every direction from the momentum equations. Hence, the energy equation needs not to be activated.

4.2 Frame of Reference

FLUENT normally solves the governing continuity and transport equations in a fixed (inertial) frame of reference. The reference coordinate is fixed in space and the relative motion of fluid particles will be calculated in relation to this stationary frame. On the contrary some problems, especially those with a moving parts (moving wall boundary conditions), wouldn't yield steady results on their domain. In such a case, it is wise to threat the problem with a non-inertial (moving) frame of reference in which case, the relative motion of particles on each moving part could be independently referenced from suitable coordinate point that seems to an observer on the moving part. [46]

Consequently, FLUENT adapts the transport relations to include relative velocity terms accommodate the moving frame.

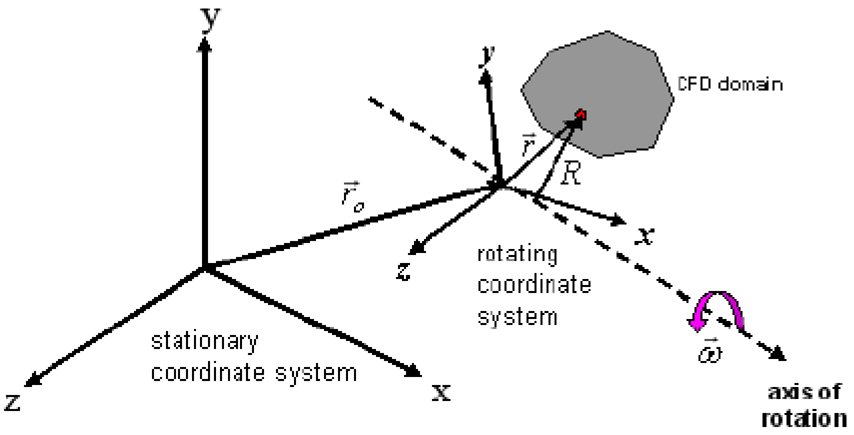

Figure 4-1: Fixed and Non-inertial reference frames [46]

Delving to Tesla turbine's constructional features, since the rotors, the spacers, and the casing are found on the same concentric circles' center, the flow could be modeled by a single (non-inertial) rotating reference frame (SRRF). By default, FLUENT permits the activation of a moving reference frame with a steady rotational speed. In doing so, the CFD problem that is unsteady in inertial frame of reference is rendered steady with respect to a moving frame. In the current case, the entire fluid domain is referred to single moving reference frame. Most analytical problems studied by previous investigators oversee this critical factor by considering the entirety of the fluid domain to a single inertial reference frame.

4.3 Turbulent Modeling

The choice of turbulence model depends on considerations such as the physics encompassed in the flow, the established practice for a specific class of problem, the level of accuracy required, the available computational resources, and the amount of time available for the simulation. Among the various turbulence model options available in FLUENT, the realizable k-ε turbulence model is found most appropriate for the CFD analysis of flow inside Tesla turbine.

With regard to Tesla turbine's case, the realizable k-ε, amongst the other k-ε models, is most likely to provide superior performance for flows involving rotation, boundary layers under strong adverse pressure gradients, separation, and recirculation.[47] The method also predicts the spread rate of planar and round jets with accuracy.

A detailed formulation of this model has been presented in Appendix A at the end of the report.

4.4 Numerics

Numerical solution involves discretization of the governing equations in time and space (along a grid). FLUENT solves the governing integral equations for the conservation of mass and momentum, and scalars such as turbulence. It uses a control volume-based technique that consists of: [46]

- Division of the domain into discrete control volumes using a computational grid
- Integration of the governing equations on the individual control volumes to construct Algebraic equations for the discrete dependent variables ("unknowns") such as velocities, pressure, temperature, and conserved scalars.
- Linearization of the discretized equations and solution of the resultant linear equation system to yield updated values of the dependent variables.

FLUENT allows two methods of numerical formulation:

- Pressure-based and
- Density-based solvers.

The two numerical methods employ a similar discretization process (finite volume), but the approach used to linearize and solve the discretized equations is different. The segregated solver formulation is more appropriate for incompressible flows; hence, it has been used for the CFD analysis of flow through the disk spaces and is discussed in the coming sections.

Their basic distinction originates from the way the governing momentum and scalar equations are linearized to form discretized algebraic equations before being solved.

4.4.1 Segregated Solution Method

In the segregated solver, the governing equations are solved sequentially (i.e., segregated from one another). Because the governing equations are non-linear (and coupled), several iterations of the solution loop must be performed before a converged solution is obtained. [46]

These successive steps are summarized in the flow chart given in Figure 4-2.

In general, the segregated solving method includes the following iterative steps before it renders credible solution:

1. Fluid properties are updated, based on the current solution. (If the calculation has just begun, the fluid properties will be updated based on the initialized solution.)
2. The *u*, *v*, and *w* momentum equations are each solved in turn using current values for pressure and face mass fluxes, in order to update the velocity field.
3. Since the velocities obtained in Step 2 may not satisfy the continuity equation locally, a ``Poisson-type" equation for the pressure correction is derived from the continuity equation and the linearized momentum equations. This pressure correction equation is then solved to obtain the necessary corrections to the pressure and velocity fields and the face mass fluxes such that continuity is satisfied.
4. Equations for scalars such as turbulence are solved using the previously updated values of the other variables.
5. Check for convergence of the equation set is made.

These steps are continued until the convergence criteria are met. The above solving procedures are suited to pressure based segregated solving method where the flow under consideration is presumed to be incompressible.

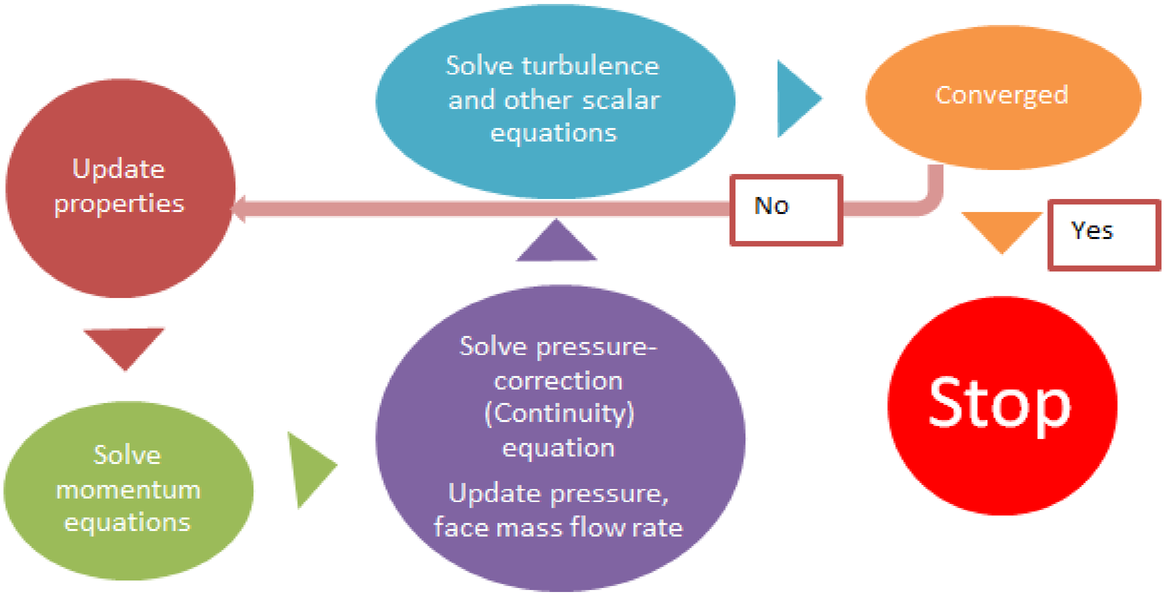

Figure 4-2: Overview of Segregated Solution Method

In pressure based solving method, the constraint of mass conservation (continuity) of the velocity field is achieved by solving a pressure (or pressure correction) equation. The pressure equation is derived from the continuity and the momentum equations in such a way that the velocity field, corrected by the pressure, satisfies the continuity. Since the governing equations are nonlinear and coupled to one another, the solution process involves iterations wherein the entire set of governing equations is solved repeatedly until the solution converges.

4.4.2 Spatial Discretization scheme: Second order upwind [scalar transport equation]

FLUENT uses cell center values to determine convective terms in the cell face boundaries. Determining face scalar values is done through interpolation of scalar terms between two neighboring cell centers. Fluent uses different interpolation schemes depending on whether the employed solving method is density-based or pressure-based. It also depends on the availability of model that is enough to simulate the particular mode within the selected scheme. These discretization schemes are first-order upwind, second-order upwind, power-law, central differencing, bounded central differencing and QUICK.

The second-order scheme is normally used for viscous terms and considering the viscous nature of the flow in the disk spacing it is amenable to apply this scheme in the solution process. The second-order upwind scheme is advantageous over first-order scheme in that by the application of a multidimensional linear reconstruction approach, it offers more accurate approach at the expense of solution time. It also has an added benefit of being able to utilize quadrilateral/hexahedral grid elements in addition to triangular/tetrahedral elements that can be solved with better accuracy.

When second-order upwind is selected, the face value ϕ_f is computed using the following expression:

$$\boldsymbol{\phi_{2nd} = \phi + \nabla\phi.\vec{r}} \tag{4.7}$$

Where ϕ is the Cell-Centered Scalar Quantity value and $\nabla\phi$ is its Gradient in the upstream cell, and $\vec{r}$ is the displacement vector from the upstream cell centroid to the face centroid. The second order upwind scheme is available to both the pressure-based and density based solving schemes.

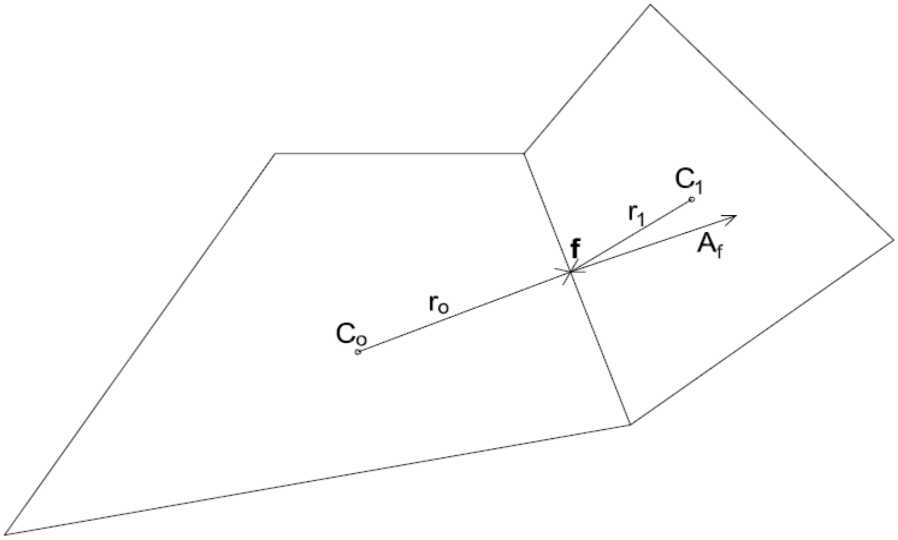

Figure 4-3: Control Volume Used to illustrate Discretization of a Scalar Quantity [46]

Apart from the two mentioned schemes, the QUICK and third-order MUSCL discretization schemes may provide better accuracy than the second-order scheme for rotating or swirling flow. The QUICK scheme is applicable to quadrilateral or hexahedral meshes, while the MUSCL scheme is used on all types of meshes. In general, however, the second-order scheme is sufficient and the QUICK scheme will not provide significant improvements in accuracy.

4.5 Discretization of governing equations

4.5.1 Momentum Equation

As it was done for the scalar transport equation, the momentum equation is discretized in the following way, [46]

$$\boldsymbol{a_p u = \sum_{nb} a_{nb} u_{nb} + \sum p_f A_i + S} \quad (4.8)$$

where:

p_f=Face Pressure Value between Two Neighboring Cells

S=Source Term

A_i= ith Face of the Control Volume

a_p= Linearized coefficient for scalar quantity,u

a_{nb}= Neighboring Linearized Coefficient for scalar quantity,u_{nb}

The pressure values at the faces using are interpolated using momentum equation coefficients.

$$P_f = \frac{\frac{P_{co}}{a_{p,co}} + \frac{P_{c1}}{a_{p,c1}}}{\frac{1}{a_{p,co}} + \frac{1}{a_{p,c1}}}$$

The above equation provides acceptable pressure values as long as the pressure gradient between neighboring cells is smaller. Such pressure interpolation method may not be suitable for high Rayleigh-number natural convection or highly swirling flows or else where there is pressure gradient at the wall due to presence of body forces.

In such cases, the location in the domain where there is a spike in pressure distribution must be refined so that smoother transition can be achieved.

As an alternative to the above linear coefficient weighted interpolation method, the PRESTO!(PREssure STaggering Option) scheme will be used here under because of its applicability of the algorithm for high swirling flows. The PRESTO! scheme uses the discrete continuity balance for a “staggered" control volume about the face to compute the “staggered" (i.e., face) pressure. Note that for triangular, tetrahedral, hybrid, and polyhedral meshes, comparable accuracy is obtained using a similar algorithm.

4.5.2 Continuity equation

The steady state continuity equation in integral form is given as:

$$\boldsymbol{\oint \rho \vec{v} d\vec{A} = 0} \quad (4.9)$$

The discretized form of the above integral equation is

$$\boldsymbol{\sum_f^{N_{faces}} J_f A_f = 0} \quad (4.10)$$

Where, J_f is the Mass Flux through face f and A_f is Cross Sectional Face Area

The face value of velocity is not averaged linearly; instead, momentum-weighted averaging, using weighting factors based on the a_p coefficient on the previous equation is performed.

$$J_f = \rho_f . \frac{a_{p,co} v_{n,co} + a_{p,c1} v_{n,c1}}{a_{p,co} + a_{p,c1}} + d_f\left((p_{co} + (\nabla p)_{co} . \overrightarrow{r_o}) - (p_{c1} + (\nabla p)_{c1} . \overrightarrow{r_1}) \right) = \hat{J}_f + d_f (p_{co} - p_{c1}) \tag{4.11}$$

Where, $p_{co}, p_{c1}$and $v_{n,co}$,$v_{n,c1}$ are the Pressures and Normal Velocities within the two cells on either side of the face, respectively. $\hat{J}_f$ contains the influence of velocities in these cells. The termd_f is a function of $\overline{a}_p$, the average of the momentum equation a_p coefficients for the cells on either side of the face f.

4.6 Pressure-Velocity coupling

As discussed before, the face values of velocity and pressure are determined based on non-linear momentum-weighted averaging of the pressure and velocity terms at the cell centers derived from continuity relation. Iteration of these unknown terms commences once a guessed face mass flow rate is assumed based on predicted pressure field. But predictive values of pressure and mass variables certainly do not satisfy conservation of mass principle and hence has to be rectified by introducing certain corrective added variable. The pressure-velocity coupling as such is this predictor-corrector approach that helps to satisfy the discrete continuity equation with almost zero variation on the face mass terms across the flow field.

Many problems will benefit from using SIMPLEC, particularly because of the increased under relaxation that can be applied. SIMPLE and SIMPLEC use about the same pressure-velocity coupling algorithm only to differ in the pressure gradient correcting coefficient in the SIMPLEC which gives it accelerated convergence edge over the SIMPLE approach. Hence, for the current modeling process the SIMPLEC algorithm will be used for pressure and mass flow rate correction.

The step to be followed during solving process is illustrated in the flow chart below.

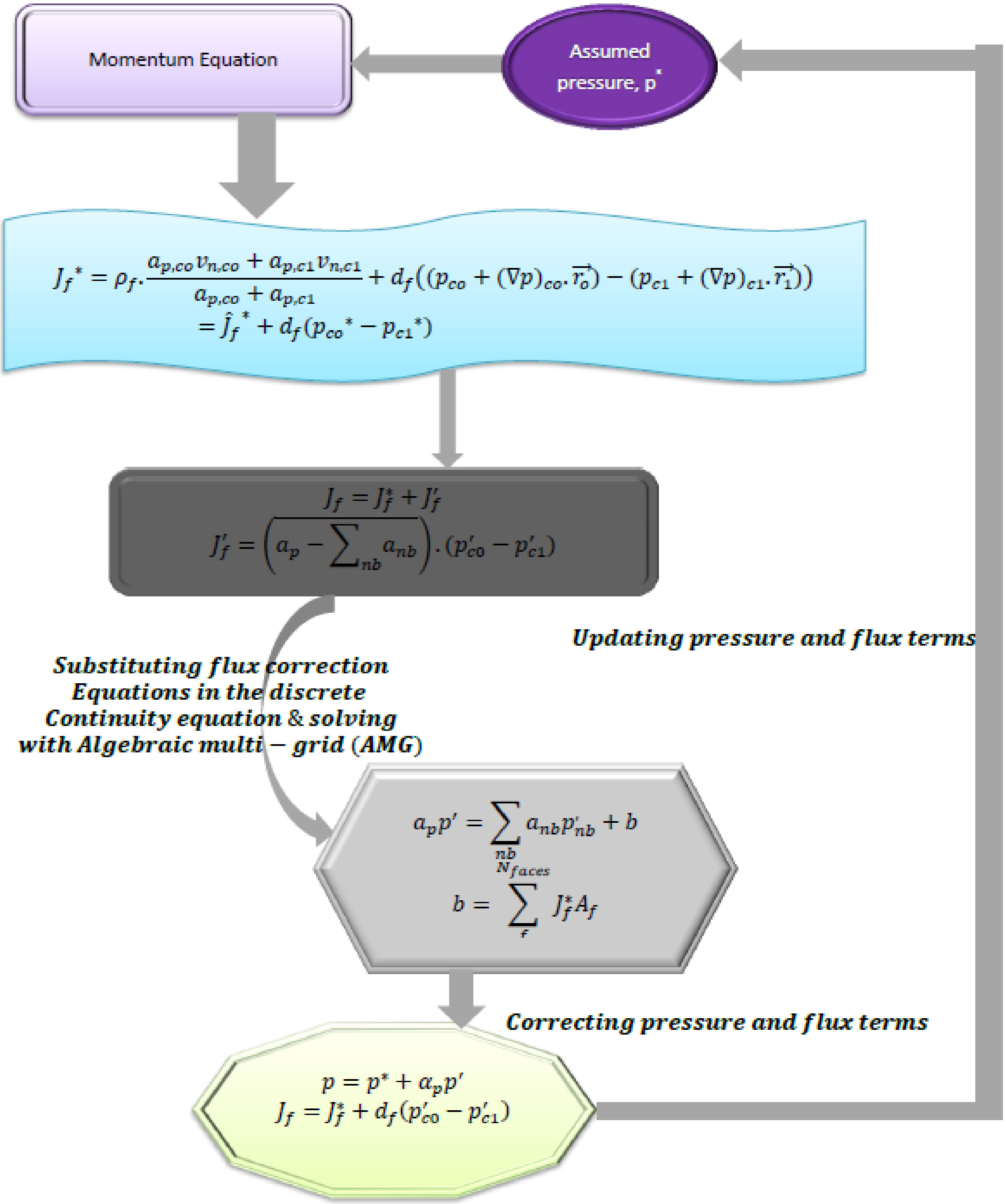

Figure 4-4: Algorithm for SIMPLEC Method (Adapted from [46])

where, variables with '*' are predicted variables, corrective terms are given in terms of single quotation mark.

4.7 Under Relaxation Factor

Because of the nonlinearity of the equation set being solved, it is necessary to control the change of a momentum or pressure, ϕ, during iteration. This is typically achieved by under-relaxation, which reduces the change of ϕ produced during each iteration step. It is the main technique by which the solver is stabilized. In a simple form, the new value of the variable ϕ within a cell depends upon the old value, ϕ_{old}, the computed change in ϕ, $\Delta\ \phi$, and the under-relaxation factor,α, as follows:

$$\boldsymbol{\phi = \phi\_old + \alpha\Delta\phi} \qquad (4.12)$$

where:

ϕ = Scalar quantity,

$\phi_{old} = \phi$value taken at one step earlier iteration,

$\boldsymbol{\alpha}$ =Under relaxation factor

Similarly, the under-relaxation of equations is used in the pressure-based solver to stabilize the convergence behavior of the outer nonlinear iterations by introducing selective number of ϕ in the system of discretized equations.

$$\boldsymbol{\frac{a_P\phi}{\alpha} = \sum_{nb} a_{nb}\phi_{nb} + b + \frac{1-\alpha}{\alpha} a_p\phi_{old}} \qquad (4.13)$$

Where, a_{nb} and a_p are Linearized Coefficients for ϕ_{nb} andϕ, respectively. $b$is a Constant

The under relaxation factor assumes values between 0 and 1. Generally, increasing under relaxation factor to values nearer to unity leads to speedier solution time, while depending on the case, leads to perturbations in the iterative solution. Conversely, reducing the under relaxation factors of quantities such as momentum, pressure, density, and body forces will result in reduced diffusion of solution term while consuming lengthier solving time.

The general procedure in solving control volume problems is first to start the iterations with relatively higher under relaxation factor and then by monitoring the solution residuals whether or not they are converging to their minimum set points, proceeding to lower under relaxation factors. In some cases where high grid skewness is at hand, the problem must be solved by manipulating adding skewness correction factor in addition to the under relaxation factor.

4.8 Near-Wall Treatment

The near-wall modeling significantly impacts the fidelity of numerical solutions, in as much as walls are the main source of mean vorticity and turbulence. After all, it is in the near-wall region that the solution variables have large gradients, and the momentum and other scalar transports occur most vigorously.

Traditionally, there are two approaches to modeling the near-wall region. In one approach, the viscosity affected inner region (viscous sub layer and buffer layer) is not resolved. Instead, semi-empirical formulas called "wall functions" are used to bridge the viscosity-affected region between the wall and the fully-turbulent region. The use of wall functions obviates the need to modify the turbulence models to account for the presence of the wall.

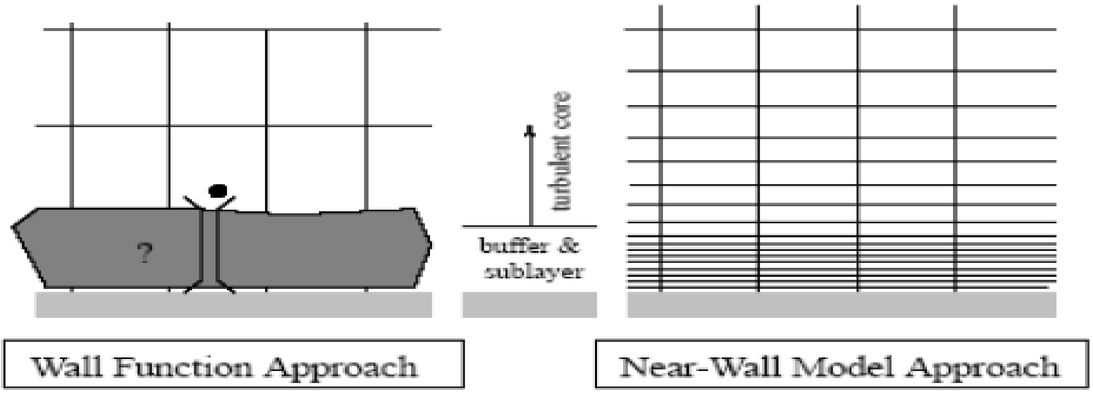

- **The viscosity-affected region is not resolved, instead is bridged by the wall functions.**
- **High Re turbulence models can be used**

- **The near-wall region is resolved all the way down to the wall**
- **The turbulence models ought to be valid throughout the near-wall region.**

Figure 4-5: Near-Wall Treatments [46]

In another approach, the turbulence models are modified to enable the viscosity-affected region to be resolved with a mesh all the way to the wall, including the viscous sub layer. This will be termed the "near-wall modeling" approach.

In most high-Reynolds-number flows, the wall function approach substantially saves computational resources, because the viscosity-affected near-wall region, in which the solution variables change most rapidly, does not need to be resolved. The wall function approach is popular because it is economical, robust, and reasonably accurate. It is a practical option for the near-wall treatments for industrial flow simulations.

The wall function approach, however, is inadequate in situations where the low-Reynolds number effects are pervasive in the flow domain in question, and the hypotheses underlying the wall functions cease to be valid. Such situations require near-wall models that are valid in the viscosity-affected region and accordingly integrable all the way to the wall.

Considering the constructed geometrical models at hand, since the working flow regime space is smaller and the available number of equations are fewer in the two-dimensional geometrical model than the three dimensional turbine model, “near-wall modeling” approach is followed for generating mesh around the rotating disk walls. This will give the modeler a greater freedom in expediting the solution process by using the limited computer capabilities determined from such simplifications. On the other hand, the 3D model, as it requires higher solution capabilities, gives a little less freedom for treating the flow near the disk surfaces. In this case, “wall-function” approach is a more viable option to treat near-wall viscous property variations.

Among the four types of wall-functions available in FLUENT enhanced wall treatment is chosen for the purpose. Enhanced wall treatment is a near-wall modeling method that combines a two-layer model with enhanced wall functions. To achieve the goal of having a near-wall modeling approach that will possess the accuracy of the standard two-layer approach for fine near-wall meshes and that, at the same time, will not significantly reduce accuracy for wall-function meshes, FLUENT can combine the two-layer model with enhanced wall functions.

Chapter 5

5 Simulating the Tesla Turbine

5.1 Introduction

In an effort to approximately depict the actual flow in the different sections of the Tesla turbine, commercial CFD packages come in handy by providing virtual platform for simulation under which the governing physical equations are solved. Although user friendliness varies across the different state-of-the-art commercial CFD tools, basic solving approaches remain far or less the same. These software tools comprise some form of geometrical modeling applications in connection with numerical solving applications with inbuilt physical models which are initialized using user supplied boundary conditions. The geometrical modeling platform can be found conjoined with the numerical solving program, as in ANSYS, or else as separate programs communicating through common file formats, as in between Gambit and FLUENT.

Under the current thesis project, the latter two software packages will be deployed to the task to construct and generate mesh of the turbine geometrical model, and subsequently solve the flow. The totality of computation activities performed throughout the simulation process is summarized in the following flow chart below.

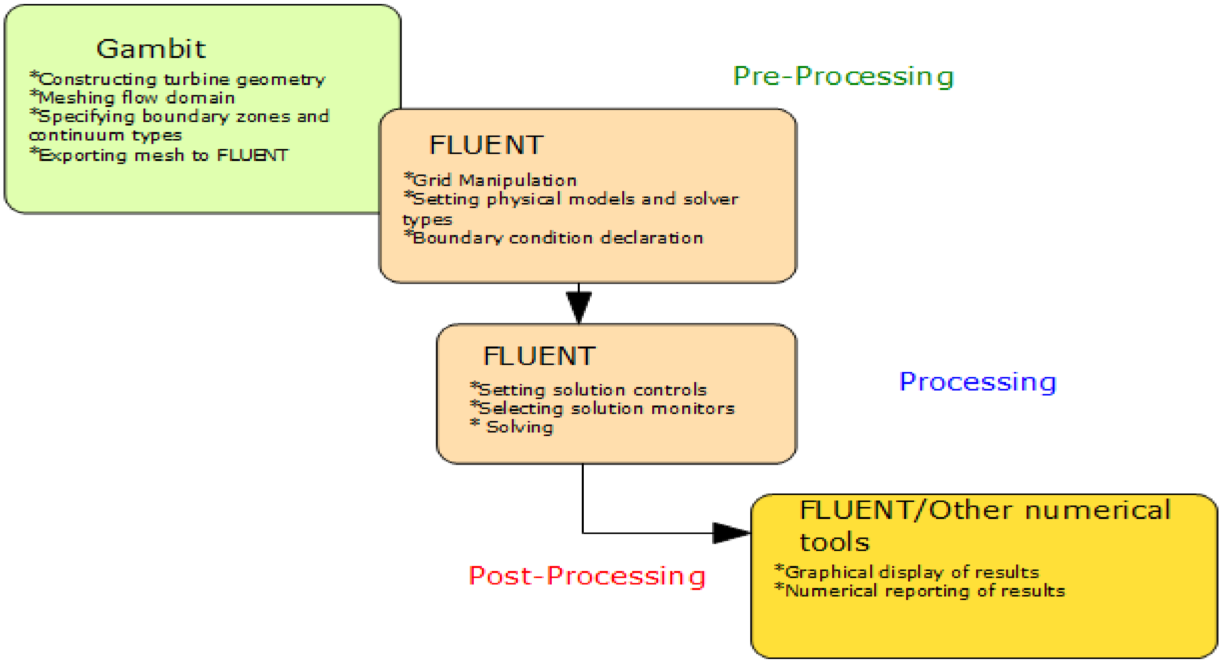

Figure 5-1: Process description of numerical solving process between Gambit and FLUENT

Details of the activities involved in each of the phases are described in the coming sections.

5.2 Basic Steps for CFD Analysis

The preprocessing procedures of the CFD simulation are dealt under the two consecutive broad sections: pre-processing in GAMBIT and pre-processing in FLUENT.

5.2.1 Preprocessing of Simulation

Preprocessing in GAMBIT includes building of turbine geometry, mesh generation, specifying boundary zones and also exporting the mesh file to be read in FLUENT.

5.2.1.1 Preprocessing in GAMBIT

a. Building Geometry

Two geometrical models are constructed both of which base themselves on the physical model simplification followed of the flow. The first of the two assumes that there is no tangential disparity of flow variables across the inter-disk space, which then lends itself to a two dimensional (2D) condensation of the flow regime. A further simplification to this would be circumferential flow introduction to the disk row without finite number of fluid injection nozzles along the periphery. This assumption makes it easy to deal with the problem set as an axisymmetric, 2D flow across disk bank.

A more resourceful but rather time and disk memory consuming model which treats flow in 3D is demonstrated. The geometrical model, as opposed to the former, assumes variations in the number of air introducing nozzles on the periphery of the disk row periodically located circumferentially. Here too, geometrical symmetry allows modeling simplifications need to be taken in considering only the flow domain at half of the axial span from the central exit port. In turn, this would reduce the computational time to be reduced by half taking into account the double dynamic memory requirement in meshing the flow.

The same calculated turbine design dimensions are used to develop the virtual models. It must be noted that the dimension of the model object is specified in a default unit rather than international SI or empirical unit. As shall be seen later, unit declaration is part of the pre-processing procedure within the FLUENT software.

b. Meshing the flow domain

In the current Tesla turbine case, since the flow undergoes through a regular shaped trapezoidal fluid injection nozzles thereafter to join a cylindrical flow channels (inter-disk spaces), it is realizable to use quadrilateral/hexahedral elements that are suitable for flows parallel to the boundary faces as opposed to tet/tri elements. In light of the boundary layer buildup from the leading edge of the disks up to the central exit port, bi-directional graded mesh on either side of the disks was prepared. The first span of the graded mesh has a length 0.15 mm which stretches by a factor of 1.1 for the successive mesh spans in the axial direction. Complete mesh geometry of the proposed models is presented in figure 5-2 with an up-close look at the inter-disk spacing space and nozzle ejection interface.

In summary, 57,610 quadrilateral elements were used in the axisymmetric 2d model while up to 2,654,690 hexahedral cells were prepared for the three dimensional center plane symmetrical models. Careful precaution was taken to ensure the conformity and consistency of geometry (vertices, edges, and faces) between the adjacent fluid regions.

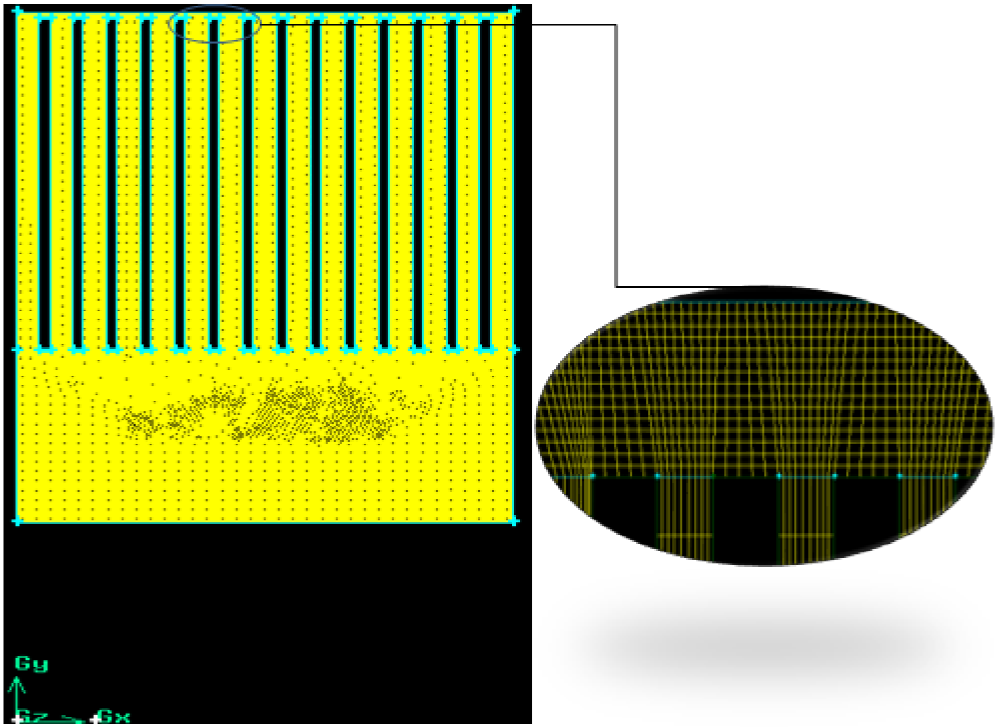

Figure 5-2: Mesh geometry of Tesla turbine

At the end of the meshing course of activity, the meshed geometry was subjected to mesh quality examinations as Gambit provides skewness rating scales according to angular or size deviation from comparative equilateral or angular elements.

c. Specifying boundary zones and continuum types

Boundary type specifications define the physical and operational characteristics of the model at those topological entities that represent model boundaries. Boundary zones generally set limiting flow conditions on certain geometrical interfaces where the condition of flow is known prior to running numerical solution process without having to constrain in numerical terms. Boundary zone also establishes certain essential model features such as the assignment of rotor rotating axis and symmetrical plane/axis about which model reduction was made.

Accordingly, velocity inlet boundary zone is set for the nozzle inlet edge/face of the turbine as it is appropriate for defining the velocity and scalar properties of flow at the fluid boundary condition. On the other hand, pressure outlet boundary zone is assigned for the disk bank exit as it is the case for the expanded air to leave at atmospheric condition. Similarly, the spacer-disk assembly rotation axis was taken as the line of 'symmetry' for the axisymmetric 2D model. Simultaneously rotating surfaces like disks and spacer surfaces are also grouped to be specified with 'wall' boundary types. Pictorial representation of the various boundary zones is given in Figure 5-3.

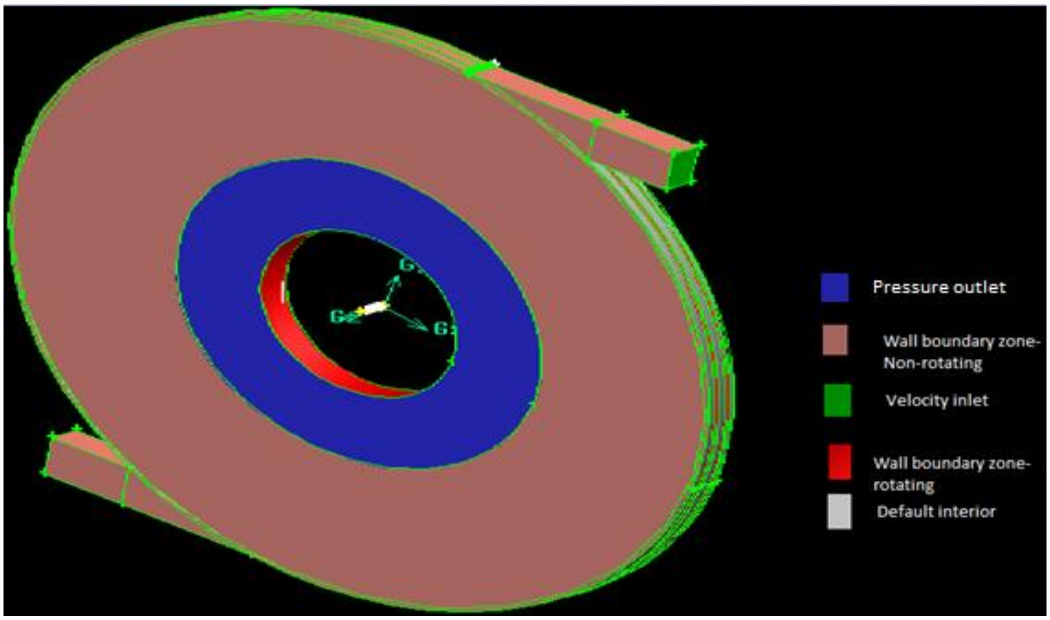

Figure 5-3: Boundary Zones

On the other end, flow continuum specifications define the physical characteristics of a model within regions of the flow field. In most turbo machinery problems, only the fluid region is prepared for numerical computation and the solid region is defined by presence of walls.

d. Exporting mesh file to FLUENT

After specifying the boundary zones and the continuum types, the mesh and geometry developed in GAMBIT is saved in a database file *.dbs for future reference. This model is exported to a mesh file *.msh so that FLUENT can read the grid information and use it for further preprocessing and computation analysis.

5.2.1.2 Preprocessing in FLUENT

The overall goal of preprocessing the problem set is to specify the required input parameters and numerical discretization schemes with enough information to set off the solving process. This routine starts by importing the *.msh extension file into FLUENT then proceeds to manipulating the imported grid according to the resolution of solution variables using its inbuilt tools. The process goes forth until all the physical models, the known boundary conditions and numerical solving schemes have been totally defined. For the current discussion, this procedure is discussed in two main broad subroutines: Grid manipulation and Defining analysis basis (Setting up solver and physical models).

a. Grid manipulation

Grid manipulation is concerned with refining, rearranging, and conforming mesh topology so as to avoid steep gradients on solution terms in neighboring cells. The process consists of the following subroutines.

i. Checking grid

The grid checking capability in FLUENT provides domain extents, volume statistics, grid topology and periodic boundary information, verification of simplex counters, and for axisymmetric cases, node position verification with respect to the x axis.

Negative volume features needs to be adapted before the solution could proceed. In axisymmetric problems, such as the Tesla turbine’s case, negative volumes arise from turbine geometry being located below the x-axis within the global reference frame. In axisymmetric case, the program considers the rotation of the rotor-spacer assembly to take place about the x-axis.

The number of faces and nodes on the different topological elements is checked. After running topological check, FLUENT goes for the face handedness. If correct connectivity is achieved, all the cells will be remarked with right handed verification. Else, left handed, usually resulting from negative faces.

At the end of the meshing course of activity, the meshed geometry was subjected to mesh quality examinations as Gambit provides skewness rating scales according to angular or size deviation from comparative equilateral or angular elements. In all the cases, the meshed geometries satisfied the recommended 0.85 skewness factor set limit for tetrahedral and hexahedral elements that would in turn ensures minimized perturbations and more accurate results in the solution variables.

ii. Scaling grid

As mentioned in earlier, the generated grid file on GAMBIT is scaled in terms of unit less (default) virtual scale. After importing the mesh file, FLUENT by default assigns meter to be the grid dimensions while setting up a case file. Since the entire model dimensions are specified in terms of mms, all the grid dimensions, in the current model, will be multiplied by the corresponding scale factor.

iii. Adapting grid geometry

Smoothing and face swapping are tools that complement grid adaption, increasing the quality of the final numerical mesh by modifying the cell connectivity through repositioning of interior nodes. In all of these cases, the intention of adapting mesh geometry is to reduce the variable fluctuation within acceptable limit by controlling the grid skewness factor. Highly skewed lead to larger truncation error with subsequent reduction of accuracy of the required solution terms.

With regard to this, the nozzle exit to rotor inlet recess area/volume are adopted to include finer mesh elements to examine the effect of flow losses indicated earlier in section 2.9. Furthermore, coarse mesh in the disk row discharge area is made smoother following the same procedure.

iv. Display grid

Grids have been visually inspected to check for grid problems and corrective actions were taken where necessary. Grids are also displayed to incorporate surfaces, the outline of all or part the domain, the grid lines (edges), the nodes on the domain surfaces and/or the solid surfaces (filled grids) when examining the solution.

b. Setting up the Solver and Physical Models

This part of the modeling process mostly relates to selecting suitable solver, deciding physical models that fit the particular flow, declaring working fluid properties, specifying the known boundary conditions and solution parameters.

i. Setting solution models

The flow models are set for the simulation process to determine the governing equations of the CFD analysis discussed earlier in Chapter 4. The following general settings of the software and assumptions are considered into the CFD model:

Table 5-1: Solver Model Assumptions

Model Assumptions	Settings
Numeric	Double precision
Space	Axisymmetric 2D and 3D
Time	Steady state
Solver	Pressure-based segregated scheme
Density	Incompressible
Reference frame	Absolute
Gravitational effect	None

ii. Defining materials

The turbine propellant working material is pure compressed air. FLUENT provides multitude of options for determining the variations of the key physical material properties based on different gas property assumptions (laws). Similarly, materials for casing, rotor disks, and spacers are also specified for the 'Solid' continuum type specified in GAMBIT. A summery table indicating the totality of assumptions taken is presented below.

Table 5-2: Thermo-Physical Properties of Selected Materials for Construction and Operation of Tesla Turbine

Turbine Part	**Material**	**Thermo-physical properties**			
		ρ ***[kg/m3]***	***C_p*** ***[J/kg-K]***	***k*** ***[w/m-K]***	**μ** ***[kg/m-s]***
Casing	Mild steel	8030	502.48	16.27	-
Disks					
Spacers					
Working fluid	Air	1.4963	1006.43	0.0242	$1.851\mathrm{x}10^{-5}$

Note that no distinction, on the turbine material, has been made between the different parts as limitation set by FLUENT material library. Observation of the nature of problem type leads to understanding that Solid material selection wouldn't have any significance on the solution as the current case is not in any way near a thermal problem.

iii. Boundary conditions

Boundary conditions are set of known initial solutions for boundary zones defined in Gambit on selected boundary edges or surfaces. These initial solution terms may be given in terms of numerical values or rather in assignment of a given boundary type for which certain material property is attributed.

Rotational boundary condition is set for the rotor and spacer assembly on the 'wall' boundary zone in absolute frame of reference. Stationary wall condition is assigned for the casing and nozzle walls. Fluid entrance velocity is given by its x and y components in order to specify the fluid entry angle.

Table 5-3: Summary of Turbine Boundary Conditions

Boundary	Boundary zone	Boundary condition
Fluid Inlet	Velocity inlet	Velocity Magnitude=211.94 m/s (relative to adjacent cells) Nozzle entry angle(α)= 9 ^{o} from tangent of the casing
Fluid exit	Pressure outlet	Gauge pressure=0 pa
Casing	wall	-Stationary wall -no-slip condition
Disk and Spacer	wall	-Rotationally moving wall -Angular velocity(ω) =1046.67 rad/s
Fluid region	default interior	Interior
Disk row symmetry wall	Symmetry	-

5.2.2 Processing in FLUENT

The following part of the simulation process much deals with setting conditions for convergence, providing initial solutions and monitoring the solution control terms as the iterations progress forward.

a. Setting solution controls

Simulation processing in FLUENT involves setting of solution controls such as under relaxation factors and selecting suitable numerical discretization schemes for spatial and fluid field variable terms. Based on the type of relevant equation for defining a given flow, under relaxation factors for pressure, momentum, body forces, and in case of compressible flows, density, are introduced for updating these terms in successive iteration steps. Up on monitoring the progression of residual terms, the under relaxation factors can be lowered or incremented as instabilities occur along-the-way and convergence is not achieved. In any case, the simulation must proceed in such a way that must avoid perturbations especially, in the momentum equation, as input parameters such as disk rotation speed and fluid flow rate could destabilize the solution if they are not gradually increased in successive iteration steps.

Table 5-4: Solution Control Discretization Schemes and Under-Relaxation Factors

Discretization Scheme	
Variable	**Scheme**
Pressure	PRESTO! Pressure Staggering Option
Pressure-Velocity coupling	SIMPLEC (Semi-Implicit method for pressure-linked option Consistent)
Momentum	QUICK
Turbulence model	realizable k-ε
Swirl velocity	Second Order Upwind
Near wall treatment	Enhanced wall functions
Under-Relaxation factors	
Equation	***Value***
Pressure	0.3
Body forces	1
Momentum	0.65
Density	1
Turbulence kinetic energy	0.8
Turbulence dissipation rate	0.8

On the other hand, the SIMPLEC pressure-velocity coupling is used here over its counterpart SIMPLE scheme, for the fact that, the former has better convergence merit and wider span for application of under-relaxation factors because of its inherent pressure gradient correction algorithm. For high swirling and high speed rotating flows, as for the case in Tesla turbine, PRESTO! Pressure interpolation scheme should be used as FLUENT user guide recommends it. Taking into account the quad/hex grid generated for the turbine geometry, it is wise to apply second order upwind or QUICK scheme for attaining accurate result. The QUICK scheme, as compared to second order upwind scheme, tends to be more accurate for swirling or rotating flows, but only works for the aforementioned grids neglecting the rest of grid topologies. In the case that the solution doesn't converge, it is advisable to start first with first order upwind scheme and subsequently shifting to QUICK scheme.

b. Selecting solution monitors

Solution convergence can be checked either by monitoring graphical progression of residuals, force vectors, surface/volume integrals or through numerical reporting of overall balance of these results. In any case, convergence criteria expressing by how much the numerical solution variable (conserved variable) disparity between successive iteration terms must be specified by the user.

i. Monitoring residuals

One way of checking solution convergence is by monitoring solution residuals for continuity, x, y and z velocities, and swirl. In general, you will only need to enable residual plotting and modify the convergence criteria by monitoring iteration history. The following residuals are applied as one means for checking convergence.

Table 5-5: Residual Limit Set for Continuity, Momentum and Turbulence Equations

Equation	Residual
Continuity	$1x10^{-4}$
x-velocity	$1x10^{-3}$
y-velocity	$1x10^{-3}$
z-velocity	$1x10^{-3}$
Swirl	$1x10^{-4}$
k and ε	$1x10^{-3}$

A historical plot of the above residuals is given in Figure 5-4.

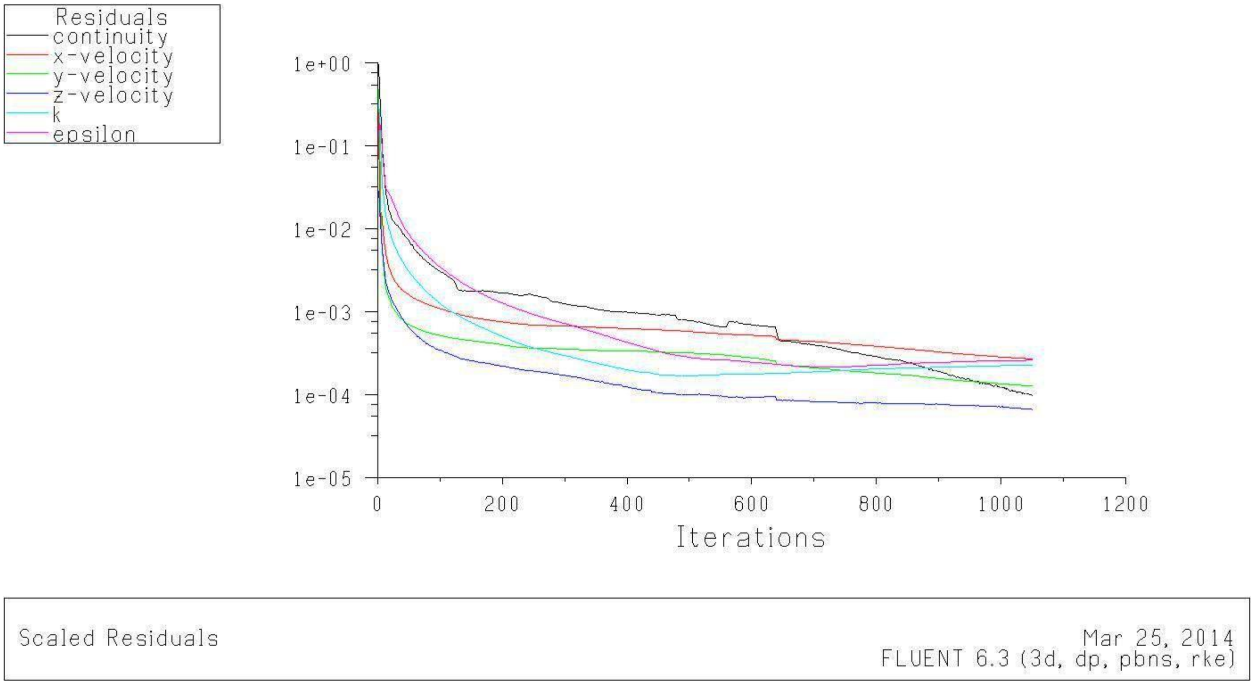

Figure 5-4: Historical Residual Plot

Since the fluid domain comprises not only the cylindrical inter disk flow spaces but also the fluid supply nozzles, monitoring momentum field variables is carried out using global x, y, z rectangular coordinates.

ii. Surface Monitoring

Sometimes, meeting residual solution convergence criteria does not necessarily guarantee accurate results. Other times, the different residual criteria set for convergence remain higher than the actual precision level achieved over much of the iteration spectrum, hence convergence remain unattained. Such modeling inconsistency arise from various reasons such as guessing the initial flow field much closer to the actual field resulting in large scaled residual for the continuity equation or poor estimation for turbulence residuals not showing continually decreasing pattern in the monitor screen.

It is, therefore, a good idea to judge convergence not only by examining residual levels, but also by monitoring relevant integrated quantities. At the end of each solver iteration or time step, the average, mass average, integral, flow rate, or other integral report of a field variable or function can be monitored on a surface.

Monitoring surface integrals can be used to check for both iteration convergence and grid independence. For example, the average value of a certain variable on a surface can be monitored and solution is said to have converged when this value no longer changes in successive iterations. The grid can then be adapted and the solution be reconverged. The solution can be considered grid-independent when the average value on the surface stops changing between adaptions.

A mass weighted average velocity magnitude plot for the whole iteration range has been given in figure 5-5 as presented below.

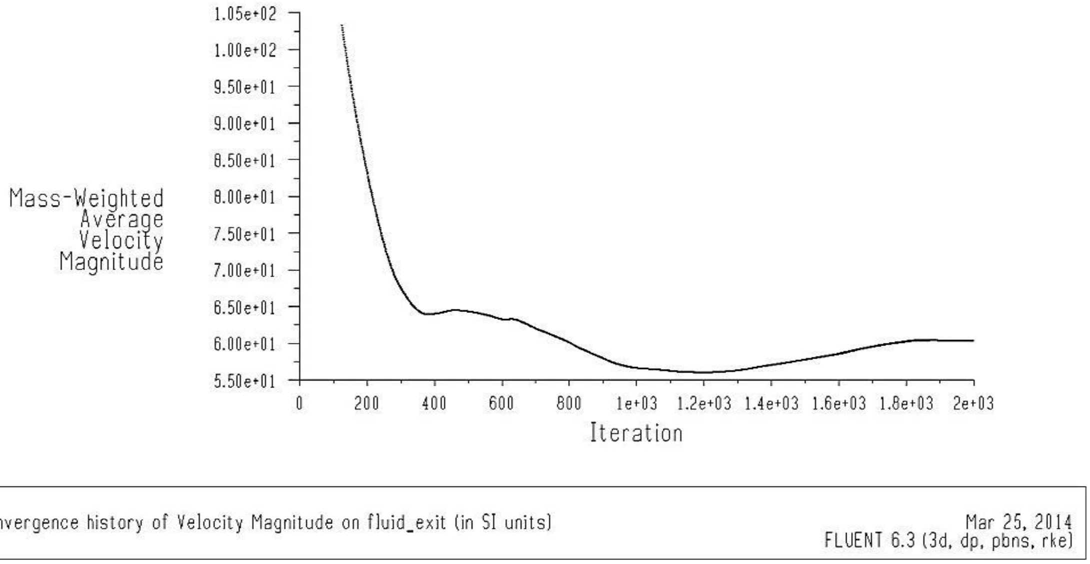

Figure 5-5: Controlling the Convergence of Velocity Magnitude at the Fluid Exit

The graph shows the average mass weighted average velocity magnitude seizes to fluctuate after about 1800 iterations which is an indicative of a converged stable solution.

iii. Report of Overall balances

As an additional means for cross checking convergence, overall balance of mass flow rate can also be used. For a converged solution, the net flux report shows nearly zero term.

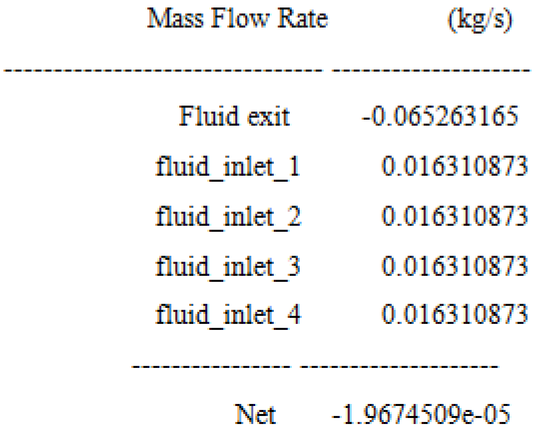

```
                    Mass Flow Rate          (kg/s)
-------------------------------- --------------------
                    Fluid exit       -0.065263165
                  fluid_inlet_1        0.016310873
                  fluid_inlet_2        0.016310873
                  fluid_inlet_3        0.016310873
                  fluid_inlet_4        0.016310873
                ---------------- --------------------
                            Net     -1.9674509e-05
```

The overall imbalance can be calculated as percentage of the net mass flow out of the mass flow at outlet and is compared to the minimum tolerable value of 0.2%. With regard to the mass imbalance between the four inlet nozzles and outlet port, in this case, sufficiently satisfies this solution criterion.

c. Solving

Solution computing is at the pinnacle of the processing simulation process. Calculation of solutions needs initialization of the flow field with specified initial values of the flow variables for the entire fluid domain or a zone in the domain before the iterating can start.

i. Initializing the solution

This step requires provision of initial solution for the solution domain in such a way that will allow the final solution to be reached in the shortest time possible. Solution can be initialized in two ways: Initializing the entire domain or providing patch values for certain flow variables on selected zones. Based on the initial values, flow variables will automatically be computed and updated from selected zones or as average values when entirety of the domain is referenced. Flow variables like x and y velocities are given in absolute reference frame since motion of the inter-disk fluid can be seen to be same with respect to any moving part or an global reference frame located at the origin.

ii. Performing calculation

After the solution is initialized, the number of iterations has to be set according to simulator's disposal. The program by using previous initial values as solution iterates to update these values for the active transport equations. As per the user's choice, the number of intervals with which the values of monitoring residuals can be constantly updated as iteration goes forward. FLUENT stores the inputs that define the problem and the results computed in two separate files: the case file and the data file.

5.2.3 Post processing in FLUENT

In post processing, the results are examined to review the solution and to extract useful data. This can be through graphical display or numerical report of results. In graphical display the overall flow pattern and determination of key flow features can be examined while in numerical reporting necessary integral quantities can be computed at boundaries of the flow domain. Amongst; the mass flow rate on boundaries, the moments about a specified center for selected wall zones and area-weighted average field variables on a surface in the domain are reported.

In the next chapter details of these output results will be presented.

Chapter 6

6 Post-Processing of Models and Result Discussion

The discussion so far doesn't go beyond explaining the theory, methodology and procedure for solving the flow in Tesla turbine. From here onwards, a comprehensive discussion of results will proceed to be followed by reflective remarks on technical performance merits.

Before this can go forward, certain non-dimensional operational characteristic correlations must be drawn first hand pertinent to the turbine visco-geometric features. These features serve as a background tools for explaining why certain key design characteristics vary the way they do.

The way the discussion is organized is first the two dimensional axisymmetric turbine CFD simulation model will be discussed by referring to unprocessed raw flow variables such as pressure and velocity field on selective flow surfaces. Secondary non-dimensional values calculated from these primary field variables are then calculated and their variation across the selected fluid surfaces is posted to study the inner workings of inter-disk flow between the rotor disks. In the same way, the 3D CFD model's result presentation goes by the same line of discussion. Up on drawing the necessary conclusions, the paper winds up by giving necessary recommendations on certain aspects which the author thinks might have had improved the already presented analysis and opens the opportunity for future investigation.

6.1 Non-dimensional Flow Parameters

Non-dimensional flow parameters are set of correlations that identify a set of physical parameters in which their superimposed effect give a unique flow characteristics and similarity irrespective of certain geometrical features. In doing so, dimensional flow forms provide a compact and economical way to represent analytical solution or output from certain CFD model.

For the current problem, the following non-dimensional parameters are selected to in order to study the effect two major operational variables, namely, disk row rotational angular speed and fluid mass flow rate in addition to the geometrical design feature such as the number of fluid supply nozzles.

a. Tip Velocity ratio (ϕ)

The tip velocity ratio relates the radial velocity of the fluid at the entrance to the disk bank to the tangential velocity at the disk periphery.

$$\boldsymbol{\phi = \frac{u_{in}}{\omega r_{in}}} \qquad (6.1)$$

where:

u_{in} = Inlet Radial Velocity

ωr_{in} = Disk Tip Tangential Velocity

The tip velocity ratio is indicative of the relative angle of flow occurring at the disk row inlet.

b. Loading Coefficient (λ)

The loading coefficient represents the specific power output of the disk assembly for every unit of circumferential (swirl) velocity the disk traverses in its rotational orbit.

$$\lambda = \frac{\frac{P}{\dot{m}}}{V_{in,d}{}^2} = \frac{\frac{T.\omega}{\dot{m}}}{(\omega r_{in})^2} = \frac{\omega(r_{in}V_{in} - r_{out}V_{out})}{(\omega r_{in})^2}$$

$$\boldsymbol{\lambda = \frac{(r_{in}V_{in} - r_{out}V_{out})}{(\omega r_{in}{}^2)}} \qquad (6.2)$$

Given a specific inlet and exit rotor radius at certain angular speed, the loading coefficient characterizes the power intensity of a given multiple disk turbine with all its design features considered.

c. Non-dimensional pressure drop across the disk row

The non-dimensional pressure drop between the disks is given as,

$$\boldsymbol{\overline{\Delta P} = \frac{(P_{out} - P_{in})}{(\rho\omega^2 r_{in}^2)}} \qquad (6.3)$$

where:

P_{out}= Total pressure at exit conditions

P_{in}= Total pressure at inlet conditions

ω = Angular speed of the rotor disks

r_{in}= Disk row inlet radius

The non-dimensional pressure drop can be referenced to the pressure drop only between the disk row or it can be used to indicate the pressure drop occurring from the fluid injection nozzles right to central exit ports.

d. Power output

The power output of a disk-spacer assembly is given as a multiple of the angular speed of the disks and the total torque acting on the disk bank.

$$P_{out} = T.\omega \tag{6.4}$$

The total torque acting on the disk bank can be determined from the viscous torque along the rotational axis for individual disks. The total viscous torque can thus be found by summing up the viscous torques for all disks in the two dimensional model while this variable is calculated as a sum of twelve times the viscous torque on the inner disk plus two times the viscous torque for the outer disk to represent the two disks next to stationary casing wall.

$$T_{2D} = \sum_{i=1}^{14} T_i \tag{6.5}$$

$$T_{3D} = 2.T_{outer} + 12.T_{inner} \tag{6.6}$$

Viscous torques along the various axes different from rotational axis is negligibly smaller as compared to the principal axis. These torque (momentum) components arguably are causes of operational instabilities such as low amplitude vibrations and in some cases, disk surface warping when operated along sides with high temperature working fluid.

e. Total Efficiency

The total efficiency of the disk assembly is calculated with specific power output of the disk turbine row compared against the isentropic enthalpy drop between the disks.

$$\eta_{tot} = \frac{\frac{T.\omega}{\dot{m}}}{\Delta h_{is}} = \frac{\frac{T.\omega}{\dot{m}}}{\frac{\Delta P}{\rho}} \tag{6.7}$$

As can be seen on the above relation, the isentropic incompressible specific flow work in Tesla turbine reduces to the pressure drop across the disk bank times the specific volume of the expanding air between the disks.

6.2 Results and Discussion

6.2.1 Axisymmetric Two-Dimensional Model

To recap the overall simplifications assumed for the two dimensional axisymmetric model, fourteen disks are axially cascaded with fluid supply at the top. There are no slightly tilted tangential nozzles and the CFD model assumes that fluid admission is done all around the disk periphery.

Separate fluid simulations where performed for different angular speeds (300 rad/s, 500 rad/s, 700 rad/s, 900 rad/s, 1046.67 rad/s (design speed), 1200 rad/s and 1500 rad/s) as well as flow rate below the design flow (25%, 50%, 75%, 90% of the design flow) . In order to aid the discussion on the variation of selected field variables, line surfaces are constructed on entry to the disk gaps and the middle plane between each inter-disk space.

A contour plot of velocity magnitude for design rotational speed and flow is given in Figure 6-1. The plot shows a perfect symmetry of the flow field with respect to the mid-plane of rotation as there are two central exits placed equidistant from this plane both at the same outlet pressure condition. As can be evidenced from the same figure, behind each trailing edge of the disk, there is a vortex flow region that causes the turbine disk to lose a sizable portion of the available power.

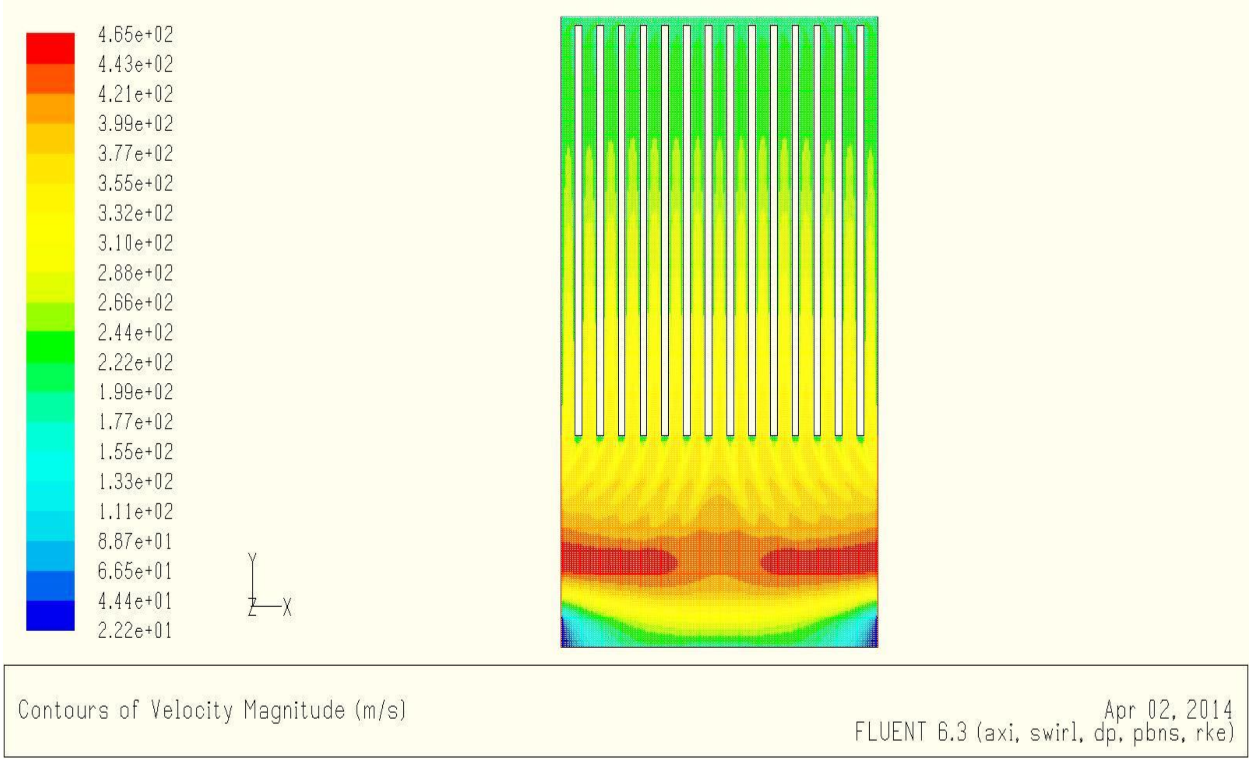

Figure 6-1: Contour Plot of Velocity Magnitude at Design Conditions

This drag effect in the trailing edge of the disks propagates itself towards the central fluid exit hole. In this region of vorticity, the fluid experiences reduced dynamic pressures as a result of the two streams of fluid on opposite sides of the disks coming to meet downstream accompanied by loses. This wake region eventually dies out towards the fluid exit.

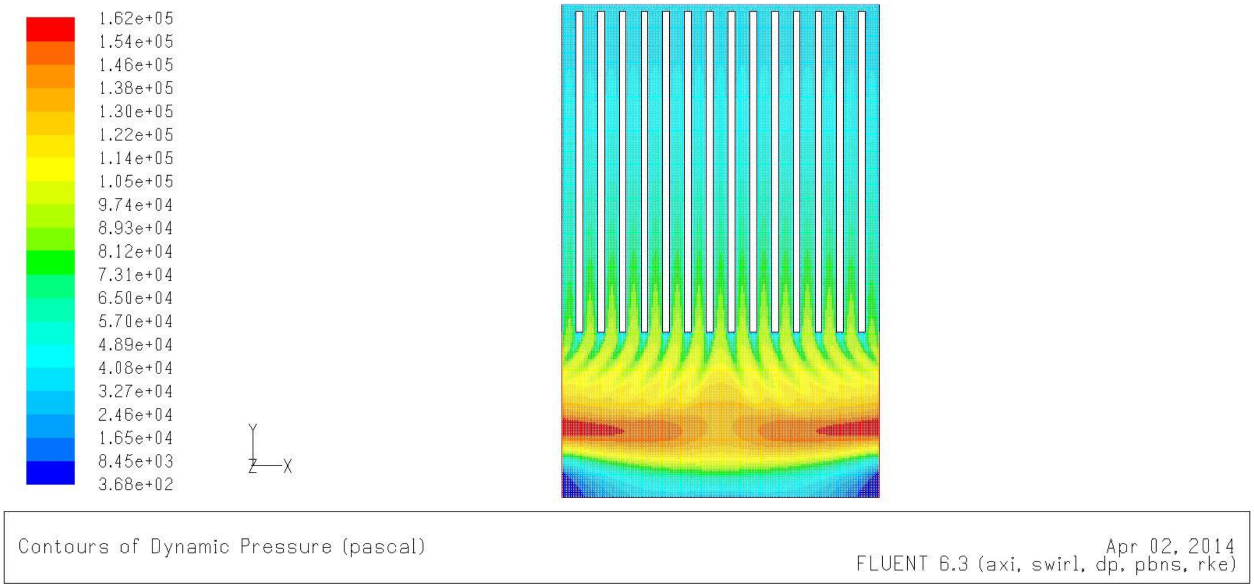

Figure 6-2: Dynamic Pressure Contour Plot for Design Case Operation

The following figure shows the swirl velocity on axial surfaces taken at four different radial locations in the eighth inter-disk space. These radial locations are at 52.8 mm, 68.51 mm, 84.3mm, and 100 mm from the central axis of rotation. From this plot, it can be easily perceived that the swirl velocity accelerates radially and decreases to the circumferential velocity of the disk as it approaches nearer to the disk due to no-slip boundary condition imposed on this surface. This accelerating fluid triggers increased dynamic pressure in the inter-disk space.

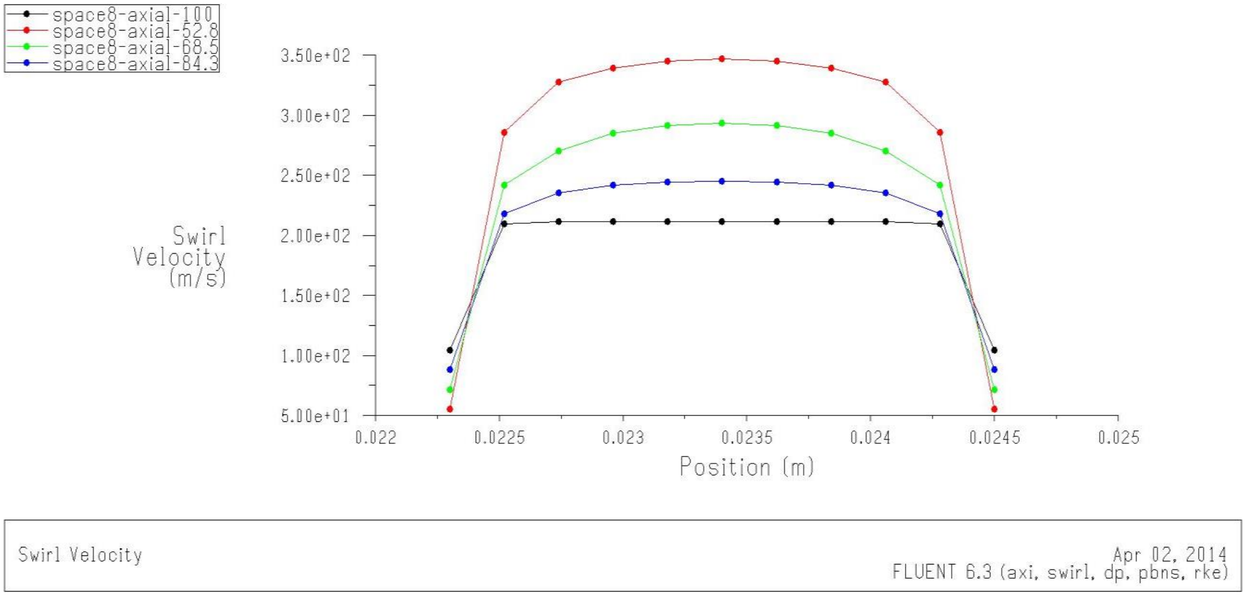

Figure 6-3: Axial Variation of Swirl Velocity [m/s]at Four Radial Location [m] in the Eighth Inter-Disk Space

Velocity profile exhibited by the flow in the totality of its domain is a flat one as it is the case that the flow lies in the turbulent regime of flow on which the design calculations were based. But there is some indication that the flow would experience transition to laminar regime as the velocity profiles tend to go curvier towards the center. Had the exit diameter of the discs were reduced to lower radial dimensions, the flow would have went laminar.

The pressure drop between the disks as they expand to give power is mild and pressure increase in the middle of the central exit as a result of higher swirl velocity component of the fluid rushing to exit the turbine.

Similar plot for the radial velocity axial distribution at the previously indicated radial positions are given in Figure 6-4. The graph indicates the presence of two symmetrically opposite regions (planes) in the disk gap where the radial velocity component is maximum. Apart from this, the radial velocity exponentially plummets to its center plane of rotation. This drop in radial velocity, as can be noticed from graph, increases as the flow traverses from outer periphery to the point it departs from the disk. The radial velocity decrease compared between the first two radial locations from the inlet is higher for the inlet as the flow experiences areal contractions as fluid races to enter narrower disk gaps.

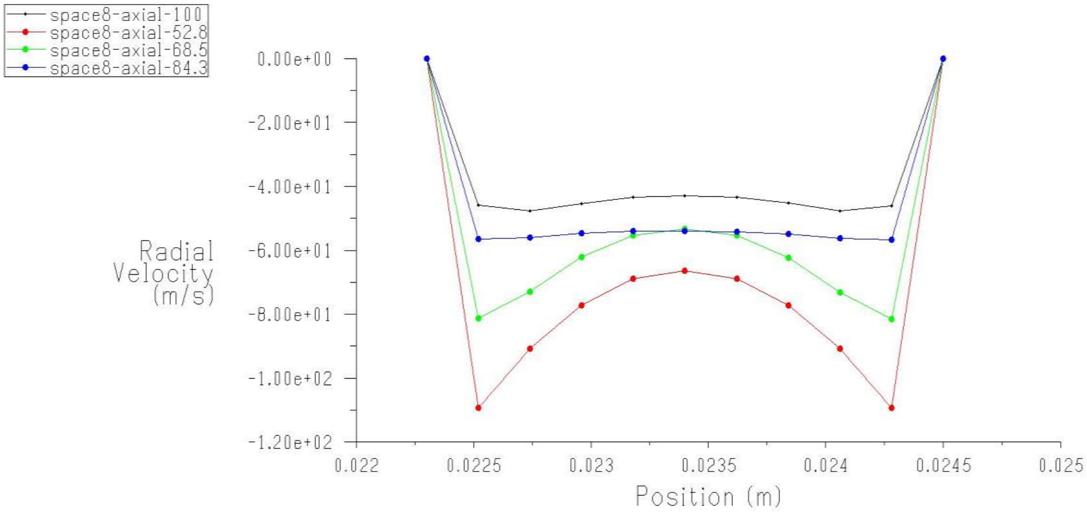

Figure 6-4: Axial Variation of Radial Velocity at Four Radial Location in the Eighth Inter-Disk Space

This areal contraction introduces axial velocity components as an addendum to the already existing swirl and radial velocity vectors. Since the flow is guided in between the disks, only axial components are predominant in the entry and exit points to the inter-disk spaces.

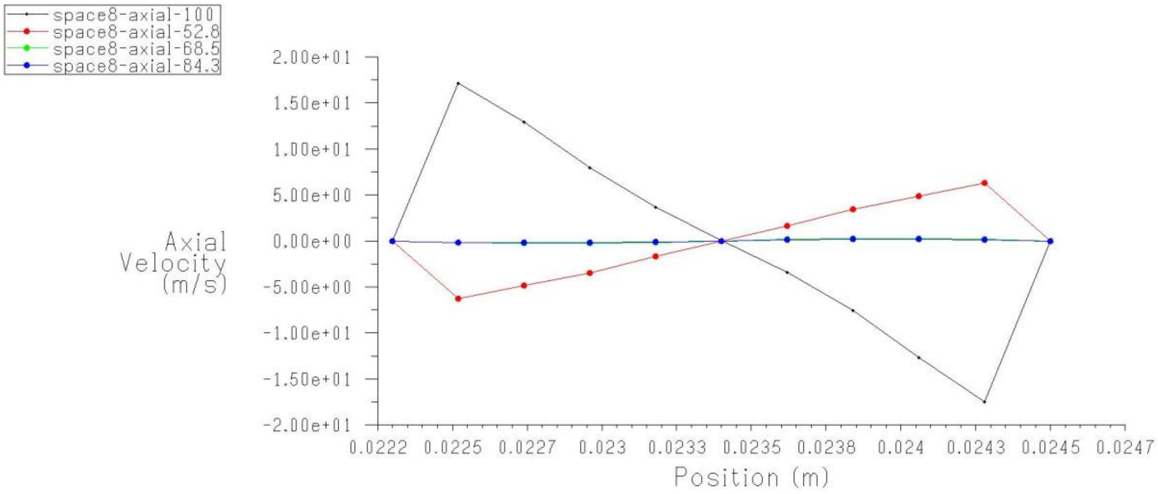

Figure 6-5: Axial variation of Axial Velocity at Four Radial Locations in the Eighth Inter-disk Space

Interestingly, the axial velocity distribution in the two halves of the inter-disk space shows that the velocity vectors are directed in opposite directions towards their respective adjacent disk's trailing edges. For disk outlet region, this can be explained by the diversion effect created as the reduced pressure region of the free vortex behind the disks tends to create sink hole towards which the flow stream are attracted to. It is expected that, the boundary layer goes thin faster from the point the axial velocity component inflects till the point of exit from disk row.

Contrasting the disk row and exit regions within the same half of inter-disk gap, the axial velocity vectors here too are directed in opposing fashions. It is also clear that the degree of introduction of axial component to the flow is higher at the inlet than at the point of departure.

Pathlines for the flow domain show an axially symmetric region divided equally to each side. Below the region where the path lines travel, there is a region where the fluid particles are out of reach indicating the flow exit port is sized larger than what is ought to be. This cross-section of the turbine is where the recirculation losses are predominant. The same regions see velocity magnitude vectors directed at opposite directions that they are intended to flow. The flow region exhibits lower dynamic pressure distribution as a result of adverse pressure gradients building due to flow non-conforming velocity magnitude vectors.

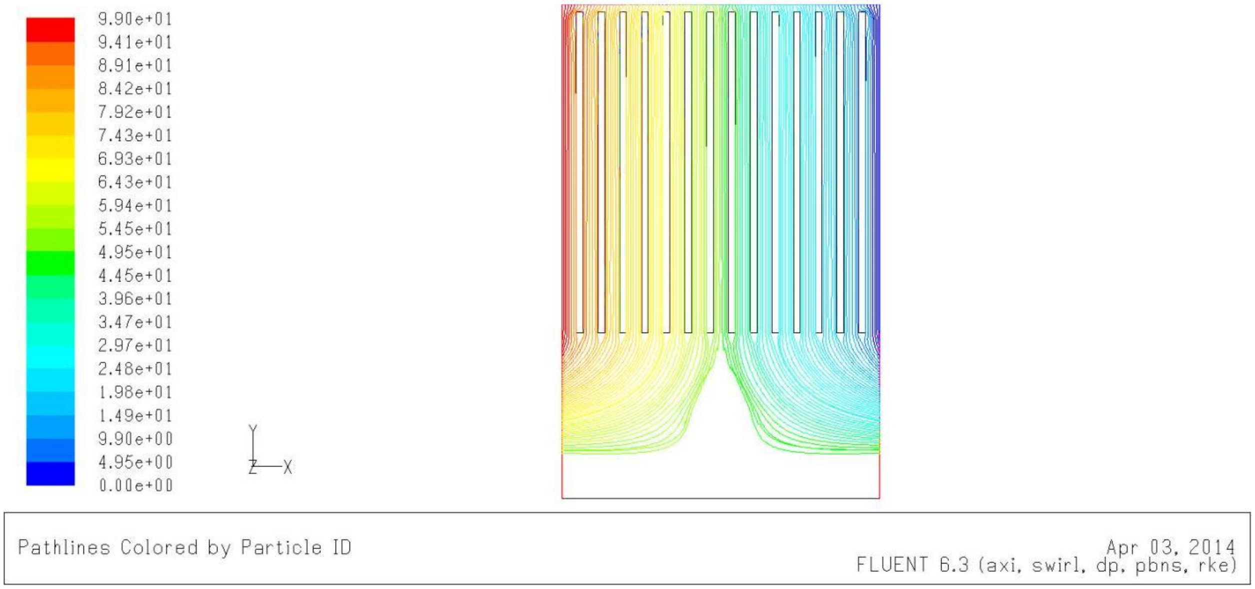

Figure 6-6: Fluid Pathlines for Two-Dimensional Numerical Model at Design Conditions

After carefully studying key field variables, secondary operational quantities such as those mentioned in section 6.1 are calculated based on field variables on selected surfaces of numerically quantified net mass flow rate or mass-weighted averaged property values (i.e. pressure, velocity components or viscous torques) on or crossing that surface.

Viscous torque acting on each disk surface is calculated by the FLUENT program itself from the shear forces acting on the different faces of the disk and the moment arm length supplied by the simulator. The program calculates also certain additional variables including the viscous coefficient on each disk, fluid viscous forces and moments acting on the three principal axes.

Numerical comparison between all the fourteen disks shows that there is only less than 0.9 % of difference in produced torque between the highest and lowest torques in the disk row.

A sample extracted data at design flow and rotor rotational speed with calculated non-dimensional parameters for all the disks and disk gaps is presented in table 6-1.

Table 6-1: Post Processed & Calculated Operational Quantities and Figures of Merits at Design Conditions

Disk (i)	Inter-disk space (j)	Viscous Torque ($T_{disk\text{-}i^{th}}$) [N-m]	Viscous Coefficient	Tip velocity ratio [-]	Loading Coefficient [-]	$\overline{\Delta P}_{jth\ space}$	Efficiency ($\eta_{disk\text{-}i^{th}}$) [%]
1	1	0.434054	0.70866	1.994513	0.530661	1.971744	0.210494
2	2	0.433841	0.708311	2.009436	0.466731	1.877691	0.23795
3	3	0.435868	0.711621	2.010318	0.454688	1.840361	0.234511
4	4	0.43684	0.713208	2.011016	0.450343	1.82665	0.233277
5	5	0.43692	0.713338	2.013386	0.451426	1.826572	0.232725
6	6	0.436113	0.712022	2.011479	0.449947	1.821179	0.232471
7	7	0.434896	0.710035	2.011667	0.452224	1.827463	0.232864
8	8	0.434848	0.709956	2.011927	0.45467	1.832892	0.234681
9	9	0.43646	0.712587	2.012623	0.452994	1.829224	0.233424
10	10	0.436857	0.713237	2.012828	0.451099	1.826145	0.232742
11	11	0.436806	0.713153	2.011057	0.44935	1.820818	0.232801
12	12	0.435912	0.711693	2.011074	0.451052	1.826455	0.232836
13	13	0.433266	0.707374	2.011309	0.45587	1.842329	0.233116
14	14	0.434691	0.7097	2.010611	0.467515	1.878501	0.201005
-	15			1.994852	0.531195	1.973221	

Even though the variation of torque is minute by the scale, examining the magnitude of torque on the disk cascade reveals a mirror pattern about a plane perpendicular to axis of rotation. This pattern of torque production is consistent with fluctuation of radial velocity magnitude profile in successive disk gaps.

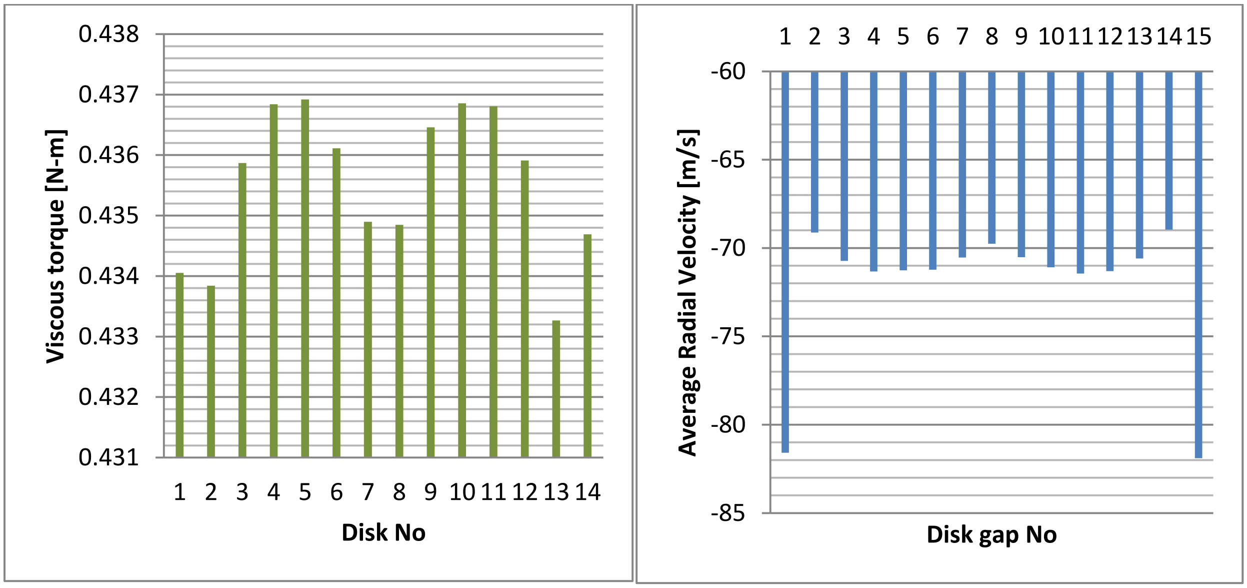

Figure 6-7: Comparison of Average Radial in Disk Flow Spaces with Viscous Torque [N-m] Produced by Each Rotor

Presence of radial velocity component of flow has been pointed as a source of flow losses rather not as an aid for entraining the flow to its exit. On the contrary, the pattern exhibited by these two profiles seems to suggest that the increase in radial velocity magnitude of the flow is matched by increase in torque on adjoining disk.

6.2.1.1 Effect of Angular Speed (ω)

To determine the effect of rotor angular speed on the different operational and merit quantities the fluid domain was simulated for seven angular velocities with separate simulations. From hereonwards, three disks and inter-disk spacings , namely the first, second and seventh disks will be chosen to study the variation of the previously stated comarison quantities.

Its observed that the torque decreases with an increase in angular speed as expected. This means that the turbine will be less adaptable to higher torques at higher speeds. Thefirst disk registered slightly higher torque in the lower and higher rotor angular speed spectrum while on the other hand, the middle disk in the disk bank (disk-7) performed better in the middle angular speed range.

The total nominal pressure drop plummets from the first inter-disk space to the seventh disk gap. But a non-dimensional pressure drop comparison between all the the three interdisk spaces proves that all the pressure drops are about the same and show no distinction between them with changing rotational conditions. Generally, the pressure drop decreases at a reduced rate when the rotor is made to rotate at higher rotatioal speed. If more sample simulation points beyond the maximum rotational velocity are taken this quantity stablizes Figure 6-8 proves this statement.

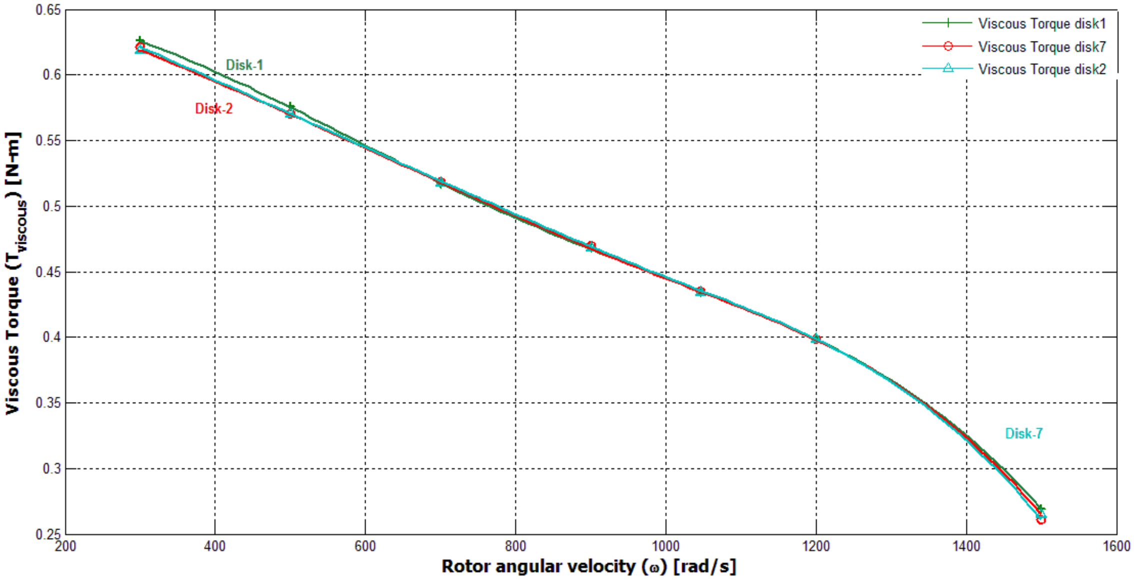

Figure 6-8: Torque Output [N-m] Variations with Rotor Angular Velocity [rad/s]

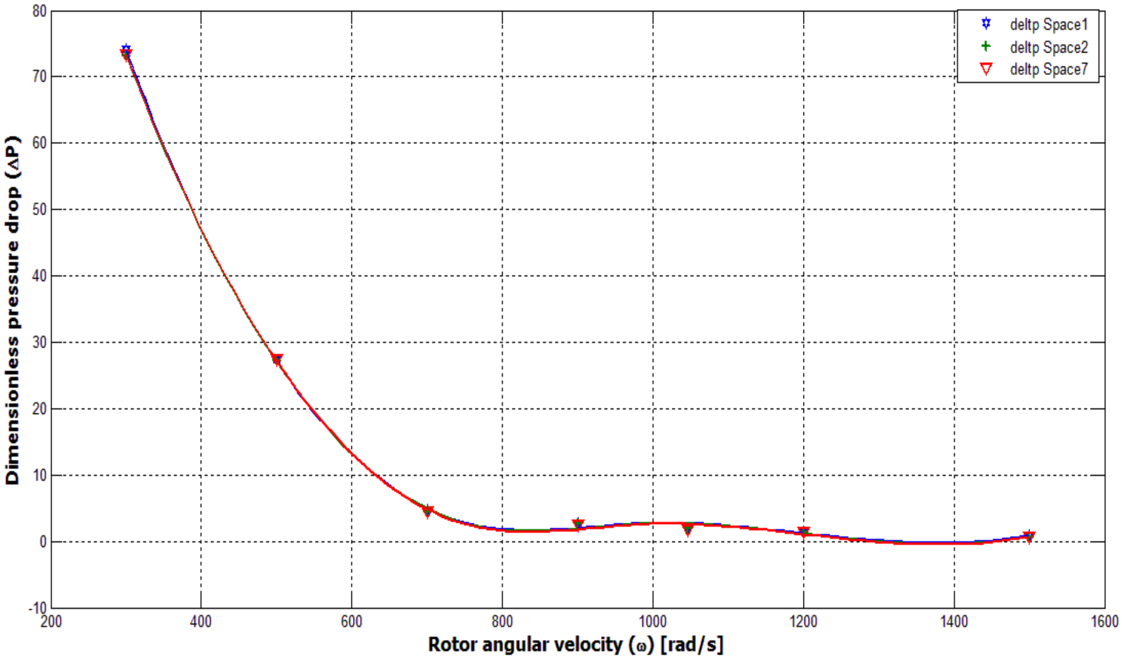

Figure 6-9: Non-Dimensional Pressure Drop [-] Change with Rotor Angular Speed [rad/s]

Since the difference momentum of velocity between the spacing inlet and exit is fairly constant, the loading coefficient in the successive disk inter-disk spaces diminishes with increasing rotor rotational speed. Figure 6-9 indicates that space 1 has a higher tendency to exert viscous momentum on its adjacent solid surfaces per unit mass of fluid flowing within its boundaries.

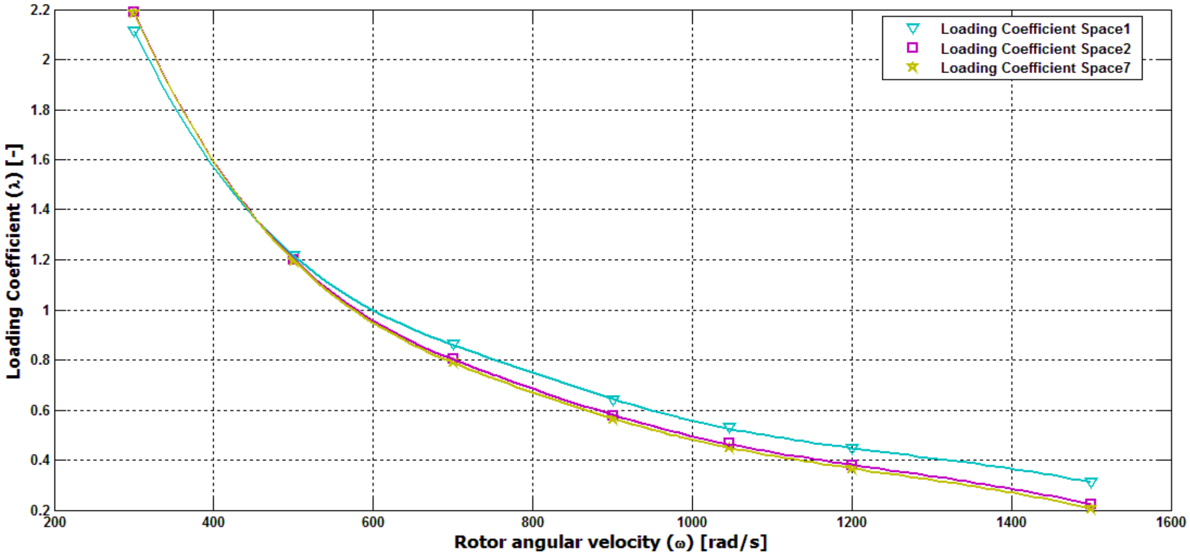

Figure 6-10: Loading Coefficient [-] versus Rotor Angular Velocity [rad/s]

The total power output of the rotor assembly was calculated as the sum of the output of each turbine rotor. The result showed angular speed of 1200 rad/s to be the maximum output point beyond which the turbine's yield would fall. This would indicate that additional power can only be determined if the turbine's design can accommodate additional set of disk row.

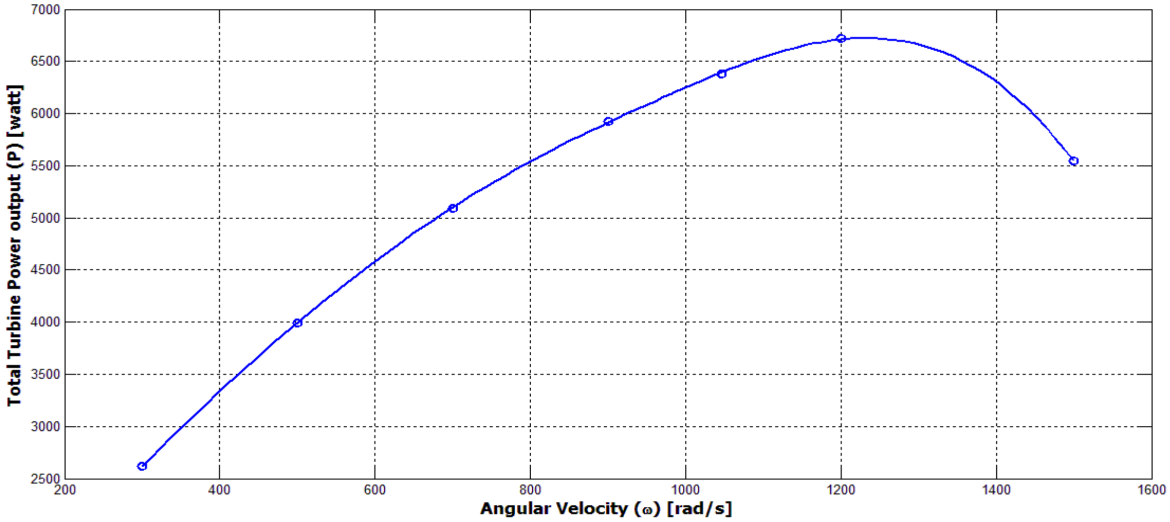

Figure 6-11: Turbine Total Power Output [watt] versus Rotor Angular Velocity [rad/s]

By taking fluid conditons at the inlet to each disk spacing, the efficiency of each disk in the disk bank were computed. The calculation reaveled a widening gap in performance between thedisk adjoing the static casing and the rest group of disks following this disk as the rotor runs faster. Generally, the efficiency curve increases at decreasing rate even falls under higher angular speeds for the first rotor.This decrease in efficiency was triggered by higher nominal pressure drop in the first spacing which in turn caused higher air flow to go to this gap. Being located next to a static wall, the part of the disk wall adjacent to it produced lesser torque than what it must have had if linear projectionswere drawn from smaller operational velocities.

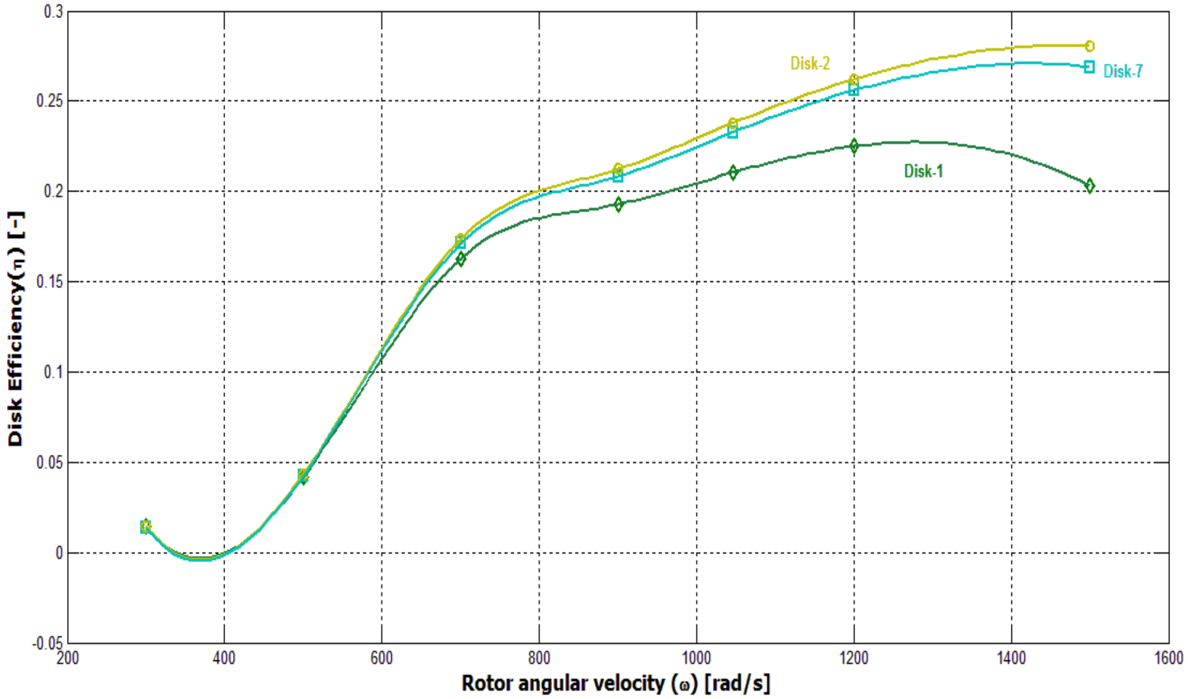

Figure 6-12: Variation of Individual Disk Efficiency [-] with Rotor Angular Velocity[rad/s]

By collating dynamic and fluid state information on peripheral fluid inlet and that of central air exit ports, the total efficiency of the turbine was calculated. Variation of rotor running speed established the existence of tipping point for maximum efficiency at the same spot where the maximum power output was found.

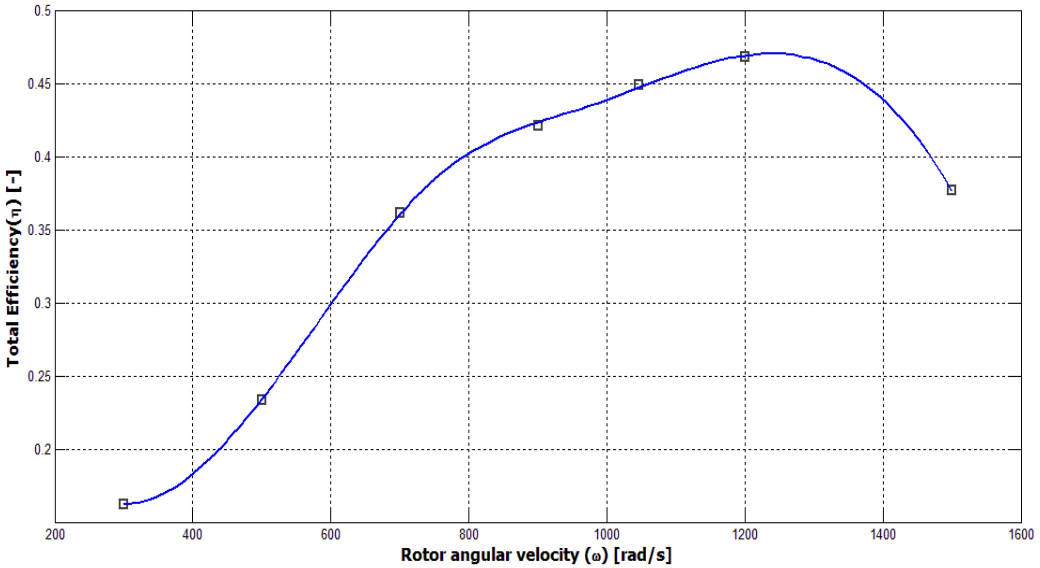

Figure 6-13: Overall Turbine Efficiency [-] Variation with Rotor Angular Rotational Speed [rad/s]

6.2.1.2 Effect of Mass Flow Rate Variation

Similar analysis with variation in air flow rate was simulated at four other flows besides the design flow rate. This is intended to ascertain the existence of maximum operating point for flow or if the efficiency indefinitely increases as the flow goes to zero where exorbitant efficiencies such as Tesla’s claim of 95% would be achieved.

As expected, dimensionless pressure drop on the first spacing is higher than any of the other spaces. Readjustment of flow to reduced flow conditions triggers a drop in nominal and non-dimensional pressure drop across all the spaces.

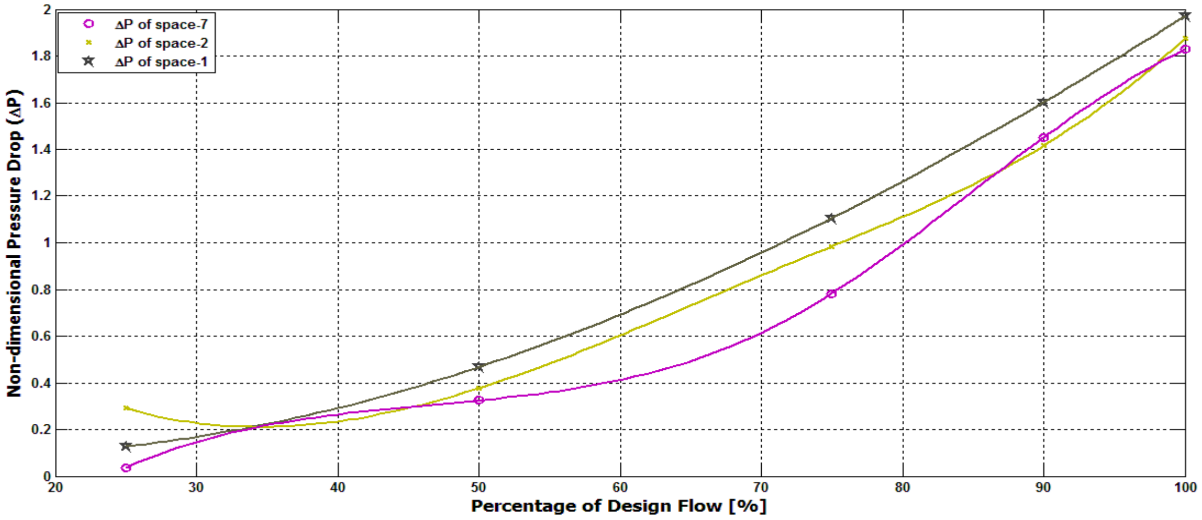

Figure 6-14:Non-Dimensional Pressure Spectrum at Reduced Flow Rate Portions

Proportionally, the shear force acting along each disk surface drops to produce smaller drag on the disks which in turn a smaller Viscous torque.

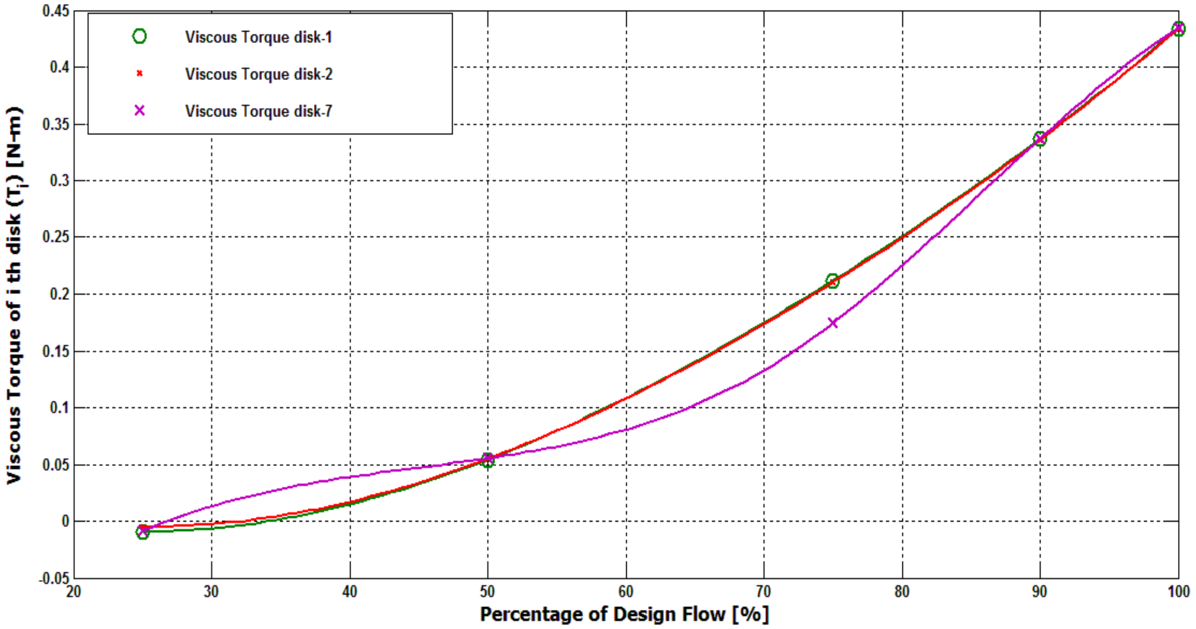

Figure 6-15: Viscous Torque [N-m] Variation for Different Flows at and Below Design Rate

It can be seen from the graph above that at and below 25 % of design flow the disk turbine produces negative torques. This signals that the irreversibility created by fluid introduction, the wake in each disk trailing edge and ventilation losses between the disks dominate the viscous drag force acting in the direction the rotor was intended to rotate.

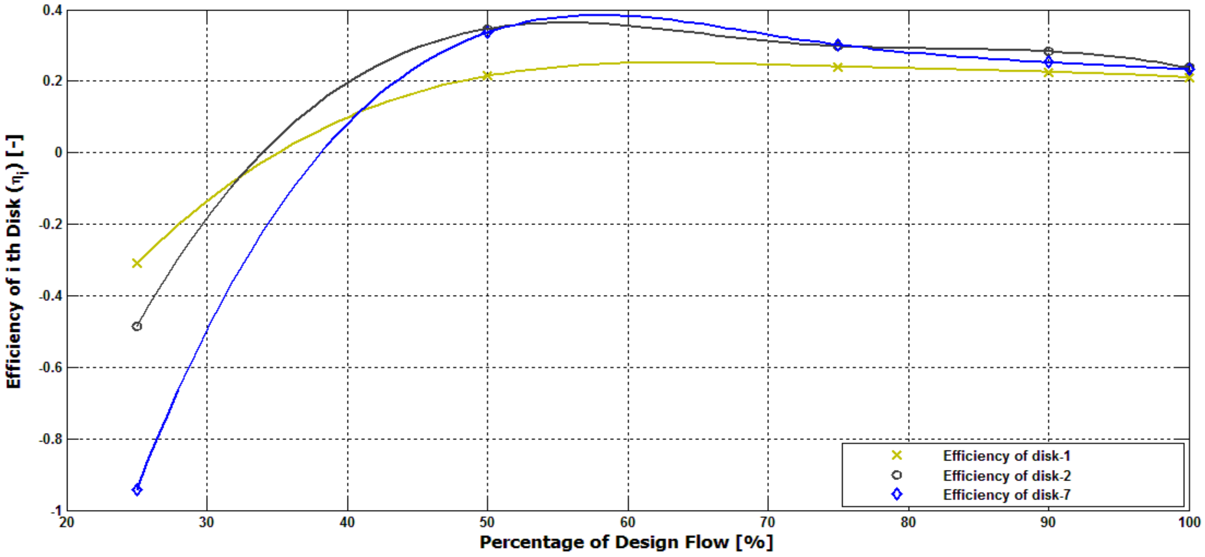

Figure 6-16: Efficiency Variation of Selected Disks with Percentage of Design Flow [%]

In this thesis, the undesirable negative torque terms acting on the rotor disks have been kept to demonstrate the extent of irreversibility in relation to a fixed reference point, zero. Hence, if the reported efficiency below zero has been spotted, it should be understood that this efficiency is actually a null efficiency but as a means for comparison the degree of deterrent forces on a respective disk.

As noted earlier, as air flow goes down the pressure difference between the disk row entrance and exit drops faster than the total torque produced by the disk bank. This in turn will upsurge the efficiency of each disk with maximum efficiency at 34.58% for the second disk at half portion. Further reduction in flow rate causes separation of the fluid particles from the disk walls, this subsequently causes the fluid stream lines to drift apart hence moving in fairly unguided motion. These unguided streamlines may travel in reverse to the normal direction of motion contributing to reverse shear force on the disk surfaces.

The flow was also checked if the reduction in mass flow rate caused the flow to transform from the turbulent regime at the inlet into laminar for which the applied set of governing equations would not exactly depict the actual scenario. Using Nendl’s visco-geometric criteria for flow transition, It was determined that 25% of designed flow was at laminar regime of flow but didn’t yield far-off result from the turbulent case which proved our earlier prediction that the negative torque could have come from flow separation of the surface of the disks.

The total output of the Tesla turbine is plotted as follows.

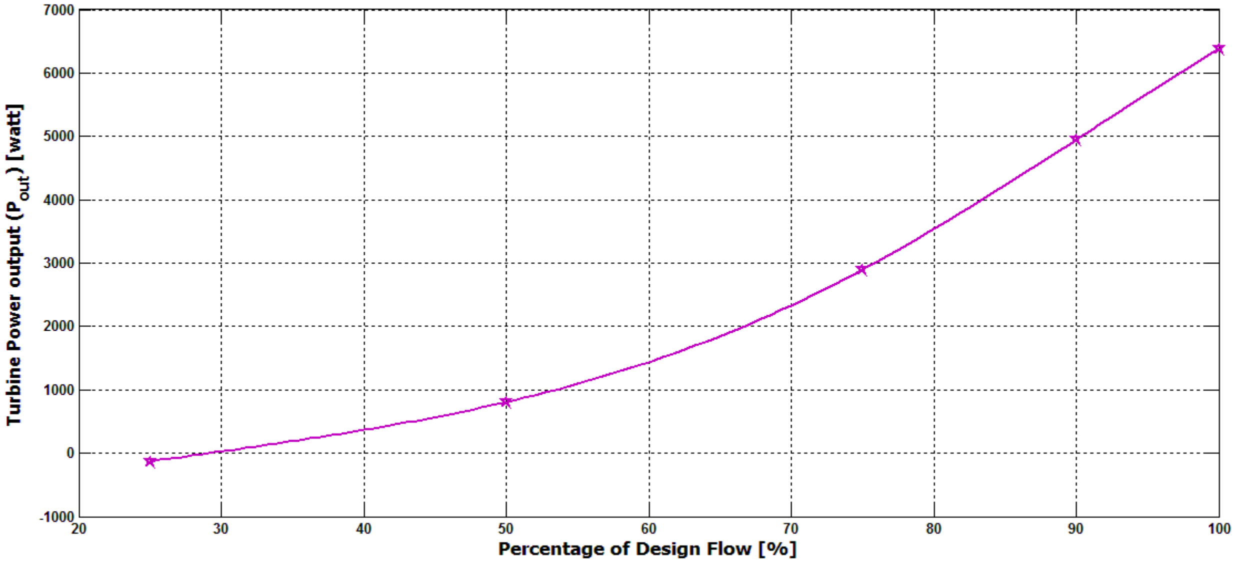

Figure 6-17: Total Power Output [watt] Change with Percentage of Design Flow [%]

As was the case for the rotor speed variation, the total efficiency of the disk row was calculated for the five different operating points as it is shown in the plot below.

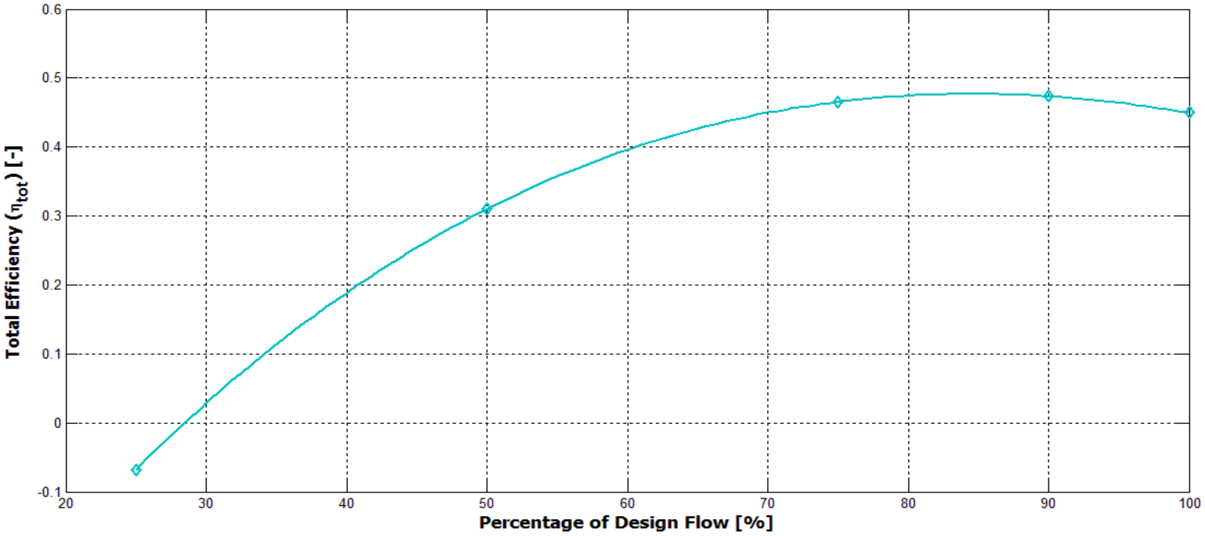

Figure 6-18: Total Efficiency [-] Variation with Flow Percentage [%]

The maximum turbine efficiency is found not at the design flow but at 90 % of the design discharge.

6.2.2 Three dimensional Model

The three dimensional models consist of even number of nozzles discretely located around the disk entry radius on the casing. Three different combinations are simulated; namely, two, four, and six nozzles. These models bridge the knowledge gap on certain shortcomings of two dimensional models such as the tangential variation in dynamic quantities, three dimensional propagation of vortices and wakes and also energy lost due to non-conducting rotor surfaces, as in reality, full admission is not feasible on common applications as the nozzles are tangentially spaced apart.

It goes without saying the models are not accurate portrayal of actual operating conditions as the initial model consisting half the number of the total disks in the bank was incapable of being solved due to limitations in the available computer resources. As was demonstrated in the 2D model, the variation in viscous torques between consecutive disks is less than 0.8 % which gives favorable advantage to the simulator to reduce the total disk cascade to two rotor disks. These two disks represent two principal flows: A flow between a fixed surface and finite rotating disk and a flow between two finite co-rotating disks.

In due process, the disk inlet velocity conditions were maintained and flow flux was set according to the pertinent flow feed area. All the studied models were constructed with the same flow inlet angles. The same quantities and method that are used to compare flow characteristics and turbine merits are also used here with the exception of mid cross sectional area contour field plot for the two gaps.

It must be noted that variations of the two operational parameters were performed on the six-nozzled turbine while a design case comparison was done on all nozzle configurations.

6.2.2.1 Design Case

In order to be able to understand the different velocity, pressure and wall flux patterns exhibited by the turbine, two surfaces that bisect the respective disk gaps, along with the disk surfaces, are selected. A dynamic pressure contour plot for design case rotational speed and flow on the second mid-gap surface is given in Figure 6-18.

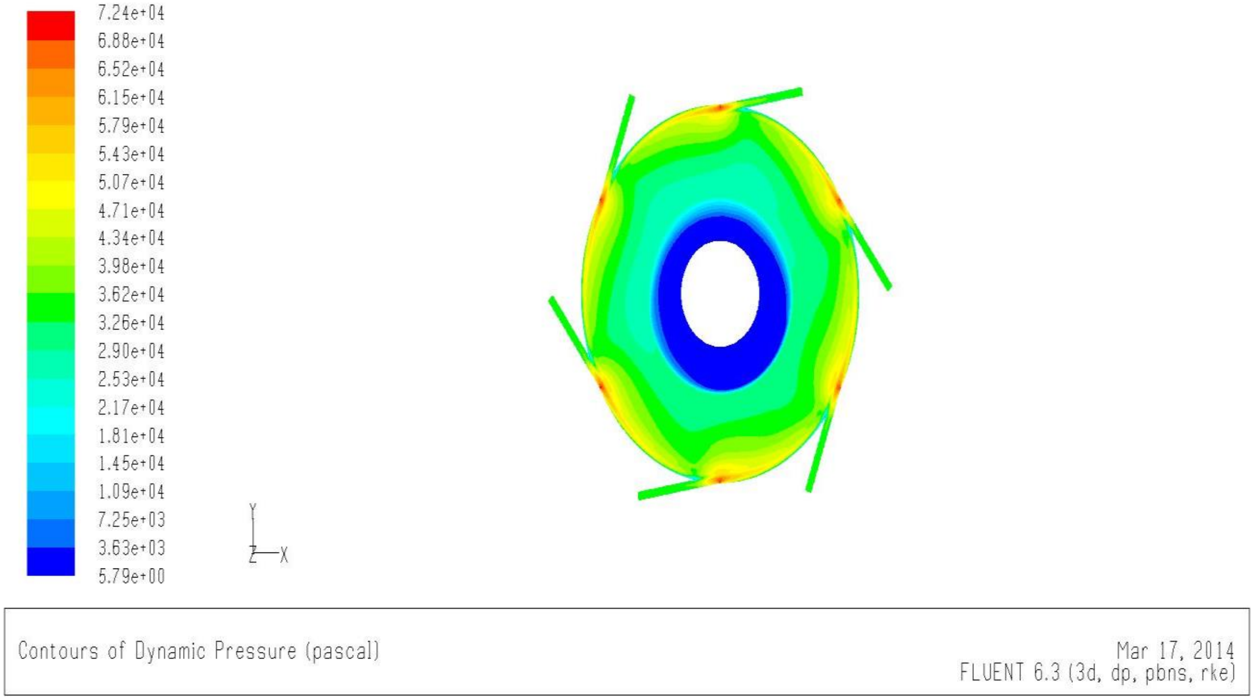

Figure 6-19: Velocity Magnitude Contour Plot at the Mid Surface to Co-Rotating Disks

The dynamic pressure directly describes the velocity magnitude profile of the flow domain. Examining the 3D model, It can be understood that the velocity magnitude does not exactly follow a spiral pattern of reduction from disk inlet to exit port but rather in sprocket like pattern, depending on the number of nozzles, which is created as a result of higher velocity fluid entering the inter-disk space and exchanging momentum with already traversing fluid particle at lesser momentum level.

Initially, it was understood that the radial velocity component keeps on incrementing due to the reduction in flow area experienced when the fluid particle travels radially inwards. This same understanding was applied in the design using two-dimensional fluid model and this was confirmed by the 2D axisymmetric CFD flow model. In contrast, the 3D model shades a different light on this scenario as can be seen in the graph below.

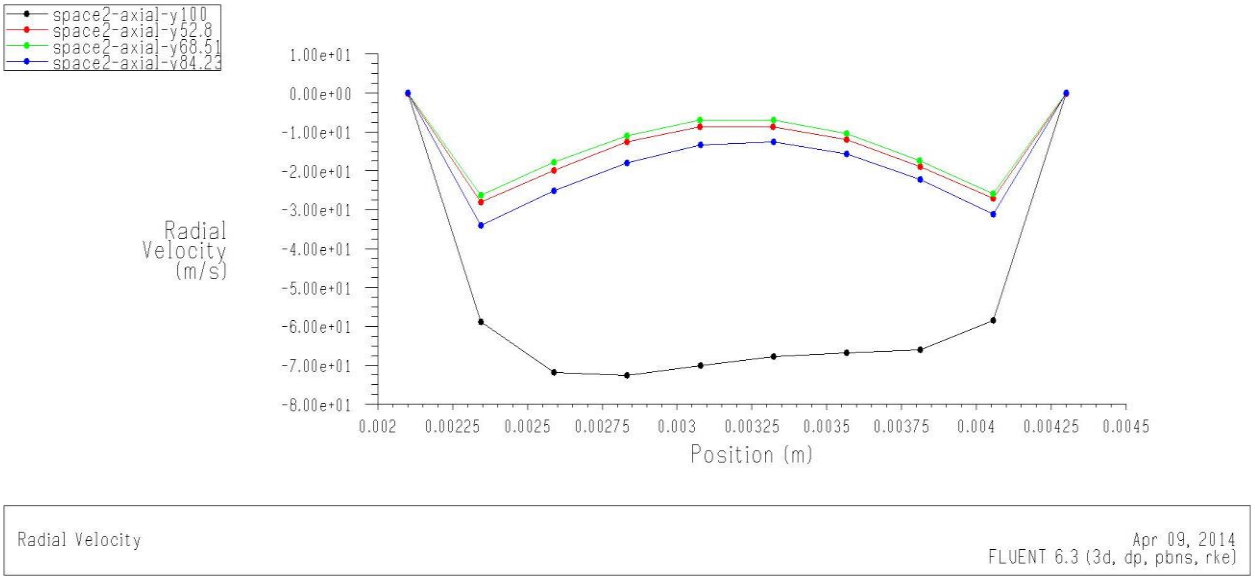

Figure 6-20: Axial Variation of Radial Velocity [m/s] Marked at Four Radial Locations

According to the 3D model, as the fluid particle travels inwards, the radial velocity component steadily falls to its low magnitude till it upsurges before leaving the disk row. As for the axial variation of radial velocity, it possesses the same distribution with axial inflection point similar to the 2D model. Contrasting the 2D and 3D models, the disparity in radial velocity from any of the inflection points to the relative maxima between the inflection points, the 3D model registers lower than the former. This type of velocity profile occurs because of the existence of laminar sub-layer region within the mainly turbulent boundary layer. This region is the same region where the viscous forces dominate the momentum forces of flow.

Similar, plot for inter-disk tangential velocity spacing is given in Figure 6-20. The oddities of 3D model happen here too. As opposed to augmentation of tangential velocity component in the radial direction of motion, the tangential velocity distribution in the 3D model is going forward in the direction of tangential velocity decline. The possibility of radial inward tangential velocity incline or decline depending on local balance of force components (inertial, viscous, Coriolis or centrifugal forces) has been reported. [51]

The relative spread of tangential velocity says something about where the greatest portion of fluid energy is transferred to the rotor disks. Swirl (tangential) velocity components at the four radial locations are more or less equally spread (difference between each component) as opposed to the current model which has wider radial tangential velocity variance at the first span of the gap followed by the second span from entry.

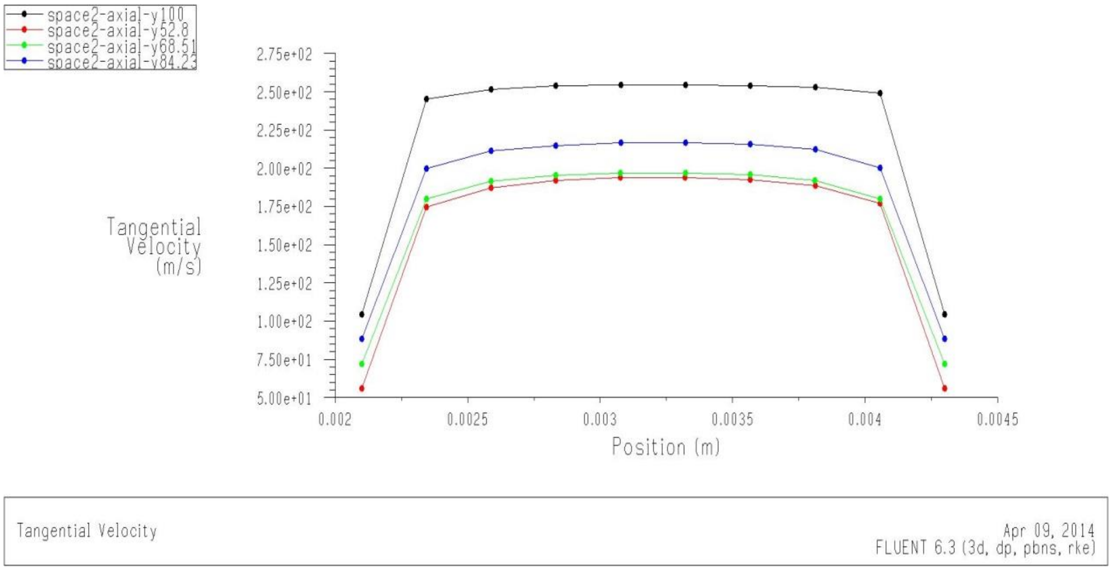

Figure 6-21: Axial Variation of Tangential Velocity [m/s] Marked at Four Radial Locations

As was discussed in section 6.1, the driving force for viscous torque production is the difference of tangential velocity component multiplied by its respective radial location between the peripheries of each radial spans. Basing this relationship, it is found that from simple computation with both models, energy transfer is the most at the inner span of the disk for the 2D model while highest rate of torque transfer takes place within the outer most periphery of each disk. Interestingly, the outer two regions of the disk surface transfer fairly the same amount of viscous energy in the 2D axisymmetric model.

Axial velocity distribution in the 3D model resembles that of the two-dimensional model with axial magnitude higher at the inlet and lower at the disk bank exit. Higher axial velocity is explained by the higher inlet velocity magnitude attained at the nozzle outlet is. On the other hand, the reduction in axial velocity at the outlet is much related to the simplification of the 3D model not having enough disk rows that could discharge cascades of air jets pushing their way through to the outlet while exchanging momentum and contributing to augmentation of axial velocity on subsequent rows.

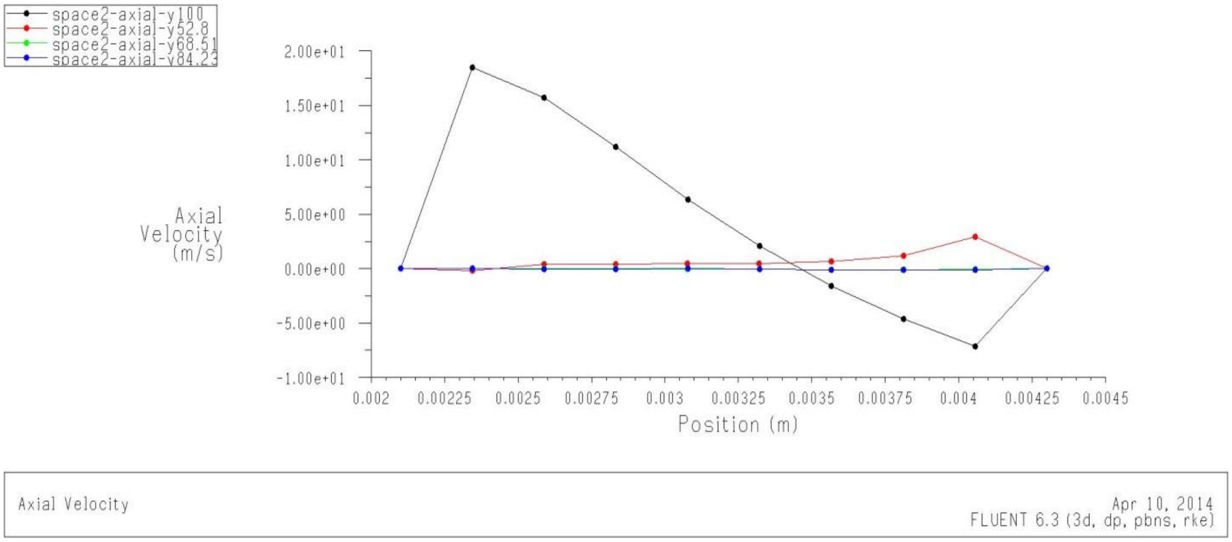

Figure 6-22: Axial Velocity Distribution on the Second Inter-Disk Space at Four Radial Locations

The fluid flowing in the space next to the casing, as it is discharged, encounters velocity steam from the second inter-disk space which in turn imparts energy to it, which explains why its axial magnitude is higher at the left end. Since the left right half of this stream travels less and less towards the central exit, with no pressure gradient on its front, have no chance of its velocity vector being deflected in opposite direction as in the first case.

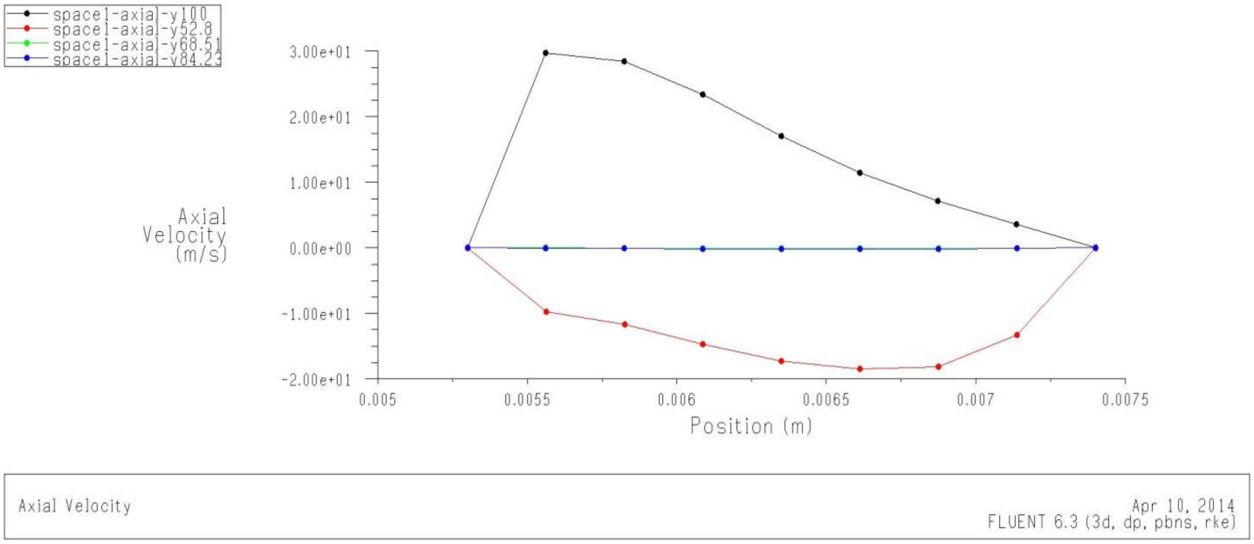

Figure 6-23:Axial Velocity Distribution on the First Inter-Disk Space at Four Radial Locations

From here on, optimization of the operational parameters and selection of nozzle number for performance superiority will be carried out. As was the done for the 2D models, similar comparison quantities will are plotted against the optimizing variable.

6.2.2.2 Effect of Angular Speed (ω)

Seven separate simulations were carried out with same rotor angular velocities as the ones for 2D models. The three dimensional model uncovers more losses that 2D models failed to accurately depict.

It is shown that as the turbine accelerators to higher rotational speeds, the pressure drop disparity between consecutive disk spaces narrows down.

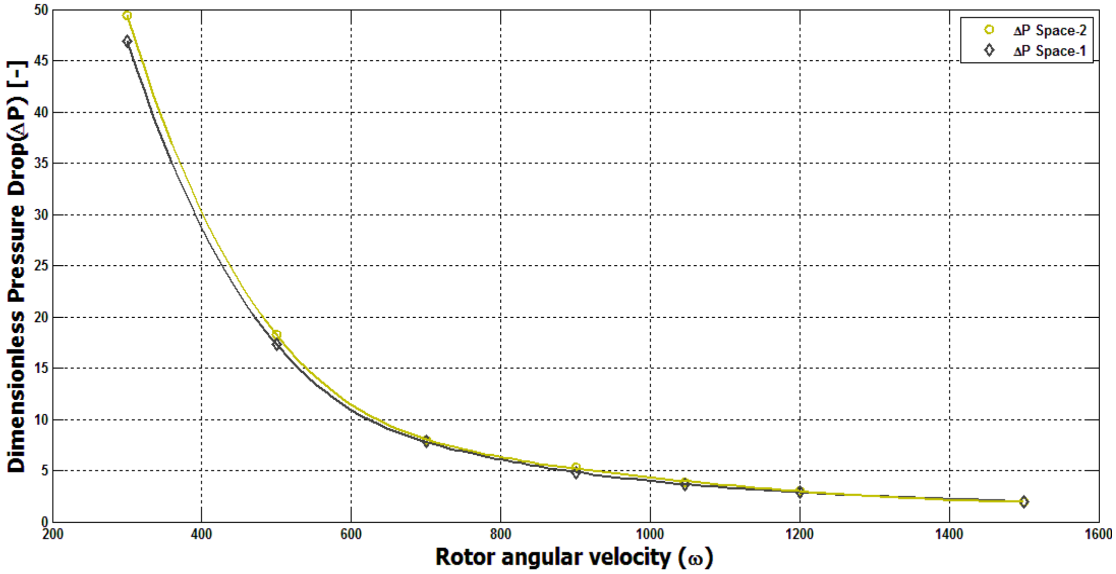

Figure 6-24: Pressure Variation in the Inter-Disk Spaces with Change in Rotor Angular Speed [rad/s]

The pressure drop is accompanied by the reduction in tangential velocity which in turn reduces the loading coefficient between the spaces. This means that the enthalpy drop in between the disk spaces divided by the square of disk row tangential speed drops.

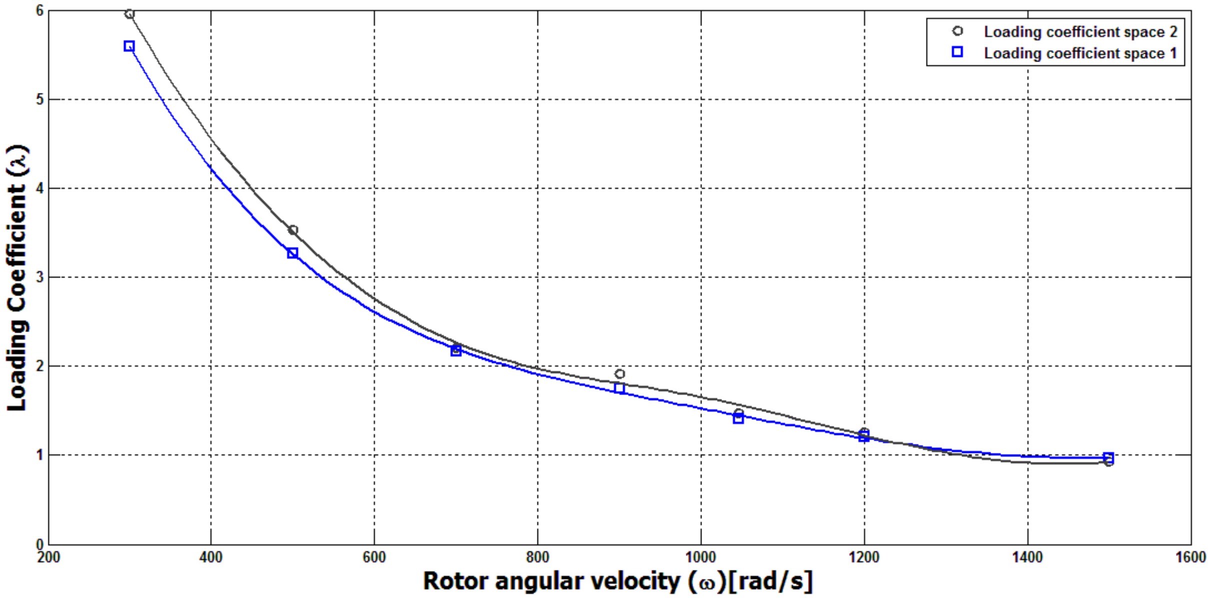

Figure 6-25: Loading Coefficient [-] Variation with Angular Speed [rad/s] (3D model)

The calculated loading coefficients for 3D model, compared to its 2D counterpart, are higher because disk row exist tangential velocities are a lot lower than the former which gives it a greater velocity momentum difference between the flow inlet and exit areas.

By taking disk row inlet and exit conditions, the respective efficiencies of two rotor disk have been computed. As the rotor disk run faster, they become more efficient in utilizing the available energy.

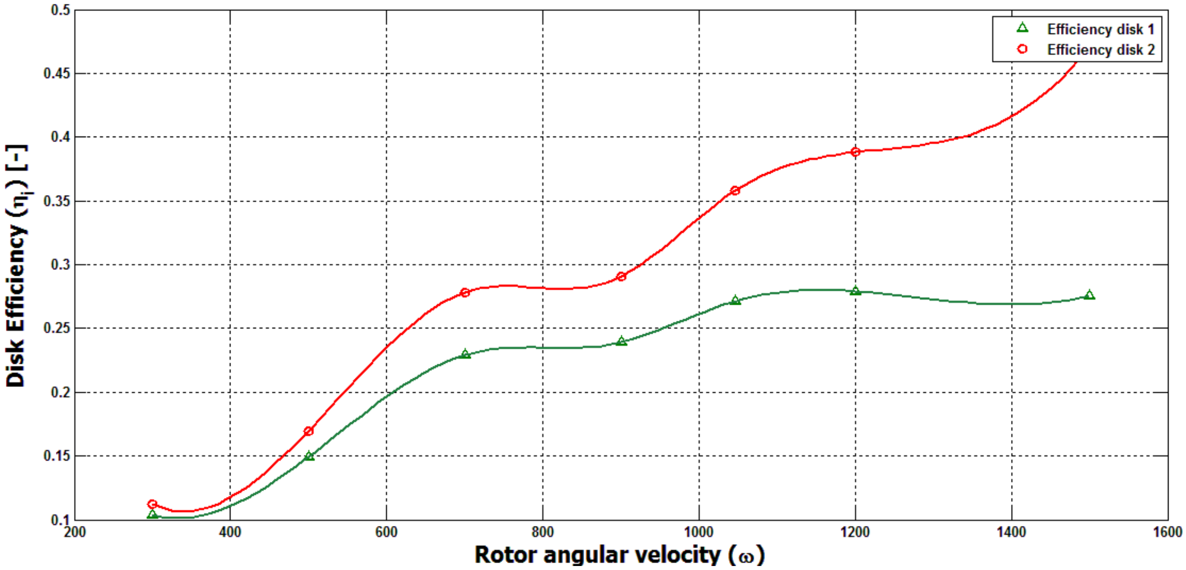

Figure 6-26:Variation of Individual Disk Efficiency [-] with Rotor Angular Velocity [rad/s]

The efficiency variance grows from about 8.6 % at 300 rad/s to more than 70% at about 1500 rad/s. The widening efficiency gap between the outer and inner disk is mainly created as a result of lower disk bank output tangential velocity in the outer inter-disk space than those gaps on the inner side.

This variance in exit velocity across the disk spaces grows with disk angular speed and is more pronounced between the first two disk gaps. Similar deduction can be taken with the two dimensional fluid model where the inter-disk exit tangential variation is only noticeable in two outer most disk spaces.

The variation of total efficiency of the disk row comprised of fourteen disks with run at different rotor speeds is presented in Figure 6-26. Similar to the previous case, maximum turbine efficiency is achieved at about 1200 rad/s. The maximum isentropic efficiency achieved for this turbine is 16.61 % which is more than 64% lesser than its comparative operation point for the 2D model.

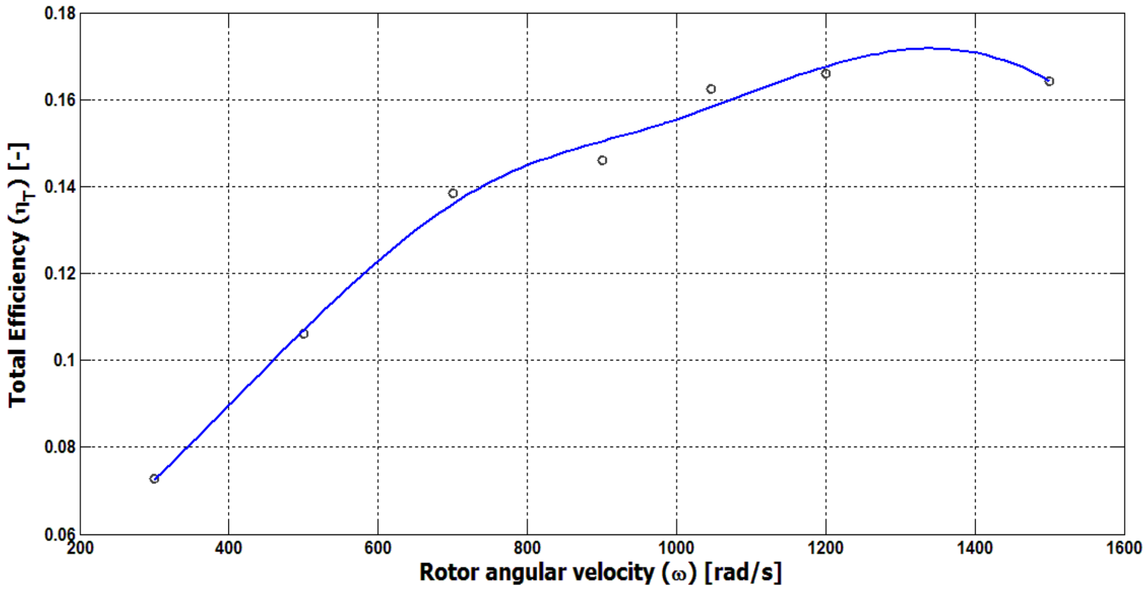

Figure 6-27: Variation of Total Efficiency [-] of the Turbine with Rotor Angular Velocity [rad/s]

The 64 % drop in efficiency accounts for drop in efficiency due to nozzle exit losses, three dimensional propagation of disk wakes, ventillation losses due to pressure gradient on energy transfering surfaces as a result of not having full circumferential fluid admission.

As can be evidenced from the previous two graphs, sufficiently high disk efficiencies, if not comparable to conventional turbines, can be achieved by the inner rotor disks had the losses to the aforementioned areas become primarily dominant.

Additional comparison of power output between the two models, the 3D model has shown a reduction of 14.37% at 1500 rad/s to about 41 % at 300 rad/s in the lower end of yield.

6.2.2.3 Effect of Flow

In the same way the disks' angular velocity was varied, the turbine was simulated with different portions of the design flow rate to examine its effect on the selected comparison quantities. Since the initial assumption taken is to consider the flow to be incompressible, this can simply be done by reducing the inlet velocity magnitude by the required portion. The velocity specification is relative to the adjacent boundary zone which takes away the complexities incurred for converting the local vector into a global one.

The total power output of the entire disk bank with the available portion of design flow is presented in the following figure.

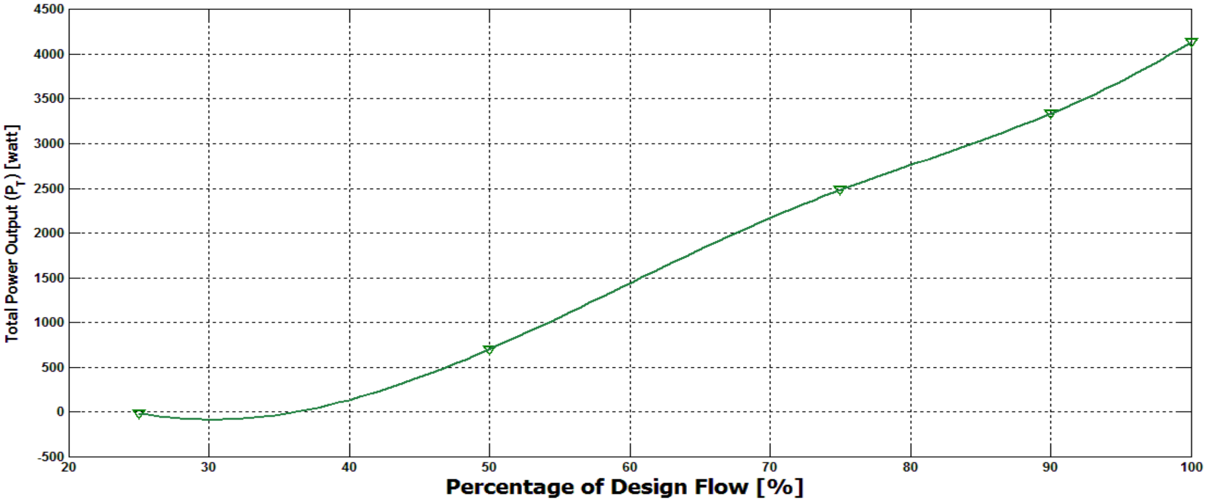

Figure 6-28: Total Yield of the Disk Turbine [watt] at Different Portions of Design Flow[%]

Comparing the current 3D model with the previous 2D CFD model, up to 35% reduction in turbine yield was registered with no apparent maximum power point. This is set to indicate further augment in flow will consequently result in increased output until yet the limiting flow is reached for the prevalent turbine geometry.

The same can be said about the total turbine efficiency where it showed no sign of inflecting downward since it has not yet reached its efficiency peaking flow. The fact that the total efficiency is generally increasing at reduced rate is a precursor for the existance of a peak efficiency point at flow beyond the design flow rate.

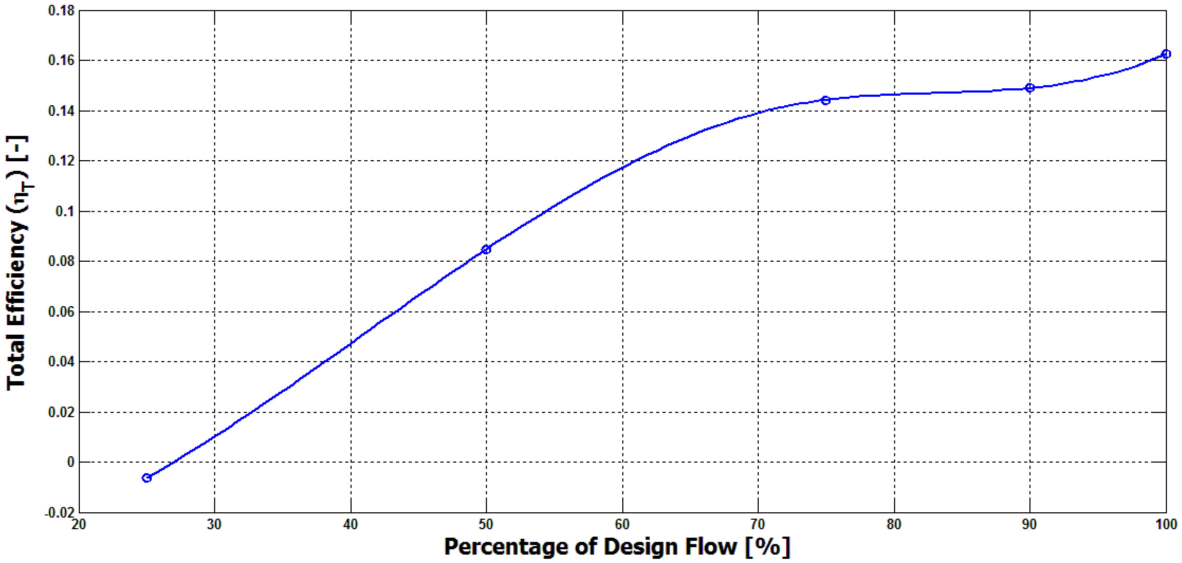

Figure 6-29: Variation of Total Efficiency [-] of the Turbine with Portion of Design Flow [%]

In contrast to this, taking the individual efficiencies alone gives other insight into this case. As was previously indicated, the Tesla turbine is more suited to the lower spectrum of flow and power. Though the gross efficiency of flow has not yet reached its maximum efficiency point, the outer and inner disks attain their maximum point around half the design case flow.

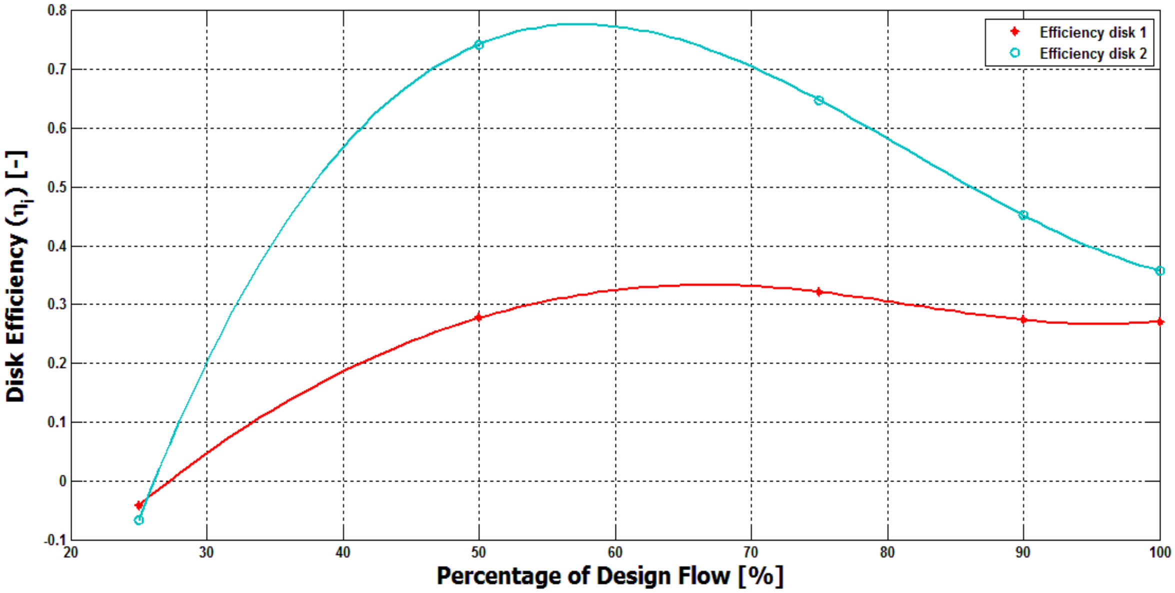

Figure 6-30: Individual Disk Efficiency [-] Variation with Percentage of Design Flow Rate [%]

This is due to the fact that the losses due to uncontrolled diffusion that occur immediately after disk space ejection and subsequent secondary losses resulting from flow being diverted from radial to axial type of motion are take away greater portion of the useful work in the lower flow operation than at the design operating condition.

Similar to the 2D fluid model, the flow domain experienced undesirable negative torque as the flow is going to transitional regime where the inbuilt FLUENT flow models fail to predict accurately.

6.2.2.4 Effect of Number of Nozzles

Three different nozzle configurations, all with the same fluid flow rate and injection area, were geometrically constructed. The inlet velocity angle and magnitude was maintained. The nozzles are located at equal tangential distance from each other. All comparisons are made at design operating conditions.

Torque comparison between the three combinations of nozzles with respective rotor disk was made on the following bar graph. The result demonstrates higher torque production is attained with four-nozzle combination while for the inner disks better torque was gained with the six-nozzle configuration.

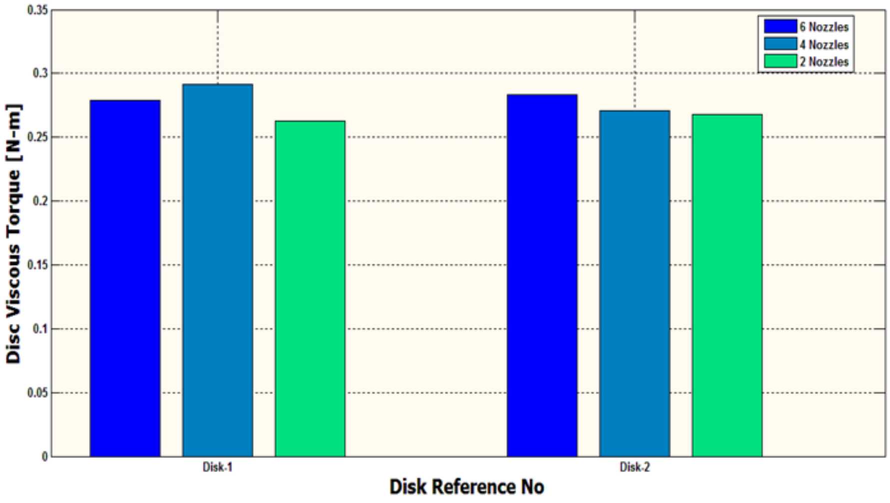

Figure 6-31: Torque Production Comparison Between Three Nozzle Configurations on Respective Disk Rotors

Since the twelve inner disks contribute greater share towards the final power output, greater total turbine power production is achieved with the six-nozzle combination.

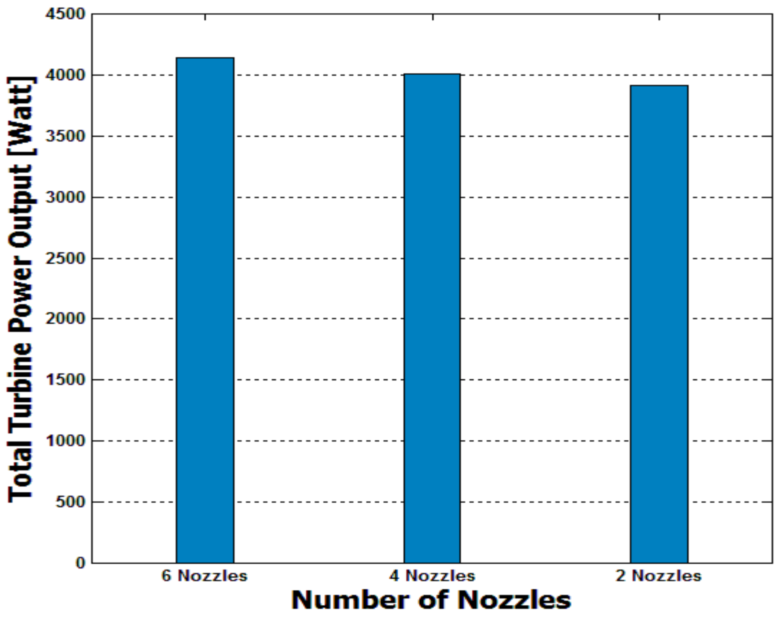

Figure 6-32: Total Turbine Output for Three Nozzle Configurations at Design Operating Conditions

Although, the six-nozzled turbine delivers the most power yield, it is not the most efficient of the three. Graphical comparison of total turbine efficiencies for the three combinations is presented in the figure below.

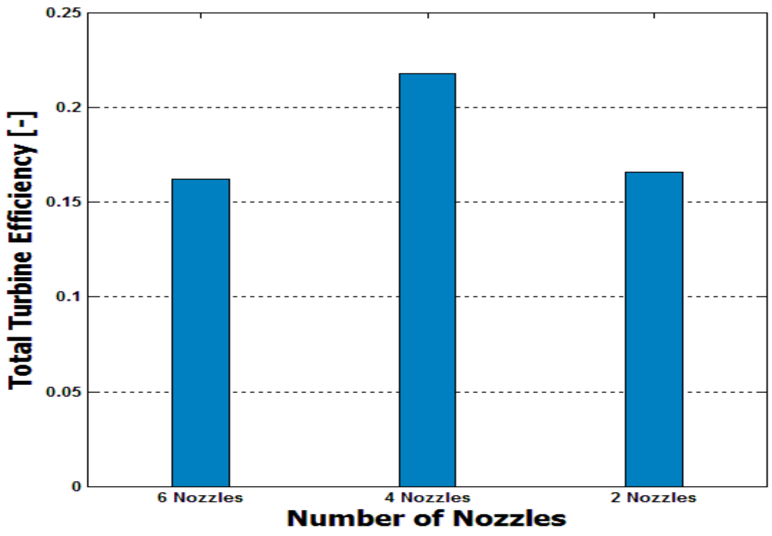

Figure 6-33: Total Turbine Efficiency for Three Nozzle configurations at Design Operating Conditions

Since the loading coefficient to non-dimensional pressure drop ratio in both flow spaces is the highest with the four nozzle combination, this combination wins the highest efficiency than the other two possibilities.

Table 6-2: Summary of Calculated Quantities for Three Nozzle Combinations

	Inter-diskSpace Reference	6 nozzle	4 nozzles	2 nozzles
Tangential Velocity Ratio (TVR) [-]	Space-1	2.13676565	1.957987	2.01008713
	Space-2	2.29497922	2.104566	2.20432753
Space Loading Coefficient (λ) [-]	Space-1	1.405165	1.539893	1.247344
	Space-2	1.466362	1.739804	1.347077
Non-Dimensional Pressure Drop ($\Delta\overline{P}$) [-]	Space-1	3.675162	2.810964	3.299519
	Space-2	3.868356	2.908152	3.525296
$\frac{\lambda}{\Delta\overline{P}}$	Space-1	0.382340966	0.547816721	0.378038064
	Space-2	0.379065862	0.598250768	0.38211745

The loading coefficient to non-dimensional pressure drop ratio can be directly used to compare all the configurations since the flow is the same in all cases. Greater λ to $\Delta\overline{P}$ ratio would mean here is more work done on the rotor disks by the spiraling fluid with minimum pressure drop on the fluid stream at the same inlet tangential velocity.

6.3 Conclusion

A steady state incompressible CFD models for multiple disk Telsa turbine have been presented for two and three dimensional fluid space frame. The CFD models illustrated mainly turbulent fluid flow regime, a topic which is rarely covered in most prior literatures. Apart from this, the inherent knowledge gap on its internal flow has created a wide variety of design algorithms, which as opposed to conventional turbines, that are not unified to produce one standard design protocol. With regard to this, by applying some modifications on certain design aspects of the previously published Couto et.al. design procedure, a two dimensional design was prepared with disk gap estimation totally based upon turbulent flow conditions. Although both2D and 3D models have their strength and weaknesses, they served as CFD verification of merit of this design procedure.

In concise terms, the knowledge gained from the forgoing discussions is summarized in the following points.

- There is a considerable agreement as to how the pattern of global terms such as total power yield, total turbine efficiency, individual disk efficiency and inter-disk space loading coefficients vary between the two models.
- Both models illustrated the existence of optimum operating rotor angular speed for optimum efficiency and maximum power. Although flow reduction would normally bring about rise in individual disk efficiency as it was thought initially, the same design flow percentage does not guarantee a maximum or incremental gain in total turbine efficiency. On the same token, the individual disk efficiency rise is possible up until the flow relaminarizes and goes into transitional flow.
- The radial variation (spread) of tangential velocity from disk row entry to the point of disk departure gives a good indication where in which portion of the disk energy transferred the most.
- Peculiar axial and radial velocity profiles were recorded in between the disks that relate much to the boundary layer profile formed from the two edges and the losses that are created at trailing edges of each disk.
- Efficiency increment is directly related to the loading coefficient rise faster than the non-dimensional pressure drop in the adjacent flow spaces near a given disk. Optimum

operating rotor angular speed must be chosen at a point where the loading coefficient starts to drop faster than the pressure drop.

The maximum total efficiencies determined so far are in the same neighborhood, but not higher, as most of early reported studies performed on laminar flows. As per our simulation has predicted, the efficiency of the individual disks' alone has not gone far above 27 % which negates, if not for laminar flows, the idealization that 95 % efficiency could be attained for the same case.

6.4 Recommendation

The present paper discussed two alternative CFD models for studying turbulent flows between co-rotating disks encapsulated in a stationary casing. As mentioned earlier, these models have their strengths and weaknesses per se. The reported viscous torques between successive disks show a variation of not less than 0.8 % while this value goes up as much as 2.79 % for the 3D models. Of course, this amount of disparity is not only a result of three dimensional velocity components that are contributing towards the reversibility of the flow but also from modeling limitations that seem to introduce less realm to the boundary specification. Thus, the current models should be perfected by a 3D model, with at least half the number of disks and the axial span for fluid injection, that are in turn solved by high capacity computers. Such model would fine tune the preexisting solutions to further understand the superimposition of fluid mass across the consecutive flow spaces towards the central exit.

The presented models so far are based on incompressible fluid with no considerations given towards mechanical and frictional losses that vary according to the operational angular speed, flow and load of the turbine. This would certainly create delay between point of attaining maximum output and point of reaching maximum efficiency. As was seen before, the disk row exit losses have a great contribution to turbine efficiency loss and fluid pressure drop within the central passage. The viability of stator flow deflector should also be analyzed in ushering out the exiting fluid thereby minimizing such losses. Thus, the final model should incorporate such density and loss factors into consideration for better depicting the fluid flow scenario from which a clean cut design procedure may emerge.

REFERENCES

1. O'Neill, John, Prodigal Genius: The Life of Nikola Tesla, Ives, Washburn, Inc. 1944, pp 218-228.
2. "History of Tesla turbine", November 29, 2010.
3. Nikola Tesla: Serial no. US 523,832, US patent office, 1913.
4. Jeffery Stuart Allen, "A Model for Fluid flow between parallel, Co-rotating Annular Disks", University of Dayton, 1990.
5. http://www.brighthub.com/members/kingauthor.aspx
6. Andrés Felipe Rey Ladino : "Numerical Simulation of the Flow Field in a Friction-Type Turbine (Tesla Turbine)" , Vienna University of Technology , Austria,2004.
7. Michael John Lawn, "An Investigation of Multiple-Disk Turbine Performance Parameters", Jan. 1972.
8. Warren Rice, "Tesla Turbo machinery", Handbook of Turbo machinery-Chapter 14, Published by Marcel Dekker, Arizona, USA,1991.
9. Warren Rice, "Tesla Turbo machinery", IV International Nikola Tesla Symposium, Sept. 1991.
10. Yazan Taamneh, "Numerical Simulation of Fluid Flow in Enclosed Rotating Filter and Disk", ARPN Journal of Engineering and Applied Sciences, 2010.
11. Miller, G.E. and Sidhu, A. 1992 Multiple disk centrifugal pump as an artificial ventricle. Proceedings of the 9th Conference on Engineering Mechanics, May 24-27; College Station, TX, USA; Code 16608 pp. 976-979.
12. Valente, A. 2008 Installation for pressure reduction of hydrocarbon gases in a near isothermal manner. Abu Dhabi International Petroleum Exhibition and Conference, November 3-6; Abu Dhabi, UAE, DOI: 10.2118/118034-MS.
13. Fuller, H. J., United States Patent "Wind Turbine for Generation of Electric Power," No. 7695242, Apr. 13, 2010.
14. PetrBloudíček and David Paloušek, "Design of Tesla Turbine", Konference diplomovýchprací. Czech republic, 2007.
15. website: PowerPedia Tesla_turbine.htm

16. L. Jedrzejewski, P. Lampart, “Tesla Friction-Type Micro Turbine for Small-Scale Cogeneration”, Polish Academy of Sciences, 2011.
17. Warren Rice, “An analytical and Experimental Investigation of Multiple Disk Pumps and Compressors”, pp. 191-200, Journal of Engineering for Power, ASME, 1963.
18. Warren Rice, “Analytical and Experimental Investigation of Multiple-Disk Turbines”, ASME, USA,1965.
19. L. Matsch, W. Rice, “An Asymptotic Solution for Laminar Flow of an Incompressible Fluid Between Rotating disks”, ASME, Journal of Applied Mechanics, March 1968.
20. Lee Matsch, Warren Rice, “Potential Flow between Two Parallel Circular Disks with Partial Admission”, pp.239-240, Journal of Applied Mechanics, ASME, 1967.
21. Lee Matsch, Warren Rice, “Flow at Low Reynolds number with Partial admission between Rotating Disks”, pp.768-770, Journal of Applied Mechanics, ASME, 1967.
22. K.E.Boyd, W. Rice, “Laminar Inward flow of Incompressible Fluid between Rotating Disks, with full peripheral admission.” Journal of Applied Mechanics, ASME, pp. 229-237, 1968.
23. R. Adams, W. Rice, “Experimental Investigation of flow between Corotating Disk”, pp.844-849, Journal of Applied Mechanics, ASME,1970
24. B.E. Boyack, “Integral Method for Flow between corotating disks”, pp.350-354, Journal of General Engineering,1971.
25. L.L. Pater, E. Crowther, W. Rice,“Flow Regime Definition for Flow between Corotating disks”, pp.29-34, Journal of Fluid Engineering,1974.
26. M.J.Lawn,JR., W. Rice, “Calculated Design data for Multiple-disk Turbine using Incompressible Fluid”, pp.252-258, Journal of Fluids Engineering,ASME,1974.
27. S.H. Hasinger& L.G. Kehrt, “Investigation of a shear-force pump”, pp.201-207, Journal of Engineering for Power,ASME, 1963.
28. Abhijit Guha, Sayantan Sengupta, “The fluid dynamics of the rotating flow in a Tesla disc turbine”,pp.112-123, Europian Journal of Mechanics B/Fluids, 2012.
29. N. Huybrechts, O. Berten, E. Lenclud, “Numerical study of a Tesla turbine”, Free University of Brussels,
30. Piotr Lampart, Krzysztof Kosowski, Marian Piwowarski, Łukasz Jędrzejewski, “Design Analysis of Tesla micro-turbine operating on low boiling point medium”, pp. 28-33,Polish Maritime Research, 2009.

31. Piotr Lampart, Lukasz Jedrezejewski, “Investigation of Aerodynamics of Tesla Bladeless Microturbines”, Journal of Theoretical and Applied Mechanics,Vol.49 No. 2, pp477-499, Warsaw 2011.
32. Matej Podergajs, “The Tesla Turbine”-Seminar Paper, University of Ljubljana, March 2011.
33. Bryan P. Ho-Yan, “Tesla Turbine for Pico Hydro Applications”, Guelph Engineering Journal (4), 1-8, 2011, Ontario- Canada.
34. S.L. Soo, “Laminar Flow over an enclosed Rotating Disk”, pp. 287-296, Journal of Fluid Mechanics, ASME, 1957.
35. Breiter, M.C., and Pohlhausen, K., “Laminar inward flow between Two parallel rotating disks”, pp. 62-218, Aeronautical Research Laboratories, Wright-Patterson Air force base, 1962.
36. E. William Beans, “Investigation into Flow Characteristics of Friction Turbines”, Journal of Spacecraft, Vol.3 No 1, January 1966 pp 131-134.
37. Peter Harwood, “Further Investigations into Tesla Turbomachinery”-Mechanical Engineering project, Nov. 2008.
38. J. H. Morris, ‘‘Performance of Multiple-Disk-Rotor Pumps with Varied Inter-disk Spacing,’’ David W. Taylor Naval Ship R and D Center, Bethesda, MD, U.S. Navy Report Number DTNSRDC-80/008, August (1980).
39. M. E. Crawford and W. Rice, ‘‘Calculated Design Data for the Multiple-Disk Pump Using Incompressible Fluid,’’ ASME Trans. J. Eng. Power, 96: 274–282(1974).
40. A Guha and B Smiley, “Experiment and analysis for an improved design of the inlet and nozzle in Tesla disc turbines”, pp.261-267 ,Journal of Power and Energy, Indian Institute Of Tech,2009
41. P.-S. Wu, "Evaluation of Analytical Models for Multiple-Disk Pump Rotor Calculation," M.S. Thesis, Department of Mechanical and Aerospace Engineering, Arizona State University, May (1986)
42. D. Nendl, ‘‘DreidimensionalelaminareInstabilita¨ ten beiebenenWa¨ nden,’’ Z. Ange w. Math. Mech., 56: T211–213 (1976).
43. Couto, J.B.F., Duarte, J.B.F. and Bastos-Netto, D., th^{e} Tesla Turbine Revisited, University of Fortaleza, Ceara, Brazil, INPE, 2006

44. Lemma, E., Deam, R.T., Toncich, D. and Collins R. 2008 Characterization of a small viscous flow turbine. J. Experimental Thermal and Fluid Science, 33, 96-105.
45. Schlichting, H., Boundary Layer Theory, McGraw-Hill Book Co., Inc., New York, NY, fourth Ed., 1962, pp. 547.
46. FLUENT 6.3 User's Guide, "Modeling Basic Flow"- Chapter 9, "Modeling Turbulence"-Chapter 12& "Using the Solver"-Chapter 25, September 29 2006, Fluent Inc.
47. Cairns, W.M.J., The Tesla Turbine, Published by Camdem Miniature SteamServices, GB, 2nd edition, 2003
48. Logan, E.Jr., Handbook of Turbo machinery, Arizona State U. Marcel DekkerInc., Phoenix, 1991
49. White, F.M., Fluid Mechanics, McGraw-Hill Kogacucha, Ltd.Kosaido Publishing Co., Tokyo, Japan, 1979
50. S.S. Chawlaa, P.K.Srivastavab, A.S.Guptac: "Rotationally symmetric flow over a rotating disk", International Journal of Non-Linear Mechanics 44 (2009) 717 – 726, Elsevier, 2008.
51. TahsinEngin , Mustafa Özdemir, S_evkiÇes_meci : "Design, testing and two-dimensional flow modeling of a multiple-disk fan", Experimental Thermal and Fluid Science 33 (pp. 1180–1187) , 2009.
52. Snezˇana Šarboh : "The patents of Nikola Tesla", World Patent Information 32 (pp. 335–339), 2010.
53. E. Lennemann,. "Aerodynamic aspects of disk files", IBM Journal of Research and Development, pp. 480-488,November 1974.
54. Mustafa Turkyilmazoglu, "Exact Solutions for the Incompressible Viscous Fluid of a Rotating Disk flow", Progress in Applied Mathematics, Vol. 1 No. 1, 2011,pp. 90-97.
55. M.K. Khalil, Abu Abdou, "Friction Pump Performance Formulation", JKAU: Engineering Science, Vol. 10 No.1, pp 13-26(1998).
56. J.M. Lopez, "Flow between a stationary and a rotating disk shrouded by a co-rotating cylinder", Pennsylvania State University, 1996.
57. D. P. Kavenuke1, E. Massawe, O. D. Makinde, "Modeling laminar flow between a fixed impermeable disk and a porous rotating disk", African Journal of Mathematics and Computer Science Reasearch, Vol.2(7), 2009.

58. Van P. Cary, “Assessment of Tesla turbine performance for small scale Rankine Combined Heat and Power Systems”, ASME, Journal of Engineering for Gas Turbine and Power, Vol. 132, 2010.
59. Sebastien Poncet, Roland Schiestel, Romain Monchaux, “Turbulence modeling of the Von Karman flow: Viscous and Inertial Strings”, June 2007.
60. website: www en.wikipedia.org/wiki/Tesla_turbine.htm
61. http://www.frank.germano.com/nikolaTesla.htm
62. C.B.Basset, Jr. “An Integral solution for a compressible flow through disk turbines”, 10th Intersociety Conference of Energy Conversion, pp. 1098-1106, 1975.
63. Vedavalli G. Krishnan1, Zohora Iqbal1 and Michel M. Maharbiz1, “A Micro Tesla turbine for power generation from low pressure heads and evaporation driven flows”, Univerisity of California, Berkeley, 2011.
64. Romuald Puzyrewski and Krzysztof Tesch, “1D model calibration based on 3D calculations for Tesla Turbine”, Task Quarterly 14 No.3, pp. 237-248,as sourced from *http://www.bop.com.pl*, 2010.
65. Engineers without Borders- Program – Session 1, “Tesla Pump Irrigation System” project report, 2008.
66. H.P. Borate& N.D. Misal, “An effect of surface finish and spacing between discs on the performance of disc turbine”, pp. 25- 30, International Journal of Applied Research in Mechanical Engineering, ISSN:2231-5940, Vol. 2,2012.
67. “Gambit 2.4 Tutorial Guide”, FLUENT Inc. , Centerra Resource Park, NH, May 2007.

Appendix A: Realizable k − ε Turbulence Model

The Realizable $k-\varepsilon$model is a semi-empirical model based on model transport equation for the turbulence kinetic energy (k) and its dissipation rate (ε). The model transport equation for k is derived from the exact equation while the model transport equation for ε was derived from an exact equation for the transport of mean-square vorticity fluctuation. Both equations use a variable turbulent viscosity formation as opposed to standard $k-\varepsilon$ model.

The turbulence kinetic energy, k, and its rate of dissipation, are obtained from the following transport equations:

$$\frac{\partial}{\partial t}(\rho k)+\frac{\partial}{\partial x_j}\left(\rho k u_j\right)=\frac{\partial}{\partial x_j}\left[\left(\mu+\frac{\mu_t}{\sigma_k}\right)\frac{\partial k}{\partial x_j}\right]+G_k+G_b-\rho\varepsilon-Y_M+S_k \qquad \textbf{(}\boldsymbol{k}\textbf{ -equation)}$$

$$\frac{\partial}{\partial t}(\rho\varepsilon)+\frac{\partial}{\partial x_j}\left(\rho\varepsilon u_j\right)=\frac{\partial}{\partial x_j}\left[\left(\mu+\frac{\mu_t}{\sigma_\varepsilon}\right)\frac{\partial\varepsilon}{\partial x_j}\right]+\rho C_1 S_\varepsilon-\rho C_2\frac{\varepsilon^2}{k+\sqrt{\upsilon\varepsilon}}+C_{1\varepsilon}\frac{\varepsilon}{k}C_{3\varepsilon}G_b+S_\varepsilon \ \textbf{(}\boldsymbol{\varepsilon}\textbf{–equation)}$$

Where, C_2 and $C_{1\varepsilon}$ are constants. σ_k and σ_ε are turbulent Prandtl numbers for k and ε while S_k and S_ε are user-defined source terms.

$$C_1=max\left[0.43, \qquad \frac{\eta}{\eta+5}\right], \qquad \eta=S\frac{k}{\varepsilon}, \qquad S=\sqrt{2S_{ij}S_{ij}}$$

The values taken for simulation process correspond to default values supplied by FLUENT.

$C_2=1.9$ $C_{1\varepsilon}=1.44$ $\sigma_k=1$ $\sigma_\varepsilon=1.2$

$G_k$is the generation of turbulence kinetic energy

$$G_k=-\rho\overline{u_i u_j}\frac{\partial \mathrm{u}_j}{\partial x}=\mu_t S^2$$

The eddy viscosity in the above equations is given by,

$$\mu_t=\rho C_\mu\frac{k^2}{\varepsilon}$$

The variable viscosity C_μ varies with a factor U^*, which normalizes the rate-of-rotation tensor and source terms.

$$C_\mu=\frac{1}{A_0+A_s\frac{kU^*}{\varepsilon}}$$

and

$$U^*\equiv\sqrt{S_{ij}S_{ij}+\tilde{\Omega}_{ij}\tilde{\Omega}_{ij}}$$

A_0 and A_s are constants given as,

$$A_0=4.04 \ \ and\ A_s=\sqrt{6}cos\phi$$

where

$$\phi = \frac{1}{3}\cos^{-1}\left(\sqrt{6}W\right), W = \frac{S_{ij}S_{jk}S_{ki}}{S^3}, \tilde{S} = \sqrt{S_{ij}S_{ij}}, S_{ij} = \frac{1}{2}\left(\frac{\partial u_j}{\partial x_i} + \frac{\partial u_i}{\partial x_j}\right)$$

Y_M is the fluctuation dilation in compressible turbulence to the overall dissipation rate and is given as,

$$Y_M = 2\rho\varepsilon M_t^2$$

M_t is the turbulent Mach number and is determined from,

$$M_t = \sqrt{\frac{k}{\sqrt{\gamma RT}^2}}$$

G_b is the generation of turbulence kinetic energy due to buoyancy where non-zero gravity field and temperature (density) gradient is present in the flow domain.

$$G_b = \beta g_i \frac{\mu_t}{Pr_t}\frac{\partial T}{\partial x_i}$$

The coefficient of thermal expansion, β, is defined as,

$$\beta = -\frac{1}{\rho}\left(\frac{\partial \rho}{\partial T}\right)_p$$

Pr_t=0.85 for Realizable k-ε model

Appendix B –1: Tesla Turbine Design Drawings [Tesla Turbine Assembly]

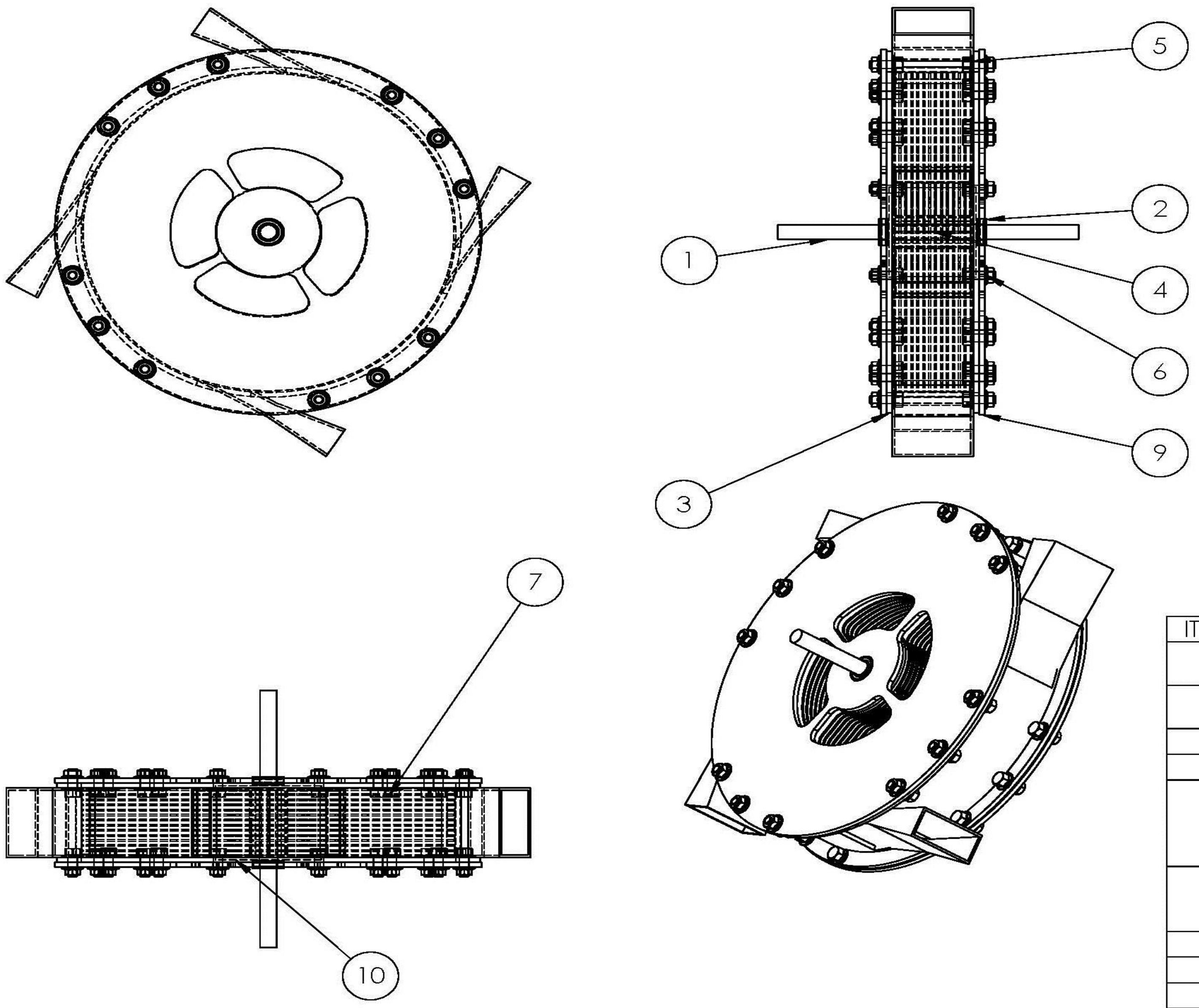

ITEM NO.	PART Name	DESCRIPTION	QTY.
1	Torque transmitting shaft		1
2	Radial bearing	AFBMA 20.1 - 28-9 - Full,SI,NC,Full_68	2
3	Peripheral Casing Cover		1
4	Nozzle		4
5	Hex Screw	B18.2.3.9M - Heavy hex flange screw, M5 x 0.8 x 12 --12N	24
6	Hex Nut	B18.2.2.4M - Hex flange nut, M5 x 0.8 --N	24
7	Rotor Disk		14
8	middle spacer		13
9	Side casing cover		2
10	end spacer		1

UNLESS OTHERWISE SPECIFIED:
DIMENSIONS ARE IN MILLIMETERS
SURFACE FINISH:
TOLERANCES:
LINEAR:
ANGULAR:

FINISH:

DEBUR AND BREAK SHARP EDGES

DO NOT SCALE DRAWING

REVISION

	NAME	SIGNATURE	DATE
DRAWN	Surafel Shimeles		21/4/14
CHK'D	Dr.-Ing. Abebayehu		
APPV'D			
MFG			
Q.A			

TITLE:

Tesla Turbine Assembly

MATERIAL:

DWG NO. 1

A3

WEIGHT:

SCALE: 1:3

SHEET 1 OF 1

Appendix B –2: Tesla Turbine Design Drawings [Side Casing Cover]

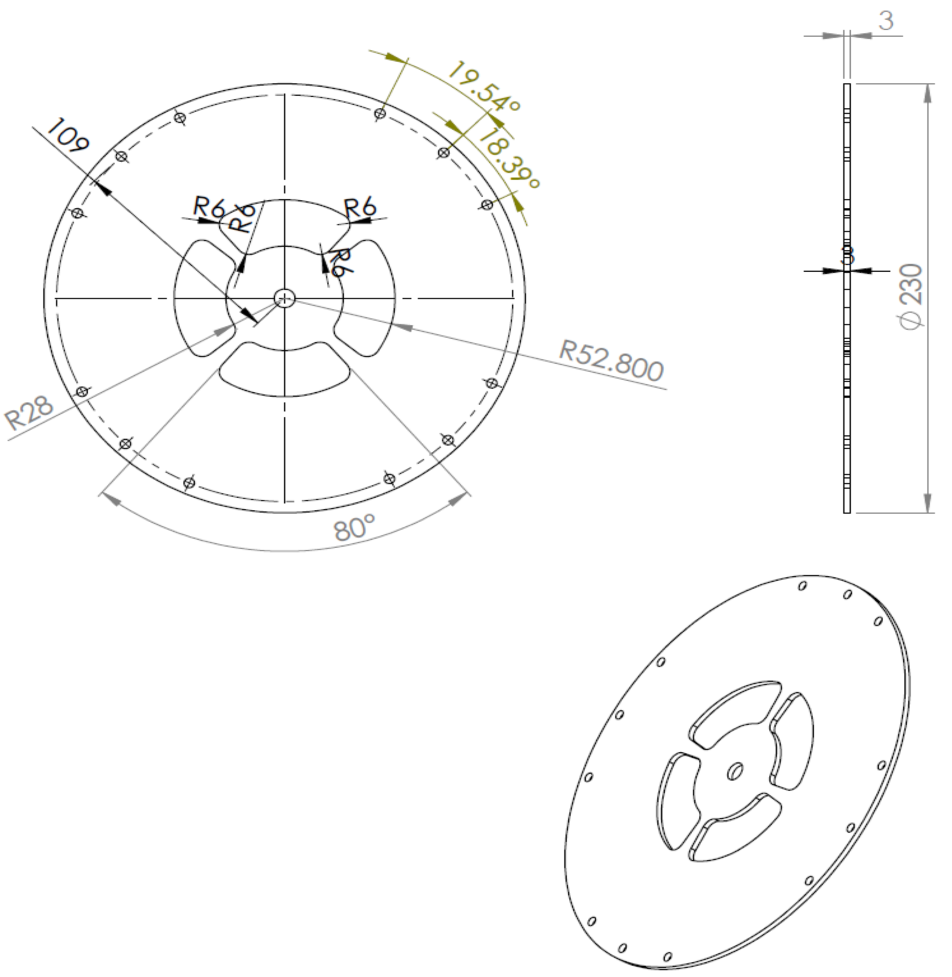

UNLESS OTHERWISE SPECIFIED: DIMENSIONS ARE IN MILLIMETERS SURFACE FINISH: TOLERANCES: LINEAR: ANGULAR:	FINISH:	DEBUR AND BREAK SHARP EDGES	DO NOT SCALE DRAWING
			REVISION

	NAME	SIGNATURE	DATE
DRAWN	Surafel Shimeles		21/4/14
CHK'D	Dr.-Ing Abebayehu		
APPV'D			
MFG			
Q.A			

TITLE:

Side Casing Cover

MATERIAL:

Mild Steel

DWG NO. 2

A4

WEIGHT:

SCALE 1:3

SHEET 1 OF 1

Appendix B –3: Tesla Turbine Design Drawings [Fluid Injection Nozzle]

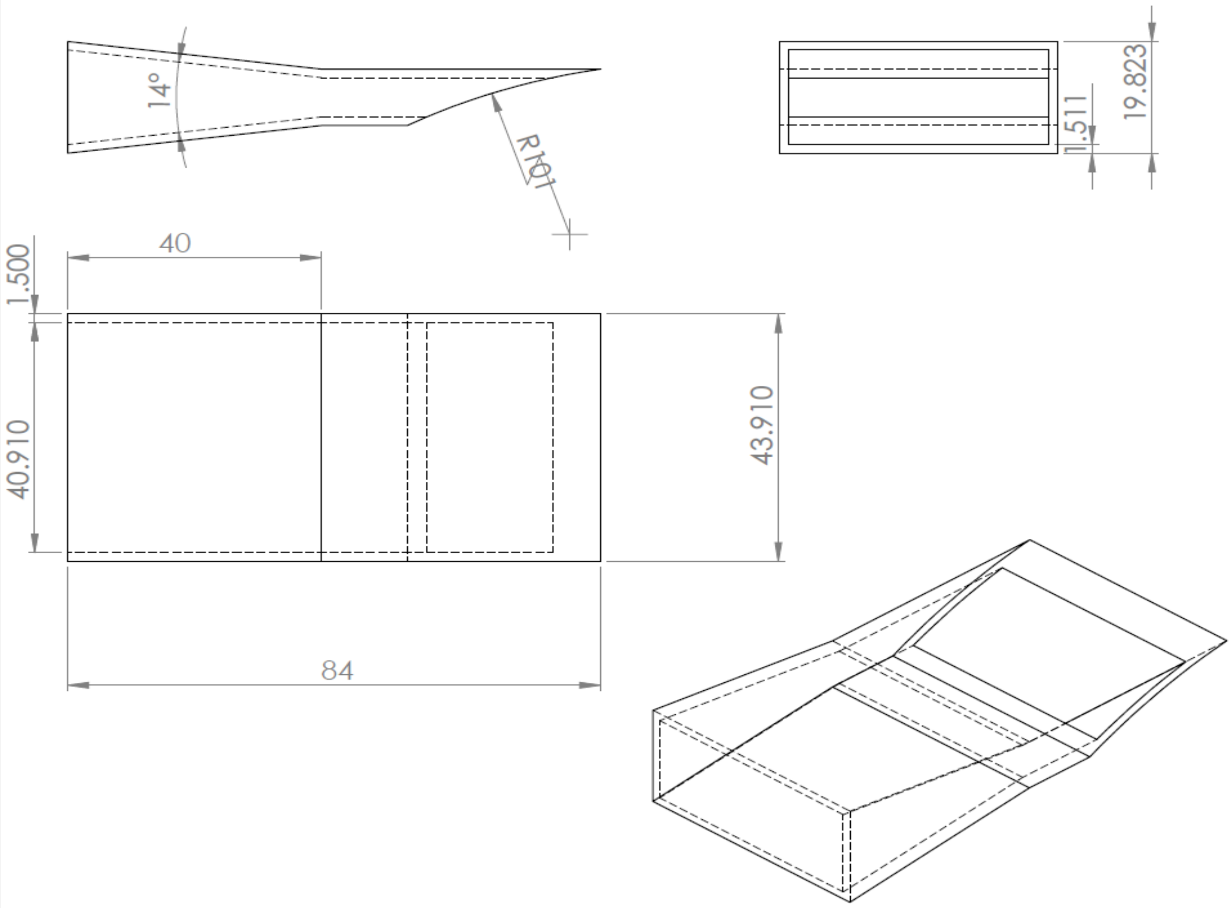

UNLESS OTHERWISE SPECIFIED:
DIMENSIONS ARE IN MILLIMETERS
SURFACE FINISH:
TOLERANCES:
LINEAR:
ANGULAR:

FINISH:

DEBUR AND BREAK SHARP EDGES

DO NOT SCALE DRAWING

REVISION

	NAME	SIGNATURE	DATE
DRAWN	Surafel Shimeles		21/4/14
CHK'D	Dr.-Ing Abebayehu		
APPV'D			
MFG			
Q.A			

TITLE:
Fluid Injection Nozzle

MATERIAL:
Mild Steel

DWG NO.
3

A4

WEIGHT:

SCALE:1:1

SHEET 1 OF 1

Appendix B –4: Tesla Turbine Design Drawings [Peripheral Casing Cover]

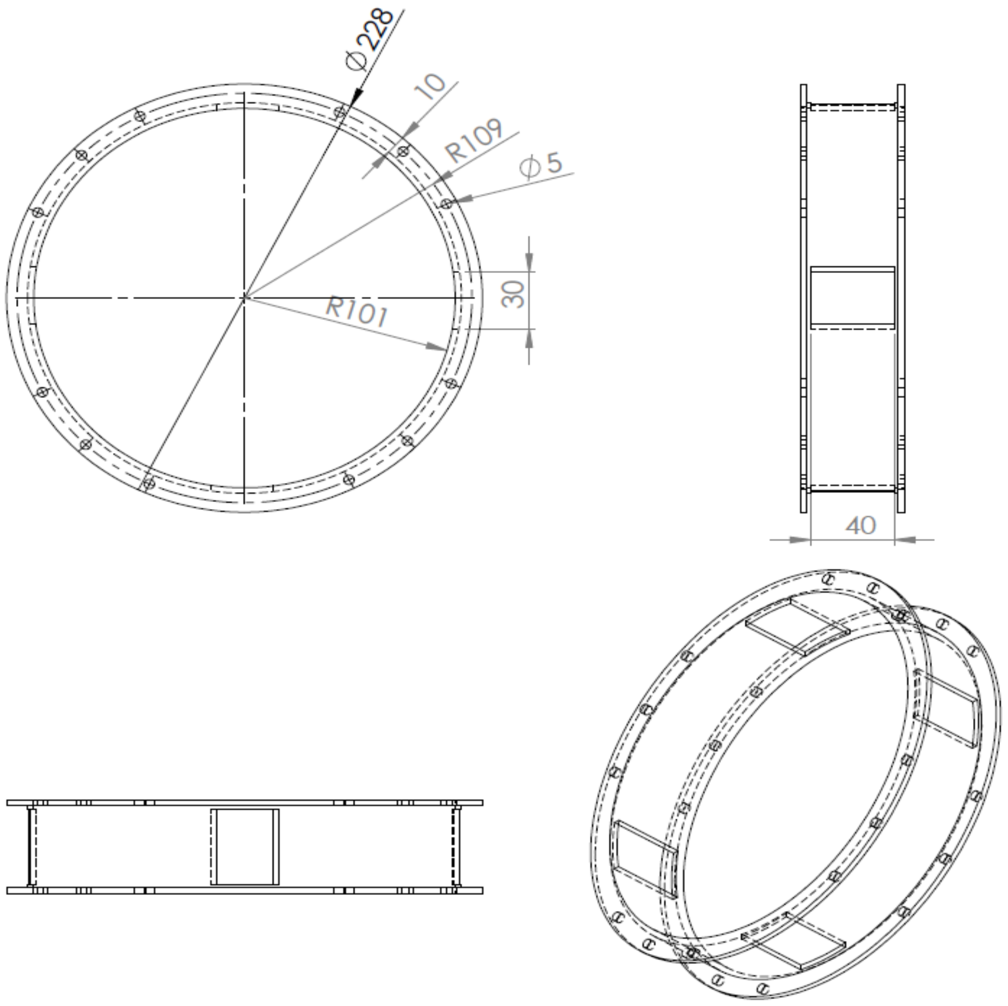

UNLESS OTHERWISE SPECIFIED: DIMENSIONS ARE IN MILLIMETERS SURFACE FINISH: TOLERANCES: LINEAR: ANGULAR:	FINISH:	DEBUR AND BREAK SHARP EDGES	DO NOT SCALE DRAWING	REVISION

	NAME	SIGNATURE	DATE
DRAWN	Surafel Shimeles		21/4/12
CHK'D	Dr.-Ing Abebayehu		
APPV'D			
MFG			
Q.A			

TITLE: Peripheral Casing Cover

MATERIAL: Sheet Metal

DWG NO. 4

A4

WEIGHT:

SCALE:1:5

SHEET 1 OF 1

Appendix B –5: Tesla Turbine Design Drawings [Rotor Disk]

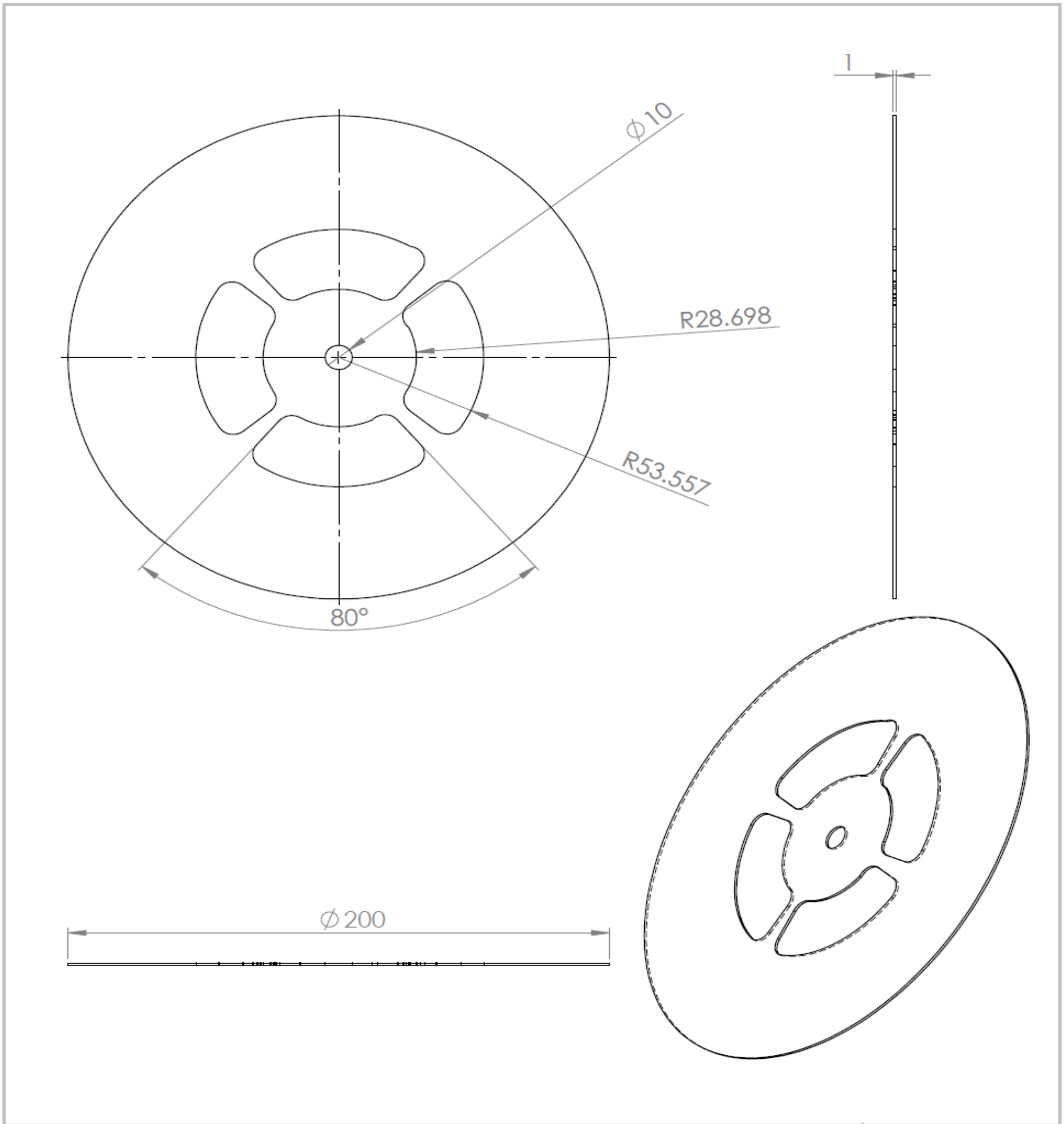

UNLESS OTHERWISE SPECIFIED: DIMENSIONS ARE IN MILLIMETERS SURFACE FINISH: TOLERANCES: LINEAR: ANGULAR:	FINISH:		DEBUR AND BREAK SHARP EDGES	DO NOT SCALE DRAWING	REVISION
	NAME	SIGNATURE	DATE		TITLE:
DRAWN	Surafel Shimeles		21/4/14		Rotor Disk
CHK'D	Dr.-Ing Abebayehu				
APPV'D					
MFG					
Q.A				MATERIAL: Mild Steel	DWG NO. 5 A4
				WEIGHT:	SCALE:1:2 SHEET 1 OF 1

Appendix B –6: Tesla Turbine Design Drawings [Torque Transferring Shaft]

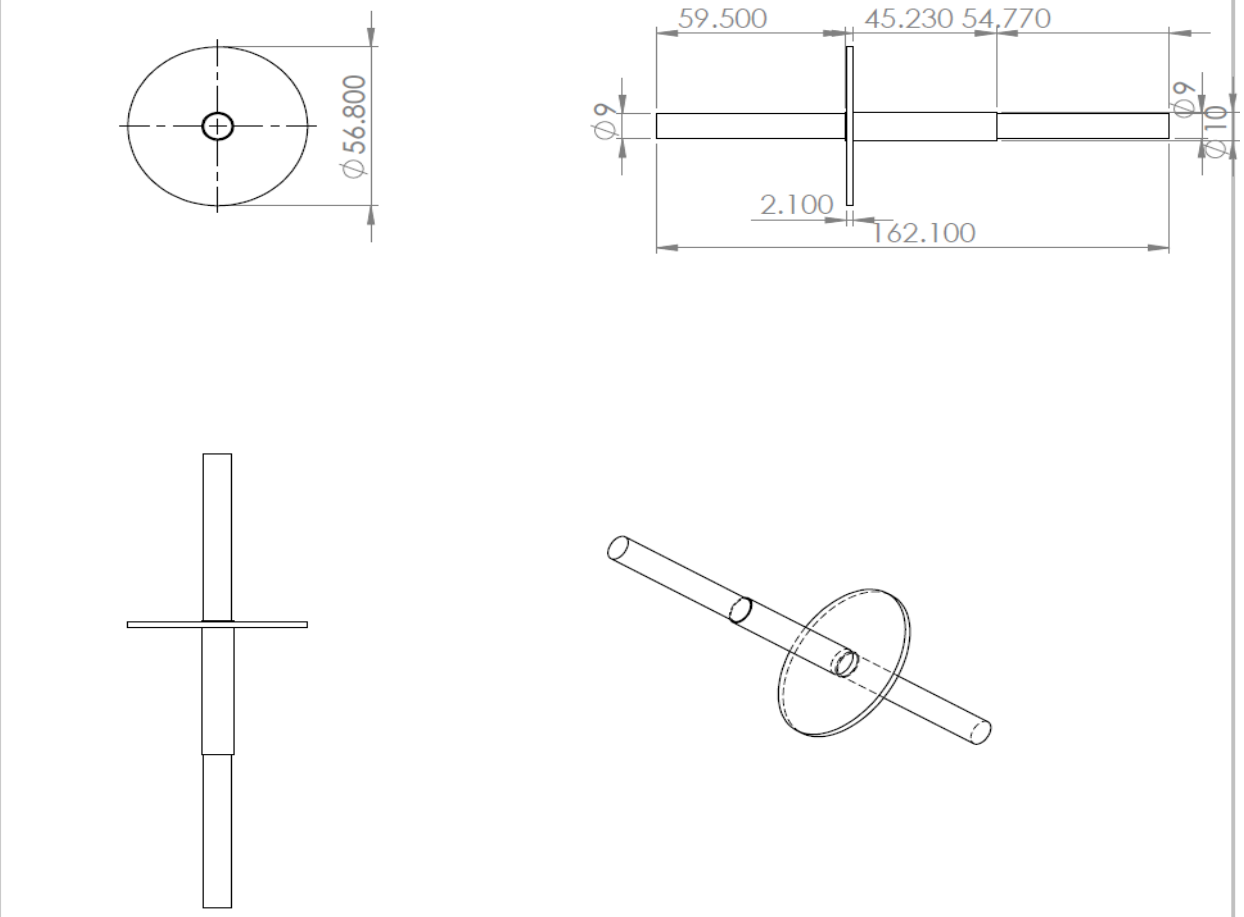

UNLESS OTHERWISE SPECIFIED:
DIMENSIONS ARE IN MILLIMETERS
SURFACE FINISH:
TOLERANCES:
LINEAR:
ANGULAR:

FINISH:

DEBUR AND BREAK SHARP EDGES

DO NOT SCALE DRAWING

REVISION

	NAME	SIGNATURE	DATE
DRAWN	Surafel Shimeles		21/4/21
CHK'D	Dr.-Ing Abebayehu		
APPV'D			
MFG			
Q.A			

TITLE:
Torque Transferring Shaft

MATERIAL:
Steel

DWG NO.
6

A4

WEIGHT:

SCALE:1:2

SHEET 1 OF 1

Appendix B –7: Tesla Turbine Design Drawings [End Spacer]

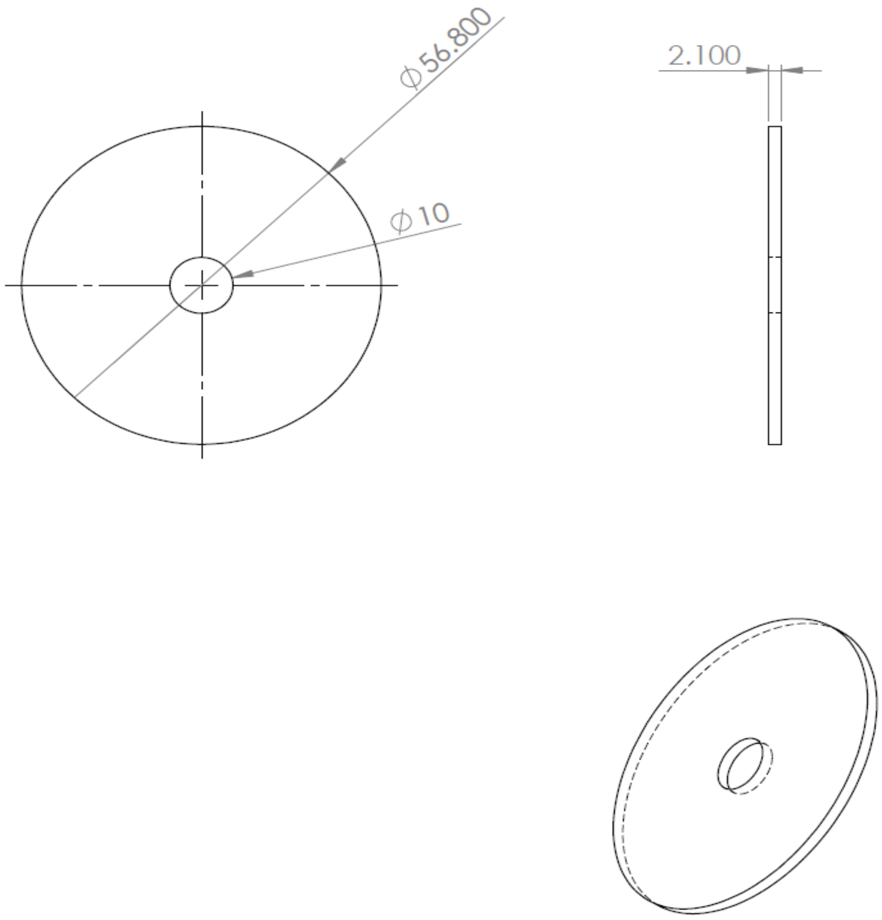

UNLESS OTHERWISE SPECIFIED:
DIMENSIONS ARE IN MILLIMETERS
SURFACE FINISH:
TOLERANCES:
LINEAR:
ANGULAR:

FINISH:

DEBUR AND
BREAK SHARP
EDGES

DO NOT SCALE DRAWING

REVISION

	NAME	SIGNATURE	DATE
DRAWN	Surafel Shimeles		12/4/14
CHK'D	Dr.-Ing Abebayehu		
APPV'D			
MFG			
Q.A			

TITLE:

End Spacer

MATERIAL:
Steel

DWG NO.
7

A4

WEIGHT:

SCALE:1:1

SHEET 1 OF 1

DECLARATION

I hereby declare that, except for references to other peoples' work which have been duly Acknowledged, this report is the result of my own research work and has not previously been submitted for a degree at this or any other university.

Name: Surafel Shimeles
Signature: ___________________

This thesis has been submitted for examination with my approval as an advisor

Dr.-Ing. Abebayehu Assefa
Signature: _____________________